RUHR-UNIVERSITÄT BOCHUM

Thermodynamic Dislocation Theory with Applications in Crystal Plasticity

Tuan Minh Tran

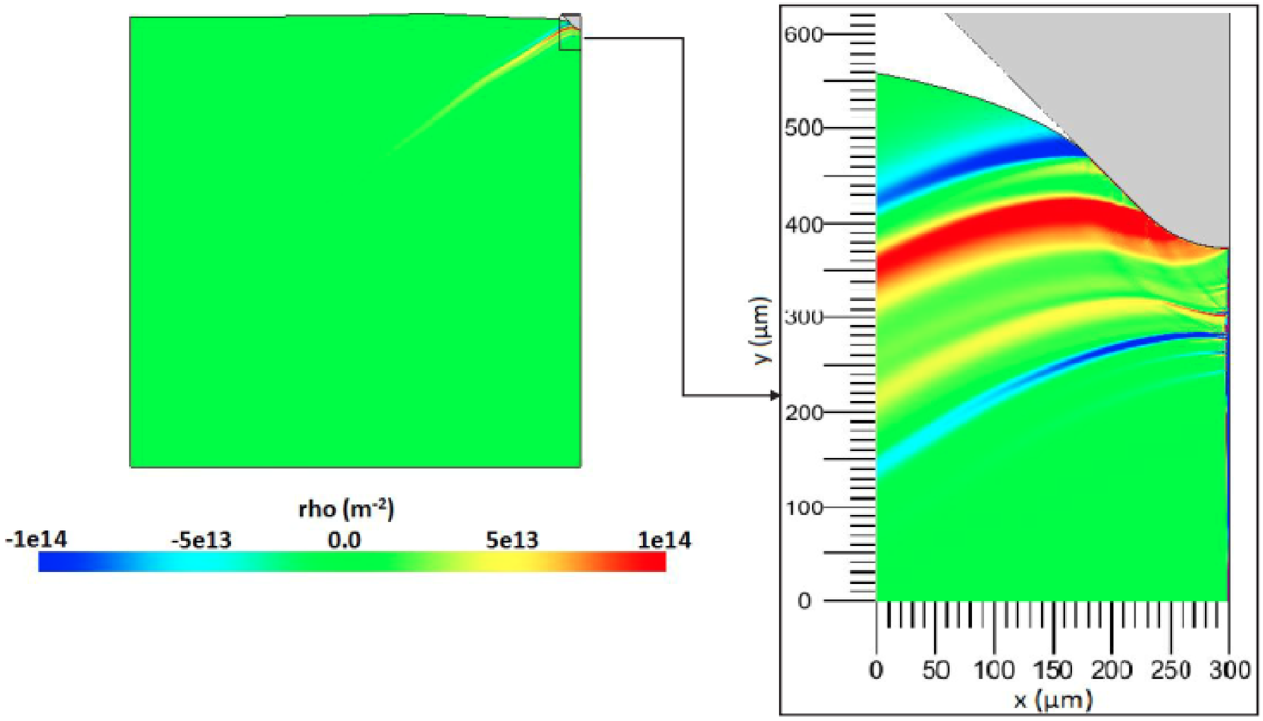

Dissertation

Thermodynamic Dislocation Theory with applications in crystal plasticity

Zur Erlangung des akademischen Grades

Dr.-Ing.

vorgelegt der

Fakultät für Bauingenieurwesen

an der Ruhr-Universität Bochum

von

Tuan Minh Tran,
geb. 11.11.1986 in CanTho, Vietnam

für Anh Thu und Minh Khue

Mündliche Prüfung: 23.04.2019

1. Gutachter: Prof. Dr. rer. nat. Le Khanh Chau
2. Gutachter: Prof. Dr. rer. nat. Klaus Hackl
3. Gutachter: Prof. Dr. -Ing. Dennis Kochmann
4. Gutachter: Prof. Dr. rer. nat. Harro Stolpe

Abstract

This dissertation investigates within the thermodynamic dislocation theory the plane strain problems of crystalline solids which are subject to elasto-plastic deformations. The present work consists of two main parts, which emphasize different modeling aspects in this context.

In the first part, the thermodynamic dislocation theory is extended to include the thermal effects that were missing in earlier versions. We also propose an extension of thermodynamic dislocation theory to non-uniform plastic deformation in the macro length scale, where the influence of excess dislocations can be ignored. A comparison of the stress-strain curves with the experiments for compression, shear, and torsion tests is also discussed in detail.

The second part examines the use of thermodynamic dislocation theory (TDT) for nonuniform plastic deformation, which is more advanced than its predecessor, the continuum dislocation theory. The free energy is modified to take into account not only the energy of excess but also redundant dislocations. The finite element solutions of the indentation test and the comparison with the experiment as well as the application of TDT to the anti-plane-shear are demonstrated in this work.

Acknowledgements

Looking back on my time at the Chair of Mechanics and Material Theory of the Ruhr-University Bochum, I would never have been able to complete this dissertation without the help of many people. Therefore I would like to thank all those who supported me, of whom I would like to mention the most important ones here.

First and foremost I am very grateful to my supervisor Prof. Dr. rer. nat. Khanh Chau Le for his patience, motivation, enthusiasm and immense knowledge. His guidance has helped me throughout the time of research and writing this dissertation on thermodynamic dislocation theory. I greatly appreciate Prof. Dr. rer. nat. Klaus Hackl for creating a pleasant atmosphere and an open environment for research and discussion. I would also like to thank Prof. Dr. -Ing. Matthias Baitsch, who gave me various constructive advices on numerical analysis.

Many thanks to my former and current colleagues, Dr. Ulrich Hoppe, Barbara Fromme, Yinguang Piao, Asim Khan, Binh Duong Nguyen, Lu Trong Khiem Nguyen, Christina Günther and the rest of the chair for creative atmosphere and friendship.

Last but not least I am grateful to my family for their love and care.

Contents

1 Introduction **1**

2 Physical backgrounds **5**
- 2.1 Crystalline structure and plastic deformation 5
  - 2.1.1 Crystalline structure of metals 5
  - 2.1.2 Lattice defects 6
  - 2.1.3 Plastic deformation of single crystals 7
- 2.2 Fundamental of dislocations 11
- 2.3 Properties of dislocations 15
  - 2.3.1 Stress field and self energy of dislocations 15
  - 2.3.2 Forces on a dislocation 16
  - 2.3.3 Interaction of dislocations 18
- 2.4 Thermodynamic Dislocation Theory (TDT) for uniform plastic deformations 20
  - 2.4.1 Effective temperature 21
  - 2.4.2 Depinning model 22
  - 2.4.3 Non-equilibrium equations of motion 23
  - 2.4.4 Scaling and dimensionless variables 25
- 2.5 Thermodynamic Dislocation Theory (TDT) for non-uniform plastic deformations 27
  - 2.5.1 Kinematics 28
  - 2.5.2 Energy of dislocation network 30
  - 2.5.3 System of equations 31

3 Thermal softening, adiabatic shear banding, and torsion of bars **35**
- 3.1 Thermal softening effects of high-temperature deformation in aluminum and steel 35
  - 3.1.1 Equations of Motion 35
  - 3.1.2 Comparison with experiment: Aluminum 36
  - 3.1.3 Comparison with experiment: Steel 43
  - 3.1.4 Discussions 46
- 3.2 Adiabatic shear banding in steel 47
  - 3.2.1 Equations of Motion 47
  - 3.2.2 Data Analysis 48
  - 3.2.3 Adiabatic Shear Banding 51
  - 3.2.4 Discussions 55
- 3.3 Torsion of bars in copper 56
  - 3.3.1 Equations of motion 56
  - 3.3.2 Parameter identification and numerical simulations 58

4 Micro-indentation and anti-plane shear **63**
- 4.1 Dislocation structure during micro-indentation 63
  - 4.1.1 Plane strain wedge indentation 63
  - 4.1.2 Finite element formulation at Zero Dissipation 67

4.1.3 Newton-Raphson solution procedure 72
4.1.4 Numerical simulations and results 76
4.2 Anti-plane constrained shear 83
4.2.1 Energy density of excess dislocations and its extrapolation 83
4.2.2 Equations of Motion 84
4.2.3 Discretization and method of solution 87
4.2.4 Numerical simulations 90
4.2.5 Discussions 95

5 Conclusion **97**

Matlab supplement **99**

List of Figures

2.1 Unit cell structure of common metals. 6
2.2 Lattice defects in crystalline solids. 7
2.3 Slip in a zinc single crystal, Elam (1935). Reprinted by permission. 8
2.4 Example of most readily slip planes in BCC and FCC unit cells. 8
2.5 Dislocations traveling through the crystal lattice in response to an applied shear stress. 9
2.6 Width of dislocation. 10
2.7 Diagram for computing resolved shear stress. 11
2.8 Edge and screw dislocation. 12
2.9 Dislocation loop. 13
2.10 Sum of two dislocation lines. 13
2.11 Schematic illustration for Orowan relation. 14
2.12 Elasticity model. 15
2.13 Line tension of dislocation. 17
2.14 Schematic representation of Frank Read source. 18
2.15 From Frank-Read source to dislocation pile-up against grain boundary. . . . 19
2.16 Interaction of two straight edge dislocations lying on the same slip planes. . 19
2.17 Interaction of two straight parallel on different slip planes. 20
2.18 Decomposition of total strain. 29

3.1 Stress-strain curves for aluminum at the small strain rate $\dot{\epsilon} = 0.25\,s^{-1}$, for temperatures $300\,C,\ 400\,C,\ 500\,C$ shown from top to bottom. The experimental points are taken from Shi, McLaren, Sellars, Shahani, and Bolingbroke (1997a). 37
3.2 Stress-strain curves for aluminum at the strain rate $\dot{\epsilon} = 2.5\,s^{-1}$, for temperatures $300\,C,\ 400\,C,\ 500\,C$ shown from top to bottom. The experimental points are taken from Shi et al. (1997a). 37
3.3 Stress-strain curves for aluminum at the highest strain rate $\dot{\epsilon} = 25\,s^{-1}$, for temperatures $300\,C,\ 400\,C,\ 500\,C$ shown from top to bottom. The experimental points are taken from Shi et al. (1997a). 38
3.4 Theoretical fractional strain rate distribution for pure aluminum at the strain rate $\dot{\epsilon} = 0.25\,s^{-1}$, for temperatures $300\,C,\ 400\,C,\ 500\,C$ shown from bottom to top. 40
3.5 Theoretical fractional strain rate distribution across the initial yielding transition for pure aluminum at the strain rate $\dot{\epsilon} = 2.5\,s^{-1}$, for temperatures $300\,C,\ 400\,C,\ 500\,C$ shown from right to left. 40
3.6 Theoretical dislocation density distribution for pure aluminum at the strain rate $\dot{\epsilon} = 25\,s^{-1}$, for temperatures $300\,C,\ 400\,C,\ 500\,C$ shown from right to left. 41
3.7 Theoretical configurational temperature for pure aluminum at the strain rate $\dot{\epsilon} = 25\,s^{-1}$, for temperatures $300\,C,\ 400\,C,\ 500\,C$ shown from left to right. 41

3.8 Temperature as a function of strain for each of the nine stress-strain tests shown for aluminum in the preceding figures. The initial ambient temperatures are $300\,C,\ 400\,C$ and $500\,C$ (blue, black, and red) as seen on the left axis. Each group of three curves is for strain rates of $\dot{\epsilon} = 0.25\,s^{-1},\ 2.5\,s^{-1}$, and $25\,s^{-1}$, from bottom to top. 42

3.9 Stress-strain curves for steel at the small strain rate $\dot{\epsilon} = 0.1\,s^{-1}$, for temperatures $850\,C,\ 950\,C,\ 1050\,C$ shown from top to bottom. The experimental points are taken from Abbod, Sellars, Cizek, Linkens, and Mahfouf (2007). 43

3.10 Stress-strain curves for steel at the strain rate $\dot{\epsilon} = 1.0\,s^{-1}$, for temperatures $850\,C,\ 950\,C,\ 1050\,C$ shown from top to bottom. The experimental points are taken from Abbod et al. (2007). 44

3.11 Stress-strain curves for steel at the highest strain rate $\dot{\epsilon} = 10\,s^{-1}$, for temperatures $850\,C,\ 950\,C,\ 1050\,C$ shown from top to bottom. The experimental points are taken from Abbod et al. (2007). 44

3.12 Temperature as a function of strain for each of the nine stress-strain tests shown for steel in the preceding figures. The initial ambient temperatures are $850\,C,\ 950\,C$ and $1050\,C$ (blue, black, and red) as seen on the left axis. Each group of three curves is for strain rates of $\dot{\epsilon} = 0.10\,s^{-1},\ 1.0\,s^{-1}$, and $10\,s^{-1}$, from bottom to top. 45

3.13 Quasi-static stress-strain curves for steel at the strain rate $\dot{\varepsilon} = 10^{-4}$/s, for temperatures -190 °C, -73 °C, 25 °C, 70 °C shown from top to bottom. The experimental points are taken from Marchand and Duffy (1988). 49

3.14 Stress-strain curves for steel at the strain rate $\dot{\varepsilon} = 1000/\mathrm{s}$, for temperatures -190 °C, 25 °C, 134 °C shown from top to bottom. The experimental points are taken from Marchand and Duffy (1988). 50

3.15 Stress-strain curves for steel at the strain rate $\dot{\varepsilon} = 1000/\mathrm{s}$, for temperatures -73 °C, 70 °C, 250 °C shown from top to bottom. The experimental points are taken from Marchand and Duffy (1988). 51

3.16 Stress-strain curves for steel at the strain rates $\dot{\varepsilon} = 3300/\mathrm{s}$ and $\dot{\varepsilon} = 1600/\mathrm{s}$ shown from top to bottom, for room temperature. The experimental points are taken from Marchand and Duffy (1988). 52

3.17 Theoretical fractional strain rate distributions for steel for $\dot{\varepsilon} = 3300/\mathrm{s}$ at room temperature: (i) at strain $\varepsilon = 0.45$ (blue), (ii) at strain $\varepsilon = 0.47$ (green), (iii) at strain $\varepsilon = 0.49$ (black), (iv) at strain $\varepsilon = 0.497$ (red). 53

3.18 Plastic strain distributions for the strain rate $\dot{\varepsilon} = 3300$/s and room temperature at the strains $\varepsilon = 0.47$ (red), $\varepsilon = 0.49$ (blue), and $\varepsilon = 0.51$ (black). . . 53

3.19 Temperature distributions for the strain rate $\dot{\varepsilon} = 3300$/s and room temperature at the strains $\varepsilon = 0.46$ (blue), $\varepsilon = 0.48$ (green), and $\varepsilon = 0.505$ (red). The black curve is the empirical law proposed by Marchand and Duffy (1988). 54

3.20 Temperature at the center of the shear band ($\tilde{y} = 0$) for the strain rate $\dot{\varepsilon} =$ 3300/s and room temperature as the function of the strain. 55

3.21 Torsion of a single crystal bar. 57

3.22 The torque-twist curves at the twist rate $\dot{\phi} = 0.25°/\mathrm{s}$ and for room temperature: (i) sample 1: TDT-theory: black curve, experiment Horstemeyer et al. (2002): black circles (ii) sample 2: TDT-theory: red/dark gray curve, experiment Horstemeyer et al. (2002): red/dark gray circles. 59

3.23 Stress distribution $\tau(r)$ at the twist rate $\dot{\phi} = 0.25°/\mathrm{s}$ and for room temperature: (i) $\phi = 10°$ (black), (ii) $\phi = 30°$ (red/dark gray), (iii) $\phi = 50°$ (yellow/light gray). 60

3.24 Total density of dislocations $\rho(r)$ at the twist rate $\dot{\phi} = 0.25°/\text{s}$ and for room temperature: (i) $\phi = 10°$ (black), (ii) $\phi = 30°$ (red/dark gray), (iii) $\phi = 50°$ (yellow/light gray). 61
3.25 The torque-twist curves for the bars twisted at different twist rates and for room temperature: (i) $\dot{\phi} = 0.25°/\text{s}$ (black), (ii) $\dot{\phi} = 2.5°/\text{s}$ (red/dark gray), (iii) $\dot{\phi} = 25°/\text{s}$ (yellow/light gray). 62
3.26 (Color online) The torque-twist curves for the bars twisted at the same twist rate $\dot{\phi} = 0.25°/\text{s}$ and for three different ambient temperatures: (i) $T = 25°$C (black), (ii) $T = 250°$C (red/dark gray), (iii) $T = 500°$C (yellow/light gray). 62

4.1 Wedge indentation. 63
4.2 Energy density of dislocation network. 65
4.3 Boundary conditions for symmetric left-half. 67
4.4 Discretization of the domain Ω into bilinear isoparametric elements Ω^e, $e = 1, \ldots, n_e$. Each element Ω^e is obtained by the mapping (4.15) from the square $\hat{\Omega} = (-1, 1) \times (-1, 1)$ in the (ξ, η)-plane, with counterclockwise node numbering. 69
4.5 Example of bilinear shape functions in reference space $\hat{\Omega}$. 69
4.6 Smooth approximations of $|x|$ and its derivatives for $\nu = 20$. It can be seen that the consistent derivative in (4.19) on the left hand side has a bump close to $x = 0$ while the relaxed approximation of the derivative in (4.20) on the right hand side does not expose this behaviour. Furthermore, the second derivative of the relaxed formulation is strictly positive. 73
4.7 Quality of the approximate function for sign and absolute value functions with different ν. 74
4.8 Integrands for energy and the element internal force vector. 74
4.9 Quadrature on triangles, $\hat{T} = \{(x, y)^T \in \mathbb{R}^2 \mid x, y > 0, x + y < 1\}$. 75
4.10 Plot of internal force vector component for $\mathbf{f}^e_{\text{int}}(((1 - \xi)\hat{\mathbf{u}}^e_1 + (1 + \xi)\hat{\mathbf{u}}^e_2)/2)$. 75
4.11 Mesh distribution and the zooming near the indenter tip. 76
4.12 Load-displacement curve. 78
4.13 Experimental GND density of the slip system (iii) from Kysar, Saito, Oztop, Lee, and Huh (2010). Reprinted by permission. 79
4.14 Simulated GND density $\frac{1}{b}(\beta_{,x} \cos\varphi + \beta_{,y} \sin\varphi)$, $h = 200\mu$m. 80
4.15 Experimental lattice rotation w^e_z from Kysar et al. (2010). Reprinted by permission. 81
4.16 Simulated lattice rotation $[\frac{1}{2}(v_{,x} - u_{,y}) + \frac{1}{2}\beta] \times 180°/\pi$, $h = 200\mu$m. . . . 82
4.17 Simulated plastic slip, $h = 200\mu$m. 82
4.18 Dimensionless energy density $f(y) = \psi_m/\mu$. 84
4.19 The dimensionless energy density ψ_m/μ within two different range of ρ^g. The dashed line refers to Eq. (4.21), and the bold line refers to Eq. (4.23). . 85
4.20 Anti-plane constrained shear. 86
4.21 Stress-strain curves at the strain rate $\tilde{Q} = 10^{-13}$, for room temperature, and for $\gamma^* = 0.08$: (i) loading path OAB (black), (ii) load reversal BCD (red/dark gray), (iii) second load reversal DO (yellow/light gray), (iv) flow stress versus strain (dashed black curve). 88
4.22 Evolution of $\beta(\tilde{x})$ at the strain rate $\tilde{Q} = 10^{-13}$ and for room temperature during the loading along AB: (i) $\gamma = 0.02$ (black), (ii) $\gamma = 0.04$ (red/dark gray), (iii) $\gamma = 0.06$ (yellow/light gray). 89

4.23 N_g versus γ at the strain rate $\tilde{Q} = 10^{-13}$, for room temperature, and for $\gamma^* = 0.08$: (i) loading path (black), (ii) load reversal (red/dark gray), (iii) second load reversal (yellow/light gray). 90
4.24 N_r versus γ at the strain rate $\tilde{Q} = 10^{-13}$, for room temperature, and for $\gamma^* = 0.08$: (i) loading path (black), (ii) load reversal (red/dark gray), (iii) second load reversal (yellow/light gray). 91
4.25 $\tilde{\chi}(\tilde{c}/2)$ versus γ at the strain rate $\tilde{Q} = 10^{-13}$, for room temperature, and for $\gamma^* = 0.08$: (i) loading path (black), (ii) load reversal (red/dark gray), (iii) second load reversal (yellow/light gray). 92
4.26 Evolution of $\beta(\tilde{x})$ at the strain rate $\tilde{Q} = 10^{-13}$ and for room temperature during the load reversal along CD: (i) $\gamma = 0.02$ (black), (ii) $\gamma = 0.04$ (red/dark gray), (iii) $\gamma = 0.06$ (yellow/light gray). 92
4.27 The normalized back stress $\tilde{\tau}_B$ near the boundary versus γ at the strain rate $\tilde{Q} = 10^{-13}$, for room temperature, and for $\gamma^* = 0.08$: (i) loading path (black), (ii) load reversal (red/dark gray), (iii) second load reversal (yellow/-light gray). 93
4.28 The stress-strain curves for specimens with different sizes at the strain rate $\tilde{Q} = 10^{-13}$, for room temperature, and for $\gamma^* = 0.08$: (i) $c = 5.1$ micron (dashed), (ii) $c = 51$ micro (bold). 94
4.29 The stress-strain curves for the specimen loaded at different strain rates, for room temperature, and for $\gamma^* = 0.08$: (i) $\tilde{Q} = 10^{-13}$ (dashed), (ii) $\tilde{Q} = 10^{-11}$ (bold), (iii) $\tilde{Q} = 10^{-8}$ (dashed and dotted). 94

List of Tables

3.1 The values of δ and y_0 52

4.1 Material parameters of single-crystalline Nickel used for simulations. . . . 77

1 Introduction

From various experimental observations and theoretical considerations it is known that nucleation, multiplication and movement of dislocations are main causes for plastic deformations of single or polycrystalline materials. As crystalline solids begin to deform plastically, the number of dislocations increases, and the accumulations of these newly formed dislocations can impede the movement of dislocations leading to strain hardening. On the other hand, the movement of dislocations dissipate an essential portion of the plastic work into heat, leading to various phenomena such as thermal softening or the formation of adiabatic shear bands. Therefore, an understanding of the irreversible thermodynamics of crystals is essential to construct the physically meaningful dislocation mediated plasticity.

In connection with plastically deformed crystalline materials and the properties of dislocations an interesting question arises: Is the entropy of dislocations relevant to the thermodynamics of plasticity and should it be involved in the continuum dislocation theory? It is known that the energy of a single dislocation is so significant that the usual thermal fluctuations are completely ineffective in its nucleation or destruction. Thus, at first glance, the kinetic vibrational temperature of the crystalline body seems irrelevant to the formation and movement of dislocations. On the other hand, the entropy of dislocation disorder is small compared to the total entropy of the crystal, since dislocations involve only a relatively small amount of total atoms in the lattice; therefore, the phenomenological thermodynamics of crystal plasticity have completely ignored the entropy of dislocations. However, a theoretical concept of dislocation entropy introduced by Langer, Bouchbinder, and Lookman (2010), or LBL-theory for short, has shown that although dislocation entropy is small, it is still an essential quantity of dislocation-mediated plasticity that should be included in equations of motion for a system containing a large number of irregularly moving dislocations. The remarkable point here is to decouple the thermodynamic system of dislocated crystal into configurational and kinetic-vibrational subsystems. The former is characterized by the relatively slow, infrequent atomic rearrangements associated with the irreversible movement of dislocations, the latter being the rapid oscillations of atoms in a lattice. As an example, the generation of dislocation by Frank-Read or several cross slip sources is an extremely slow mechanism compared to the frequencies of atomic oscillations about their equilibrium positions. The governing equations of LBL-theory are based on the kinetics of thermally activated depinning of entangled dislocation dipoles and the irreversible thermodynamics of externally driven systems. These two ideas have been successfully implemented in a consistent thermodynamic dislocation theory to simulate the plastic flow of copper over fifteen decades of strain rate, and for the temperature between room temperature and about one third of the melting temperature, which shows full agreement with the groundbreaking experiments of Follansbee and Kocks (1988); Kocks and Mecking (2003); Meyers, Andrade, and Chokshi (1995) (see Langer (2015, 2016, 2017a, 2017c)).

In order to investigate the further application of this thermodynamic dislocation theory in modelling plastic deformations of materials subjected to thermomechanical processing, the theory was later modified and extended to simulate the stress-strain curves for aluminium

(Le & Tran, 2017; Le, Tran, & Langer, 2017) and steel alloys (Le et al., 2017) showing thermal softening behavior during plastic deformation. The focus of these studies is on the physical significance of various parameters occurring in equations of motion. Based on several physical deliberations, we argue which of these parameters are to be expected as material-specific constants, independent of temperature and strain rate, and thus as essential components of the theory. Excellent agreement with the experiments of Shi et al. (1997a) and Abbod et al. (2007) for aluminium and steel alloys, respectively, is also demonstrated, with each of them providing nine different stress-strain curves for three temperatures and three strain rates. Similarly, the LBL-theory was extended in predicting the formation of adiabatic shear bands (ASB) in steel HY-100 (see Le, Tran, and Langer (2018)), which shows a good quantitative agreement with the mechanical test performed by Marchand and Duffy (1988). The latter authors have observed ASB formation at high shear rates and low temperatures. In particular, they observed strong stress drops, significant temperature increases in emerging narrow bands, and strong strain localizations leading to crack information and failure; this is a challenge for this realistic physical theory, which not only simulates this behavior but also obtains additional information about the properties of structural materials. Recently, Le, Piao, and Tran (2018) has implemented an extension of this theory in the modeling of single crystal copper bars in the macro length scale exposed to torsion. The primary goal is to use a small set of physical parameters, expected to be independent of strain rate and temperature, to simulate the torque-twist curve showing the hardening behavior. This theoretical result is compared with the experimental result of Horstemeyer et al. (2002), in which single crystal copper bars of 99.999 purity are deformed under torsion testing.

The above mentioned LBL theory and its extensions are well suited for uniform plastic deformations where dislocations are neutral, i.e. the resulting Burgers vector vanishes. This source is commonly referred to as statistically stored dislocations. Cottrell (1964) has proposed a shorter and more precise name of redundant dislocations that will be used in this dissertation. In the case of nonuniform plastic deformations of specimens of micron sizes, another source occurs in addition to redundant dislocations to adapt to the plastic deformation gradient and ensure compatibility of the total deformation. Most scientists in dislocation theory call this source geometrically necessary dislocations, but the name of excess dislocations appears more precise from the point of view of statistical mechanics. It is widely accepted that, although the percentage of excess dislocations in severe plastic deformations of crystals is low, they play an important role in the development of the microstructure. This type of dislocations has been included in the basic framework of continuum dislocation theory (CDT), which was developed by Kondo (1952), Nye (1953), Bilby (1955), Kröner (1958), Berdichevsky and Sedov (1967) and Le and Stumpf (1996), in order to capture their influence on the formation of microstructure and the size effect. Nevertheless, the applicability of the theory became possible only in recent years, thanks to the advances in statistical mechanics and thermodynamics of the dislocation network reported in Berdichevsky (2005, 2006a, 2006b), where free energy is a logarithmic function of scalar dislocation density. This approach is physically appropriate because the energy of the microstructure increases linearly at low dislocation densities (where the interaction energy is negligible (Hirth & Lothe, 1992)), but becomes infinite when the dislocation density reaches a saturated value. Several successful examples of this theory can be found in Berdichevsky (2006a, 2006b), Kaluza and Le (2011), Kochmann and Le (2008, 2009a, 2009b), Le and Sembiring (2008a, 2008b, 2009), Le and Nguyen (2010), Le and Nguyen (2012, 2013). (see also nonlinear CDT proposed by Le and Günther (2014), Koster, Le, and Nguyen (2015)). Similarly, Baitsch, Le, and Tran (2015) has developed for the first time a finite element implementation for the indentation problems within this CDT. The numerical results discussed in this paper are compared with the experimental data of Kysar et al. (2010) and Dahlberg et al. (2014), where single crystals of nickel are deformed with a wedge penetrator at an angle of 90°. The qualitative agreement with these experiments again supports the proposed CDT.

As already mentioned, the CDT proposed by Berdichevsky can simulate the formation of microstructure and explain the size effects. However, the main disadvantage of this approach is the absence of redundant dislocations and configuration entropy responsible for isotropic hardening. For this reason Le (2018) comes to its revision by including these two missing quantities, the density of the redundant dislocations and the configuration temperature, as additional state variables in the constitutive equations of CDT. This newly improved theory is called Thermodynamic Dislocation Theory (TDT) for nonuniform plastic deformations. A study of crystals undergoing antiplane constrained shear within this advanced theory is presented by Le and Piao (2018), where they also consider the asymptotically accurate energy density of the dislocation network containing a moderately high density of excess dislocations (see Berdichevsky (2017)). To investigate the use of TDT for nonuniform plastic deformations, the anti-plane shear mode is re-examined in the study of Le and Tran (2018), where the dislocated crystals are exposed to loading, unloading, and then further loading in the opposite direction. The challenge of this analysis is to simulate the stress-strain curves with the Bauschinger effect and explain them using the physical mechanism of dislocation pile-up and the annihilation of excess dislocations during load reversal.

The aim of this dissertation is twofold. First, the extension of the LBL theory is proposed to include the thermal effects missing in the early versions of thermodynamic dislocation theory for uniform plastic deformations. It also extends the LBL theory to nonuniform plastic deformation for crystals in the macro length scale where the influence of excess dislocations can be ignored. Second, it investigates the use of thermodynamic dislocation theory for nonuniform plastic deformation, which is more advanced than its predecessor, the continuum dislocation theory. To simplify the analysis, the isotropic elastic properties of the single crystal and the theory of small strain are assumed. The outline of this dissertation follows: After this introduction the physical backgrounds are discussed in **chapter 2** with a short explanation of plastic deformation on a microscopic scale, basic concepts of dislocations and their properties and finally an introduction to thermodynamic dislocation theory for both uniform and non-uniform plastic deformations. Then **chapter 3** applies the extended LBL-theory to three specific mechanical tests: compression test of aluminum and steel exhibiting thermal softening, dynamic simple shear deformation of a thin steel tube showing the adiabatic shear banding, and torsion test of macrosized copper bars. **Chapter 4** presents a detailed discussion on CDT along with its numerical solution for the quasi-static indentation test. A numerical solution for an anti-plane shear deformation under load reversal is also discussed illustrating the application of the TDT to nonuniform plastic deformations. Finally **chapter 5** concludes the dissertation.

2 Physical backgrounds

2.1 Crystalline structure and plastic deformation

The classical theory of elastoplasticity deals with the phenomenological description of formal mathematical studies based on the simplifying assumptions that metals are macroscopically homogeneous and isotropic. For fine-grained metals that are quasistatically loaded, although precision is not often desired, these formal theories are sufficiently accurate in the elastic range and may represent the observed behavior in a plastic range. Under the conditions of dynamic and shock loading, however, the assumption that a metal is an isotropic homogeneous continuum becomes less plausible. Therefore, the ability to predict the behavior of metals with the help of classical elastoplasticity theories under fast loading condition decreases. As a consequence, the proper understanding of the plastic behavior of metals requires the study of their crystalline structure.

According to the report of Ewing and Rosenhain (1900) and the experimental discovery of the diffraction of X-rays by metallic crystals (von Laue, 1912), metals are crystalline solids, i.e. they essentially consist of atoms arranged in periodic geometric lattices. There have been many great studies on the relationship between the atomic structure and the plastic deformation of metals, and many of them have been performed on single or polycrystalline materials. This Section discusses the basic mechanisms of the plastic behavior of metals at the microscopic level (single crystals) to understand the underlying performance of metallic plastic deformation at the macroscopic scale from an experimental point of view.

2.1.1 Crystalline structure of metals

After X-ray diffraction analysis, the atoms in a metalic crystal are regularly arranged in a pattern repeated in three dimensions and consisting of aggregates of single crystals or grains. This arrangement of atoms is called the crystal lattice. The repetitive property of such a crystal lattice makes it sufficient to know only the structure of a unit cell, since the entire crystal lattice can be obtained from this unit cell by translational invariance. Due to the arrangement of the atoms in this unit cell, the crystal lattice structure is called face-centered cubic (fcc), body-centered cubic (bcc) or hexagonally densely packed (hcp), which are the most common atomic configurations in metals. Fig. 2.1a shows a body-centered cubic unit cell with one atom at each corner and one additional atom in the center of the cube. Typical metals with this crystal structure are alpha-iron, columbium, tantalum, chromium, molybdenum and tungsten. Fig. 2.1b shows the unit cell for face-centered cubic crystals. In addition to an atom at each of the eight corners, there is an atom at the central locations of each of the six cube faces. Aluminium, copper, gold, lead, silver and nickel are common fcc metals. The third common metallic crystal structure, densely packed hexagonally, is sketched in Fig. 2.1c, where the unit cell is a hexagonal prism containing six atoms at each of the upper and lower basal planes and three additional atoms in the middle layer (inside the prism), and for the upper and lower layers (based on the prism) the central atom is shared with the adjacent cell. Some typical metals with this structure are beryllium, titanium, magnesium, zinc and cadmium.

It is necessary to mention here the directed line between two atoms, the crystallographic directions, and the orientation of the planes containing atoms in the crystal lattice, the crystallographic planes. They are displayed using Miller indices, and this rule can be found in Callister (2007) for a detailed explanation.

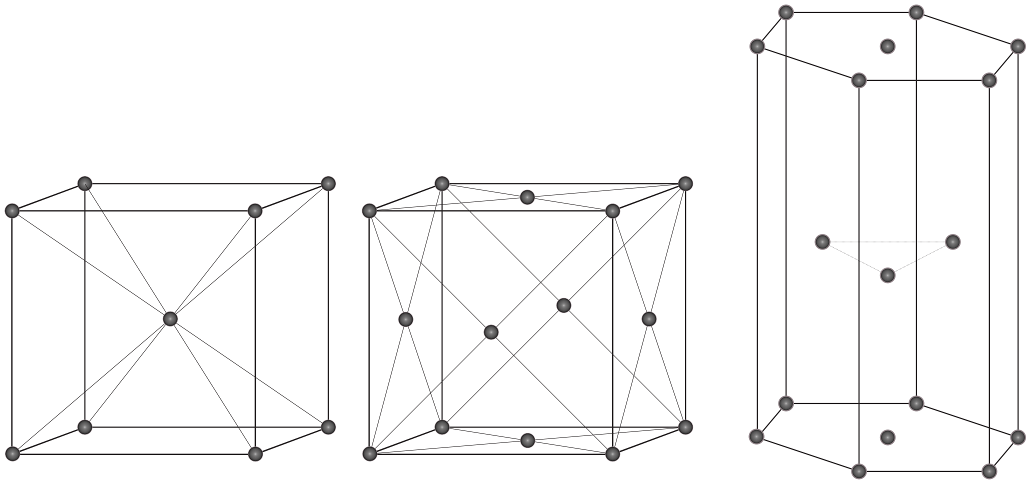

(a) Body-centered cubic. (b) Face-centered cubic. (c) Hexagonal close-packed.

Figure 2.1: Unit cell structure of common metals.

2.1.2 Lattice defects

Experimental observations have shown that crystal lattice configurations in real materials are hardly ever perfect. The term defect or imperfection is commonly used to describe anomalies from an ordered array of lattice points. There are several types of defects that can be roughly grouped by their dimensions.

- Zero-dimensional defects: The deviation from the periodic arrangement of the lattice includes foreign atoms located in the vicinity of only a few atoms. It is referred to as point defect. Vacancy, interstitial atom or impurity atom are examples of this type of defect (see Fig. 2.2a).

- One-dimensional line defects which are the subject of study in this dissertation and are named dislocations. These line defects are responsible for the phenomenon of slip, by which most metals deform plastically. Dislocations are groups of atoms that differ from their regular equilibrium locations. These dislocated atoms are very often additional or missing half-planes of atoms in the regular lattice (see Fig. 2.2b). These line defects are not only important for the explanation of plastic slip, but is also closely related to almost all other important mechanical phenomena such as work hardening, yield point, creep, fatigue and ductile fracture.

- Two-dimensional defects: These surface defects arise from the clustering of line defects into plane. Low-angle boundaries (see Fig. 2.2c), grain boundaries, stacking faults between two densely packed areas of the crystal that have alternative stacking sequences, or a twinned region of a crystal are examples of surface defects.

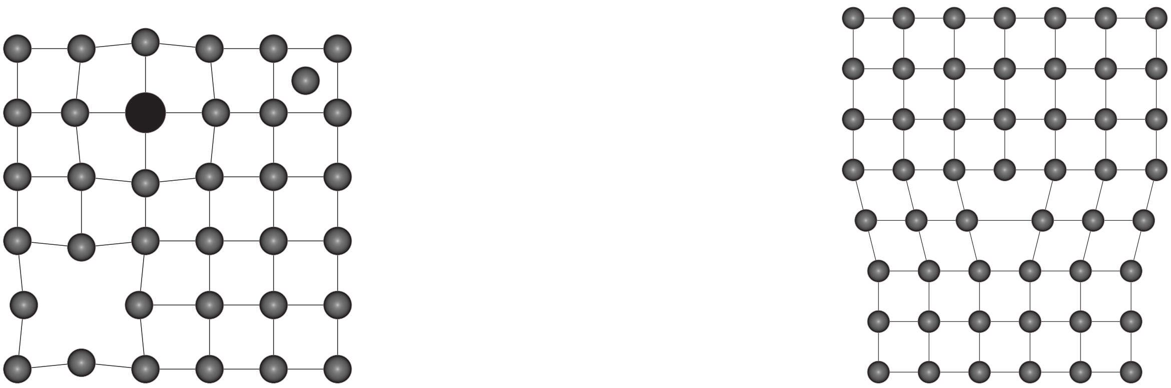

(a) Point defects.

(b) Line defects.

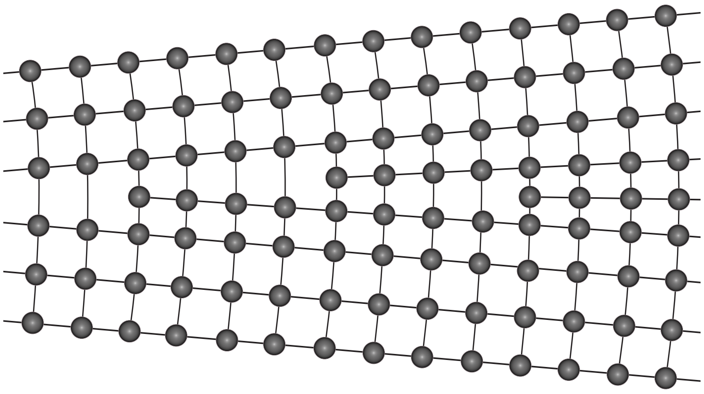

(c) Surface defects.

Figure 2.2: Lattice defects in crystalline solids.

2.1.3 Plastic deformation of single crystals

Deformation by slip One of the crucial characteristics of the crystalline structure is its ability to glide easily on certain crystallographic planes, the so-called slip planes, and on certain crystallographic directions, the so-called slip directions. As reported in Ewing and Rosenhain (1900), plastic deformation occurs in metals as these special families of crystal planes slide over each other in certain slip directions. Thanks to the technological development of recent years, it is possible not only to grow the single crystals large enough for mechanical tests, but also to observe the fine structure of the slip lines at high magnification with the electron microscope. Therefore, scientists can carry out many typical mechanical experiments such as torsion, shear, bending, tensile/compression or indentation tests on single crystals with different types of material in order not only to obtain the stress-strain behavior, but also to record the development of the deformed structure. As an illustration, Fig. 2.3 shows an experiment with plastically deformed zinc single crystals that captures information about the plastic slips that occur along the most favorable slip planes and directions.

These experimental results also suggest that gliding is generally easiest on the glide plane,

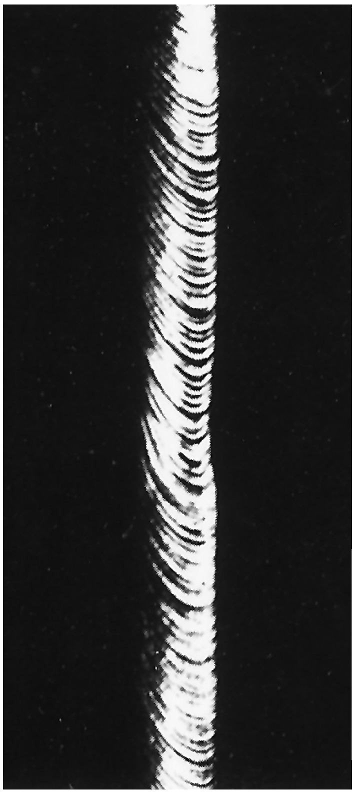

Figure 2.3: Slip in a zinc single crystal, Elam (1935). Reprinted by permission.

which is the one with the highest atomic density along the direction of the shortest interatomic distances (densely packed planes and directions). For example, using the Miller index rule, one can describe the easiest slip planes $\{1\,1\,1\}$ in $\langle 1\,1\,1\rangle$ directions for FCC metals; while for BCC metals, these slip planes are $\{1\,1\,0\}$, $\{1\,1\,2\}$, and $\{1\,2\,3\}$ with the slip directions $\langle 1\,1\,1\rangle$. For HCP metals, the choice of slip directions is more limited because only a few slip systems (plane and slip direction) exist. Typical slip planes of BCC and FCC are sketched in Fig. 2.4.

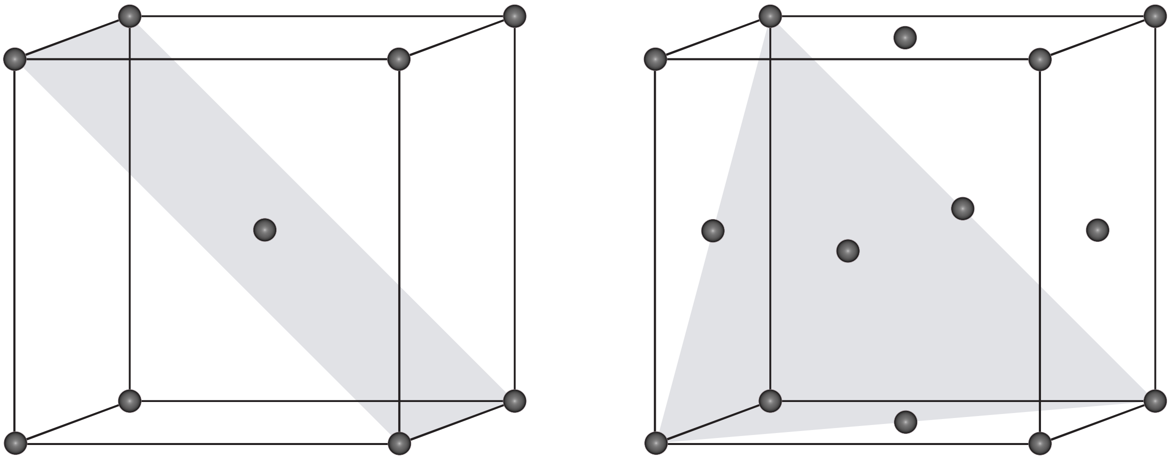

Figure 2.4: Example of most readily slip planes in BCC and FCC unit cells.

Slip by dislocation motion The theoretical estimation of the critical shear strength of the crystal at which plastic slip occurs was first found by Frenkel (1926). The theoretical shear strength can be calculated by assuming that the slip is caused by the shearing of one block of atoms over another. This estimated value is given by

$$\tau_{cr} = \frac{\mu}{2\pi}, \tag{2.1}$$

where the typical shear modulus μ for metals lies in the range of 20 to 150 GPa. Therefore, Eq. (2.1) predicts that the maximum theoretical shear strength will be in the range of 3 to 30 GPa. From various experimental measurements of the yield strength we know, however, that this estimated theoretical value is at least three or four orders of magnitude greater than the observed one. Because of this large discrepancy, it must be concluded that the plastic slips in crystals is realized by a different mechanism than the physical shearing of planes of atoms passing over another. The concept of dislocation, introduced independently by Taylor (1934), Polanyi (1934) and Orowan (1934), explain this discrepancy in the following way: The plastic slip is the result of dislocation motion.

Fig. 2.5 illustrates the movement of the dislocation through the crystal exposed to shear stress. Initially, the dislocation in A has an upper half-plane of atoms, as shown in Fig. 2.5a. With a sufficiently large shear stress, half plane A is forced to move to the right, and in the meantime the interatomic bonds of plane B are broken by the slip plane. Consequently, the upper half plane of B becomes an additional half plane of atoms, while the half plane of A is connected to the lower half plane B, see Fig. 2.5b. Thus, the dislocation moves from A to B. This process is repeated continuously until the additional half plane of the atoms reaches a free surface, see Fig. 2.5d. This leads to a sliding step of one atomic distance for the simple cubic lattice.

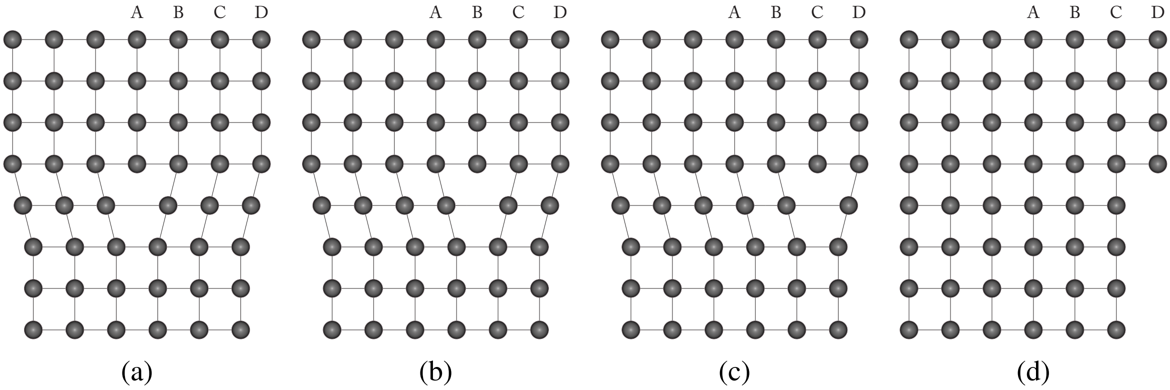

(a) (b) (c) (d)

Figure 2.5: Dislocations traveling through the crystal lattice in response to an applied shear stress.

It is interesting to calculate the required stress to drive a dislocation through a crystal continuously in a certain direction, called Peierls-Nabarro stress τ_p:

$$\tau_p \approx 3\,\mu\,\exp\left(\frac{-2\pi w}{b}\right), \tag{2.2}$$

where b is the distance between the atoms in the slip direction and w is the width of the dislocation (see Fig. 2.6). If w is several atomic spacings in dimension, the dislocation is wide. Dislocation slip occurs most easily with wide dislocations because the highly distorted region in the core of the dislocation is not located at a particular atom in the crystal lattice. For simple ductile metals, the dislocation width is normally in the order of 10 atomic distances. Assuming the minimum dislocation width in the metal is $w = 3b$, the maximum shear stress is roughly estimated: $\tau_{p,max} \approx 2\,\mu\,10^{-8}$. This calculation is accurate enough to show that the stress required to move the dislocation in a metal, which is the main cause of slip and plastic deformation, is quite small.

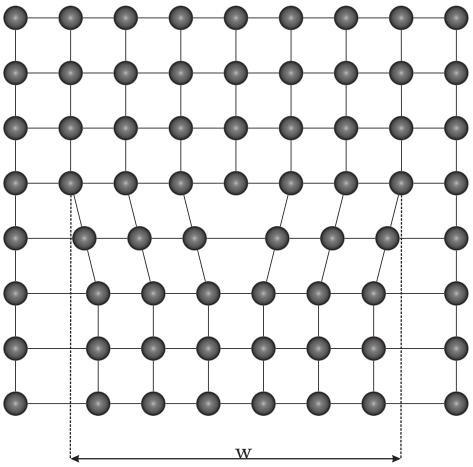

Figure 2.6: Width of dislocation.

Critical resolved shear stress As already mentioned, a plastic slip occurs due to the gliding of extra half plane of atoms on a slip plane in a slip direction as a response to applied shear stress. This shear stress component is still present for a pure tensile or compression test, but not in the directions parallel or perpendicular to the direction of the applied uniaxial load. This shear stress component is referred to as resolved shear stress. Consider a cylindrical single crystal with a cross-sectional area of A exerted by the tensile force F, as outlined in Fig. 2.7. Let the angle between the normal to the slip plane and the tensile axis be ϕ, while λ denotes the angle between the slip direction and the tensile axis. Note that in general $\phi + \lambda \neq 90°$ since the tensile axis, the normal to the slip plane, and the slip direction do not necessarily lie in the same plane. In the slip direction, the shear component of force $F\cos\lambda$ acts on the slip surface with an area of $A/\cos\lambda$, so the resolved shear stress is:

$$\tau = \frac{F\cos\lambda}{A/\cos\phi} = \frac{F}{A}\cos\phi\cos\lambda. \tag{2.3}$$

As reported in Schmid (1924), a single-crystal starts to slip when the resolved shear stress on a slip plane reaches a critical value τ_{cr}. This parameter is a constant for each specific material at a given temperature. This result is well known as Schmid's law.

Strain hardening Work hardening is one of the main features of the plastic deformation of metals and is defined as the increase in stress required to produce slip with increasing shear strain. The micro-mechanism of this phenomenon can generally be divided into two categories: stack hardening and entanglement hardening. The detailed explanation is as follows:

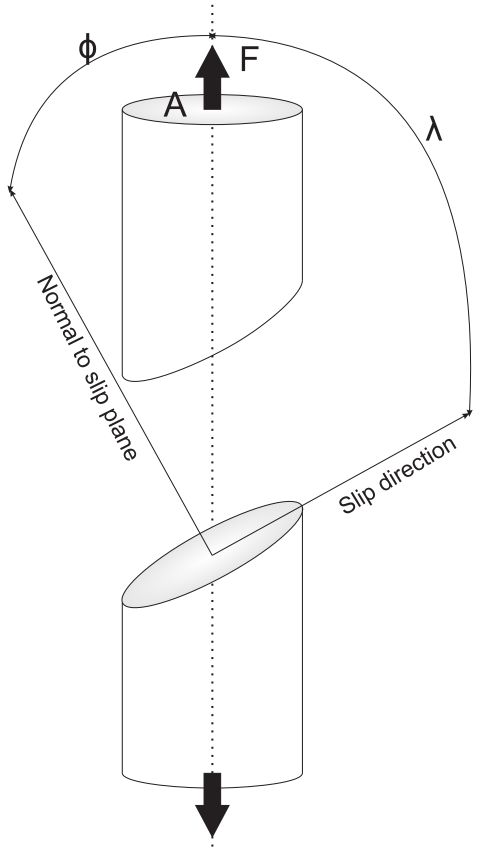

Figure 2.7: Diagram for computing resolved shear stress.

- Stack hardening occurs due to the fact that dislocations on slip planes accumulate against barriers in the crystal. Such accumulations create the back stress that counteracts the stress applied to the slip plane and therefore causes kinematic hardening with respect to the specific slip system. In this case, the barriers created by the glide dislocations on intersecting slip planes can merge to form new immobile dislocations (sessile dislocations). These dislocations with low mobility act as obstacles to dislocation movement until the stress is increased to a sufficiently high level to break them down.

- Entanglement hardening is actually an isotropic hardening for a certain slip system. This phenomenon occurs when dislocations moving in the slip plane pass through other dislocations intersecting the active slip plane. The dislocations passing through the active slip plane are called dislocation tangles (or dislocation forests). The cross slip or jogging turns out to be an important dislocation cutting process in this case.

It should be noted that moving dislocation is influenced not only by stack hardening but also by entanglement hardening. The total hardening is the sum of both contributions.

2.2 Fundamental of dislocations

As mentioned in the previous section, dislocations are the most important line defects in crystals as they are responsible for almost all aspects of plastic deformation of metals. In this Section, the basic concepts of dislocations such as dislocation line, Burgers vector, types of dislocations, or the population of dislocations in a crystal are discussed.

Dislocation types Dislocations are regions in which atoms lie outside their regular positions in the periodic crystal lattice. There are mainly two basic types of dislocations, edge dislocation and screw dislocation.

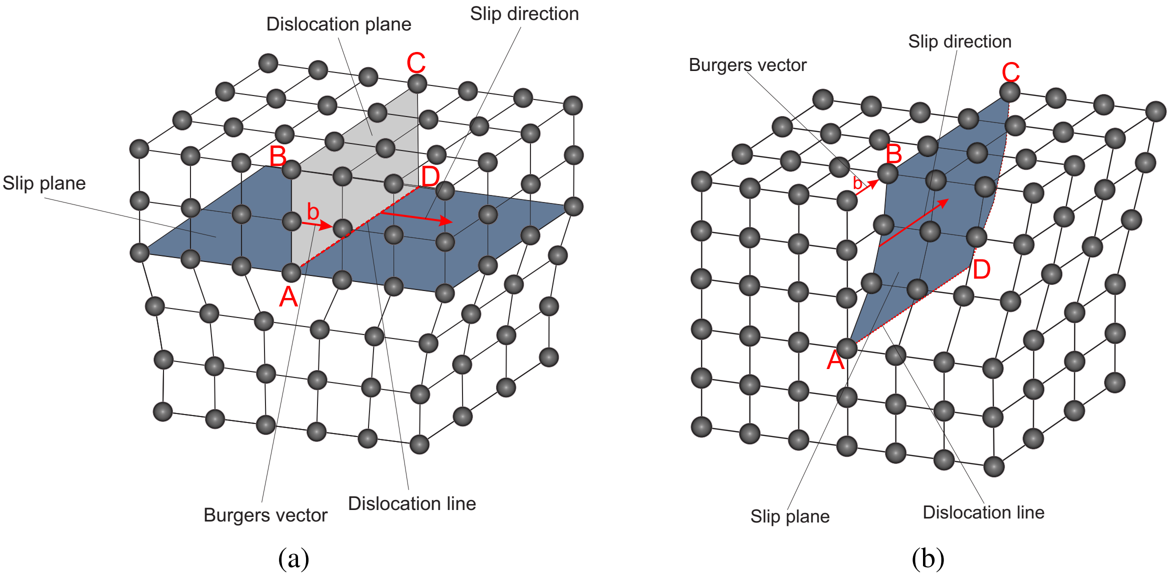

Figure 2.8: Edge and screw dislocation.

Taylor (1934), Polanyi (1934) and Orowan (1934) are pioneers who introduced edge dislocation to explain the significant discrepancy between experiment and theoretical estimation of critical shear strength. As shown in Fig. 2.8a, this type of line defect is produced by inserting an additional half-plane of atoms ABCD into a perfectly arranged lattice structure whose edges lie in a crystal. The line AD is the core of the edge dislocation, known as the dislocation line. This dislocation plane slides on a slip plane through the crystal and follows the slip direction perpendicular to the dislocation line AD. Hence the Burgers vector b is also perpendicular to the dislocation line. This vector is defined as the resulting vector needed to complete a Burgers circuit around the dislocation core (for metals, the length of the burger vector corresponds to the interatomic distance). The second primary type of dislocation is screw dislocation, first introduced by Burger (1939). It is usually generated by applying shear stress to create distortions so that a crystal shift occurs on one side of the slip plane ABCD relative to the other side in the slip direction, see Fig. 2.8b. Therefore, the dislocation line AD, in this case, is parallel to the Burgers vector b.

Dislocation loop Dislocations in real materials are more complex and rarely straight lines. In general, a dislocation involves a combination of both types of dislocations called a mixed dislocation. These mixed dislocations are usually represented in the form of curves or loops. As can be seen in Fig. 2.9, a dislocation loop in a slip plane consists of many small segments of the dislocation line that can be resolved into edge and screw components. The dislocation loop is the edge at points A and C and the screw at points B and D, while it is a mixed edge and screw along most of its lines. However, the Burgers vector remains unchanged

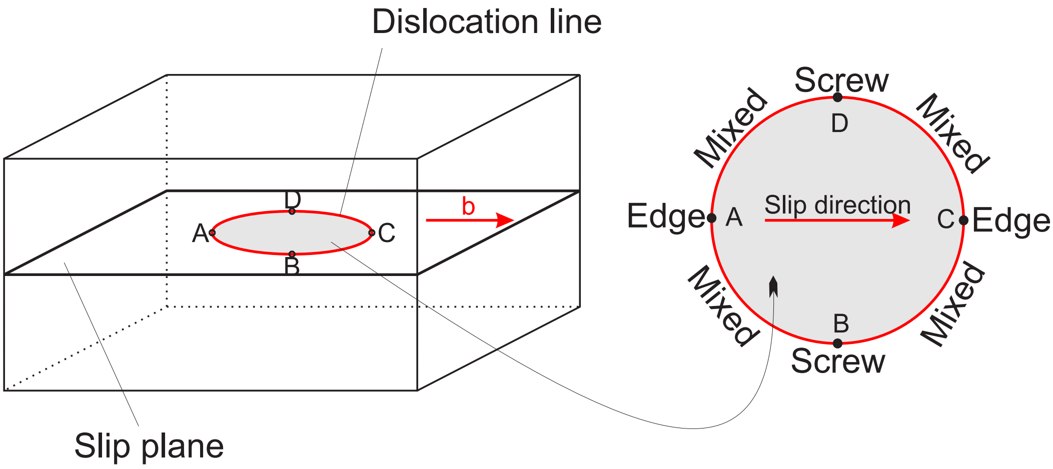
Dislocation line
Slip plane
A
B
C
D
b
Screw
Mixed
Mixed
Edge
Edge
Slip direction
Mixed
Mixed
Screw
A
B
C
D

Figure 2.9: Dislocation loop.

throughout the loop.

At this point it should be mentioned that a dislocation line is a boundary between a slipped and a un-slipped area. In general, it cannot end inside the crystal, but at the free surface or a grain boundary. Therefore, it must be closed or branch to other dislocations. Fig. 2.10 illustrates an example of the two separate dislocation lines with the Burger vectors $\mathbf{b_1}$ and $\mathbf{b_2}$, which form an immovable node, resulting in a third dislocation with the Burger vectors $\mathbf{b_3}$, where the small eclipses indicate the Burgers circuit according to the dislocation line sense with the ”right hand” rule. From the diagram it follows that $\mathbf{b_1} + \mathbf{b_2} = \mathbf{b_3}$, which means that the sum of the Burgers vector must be zero for all dislocations hitting a node.

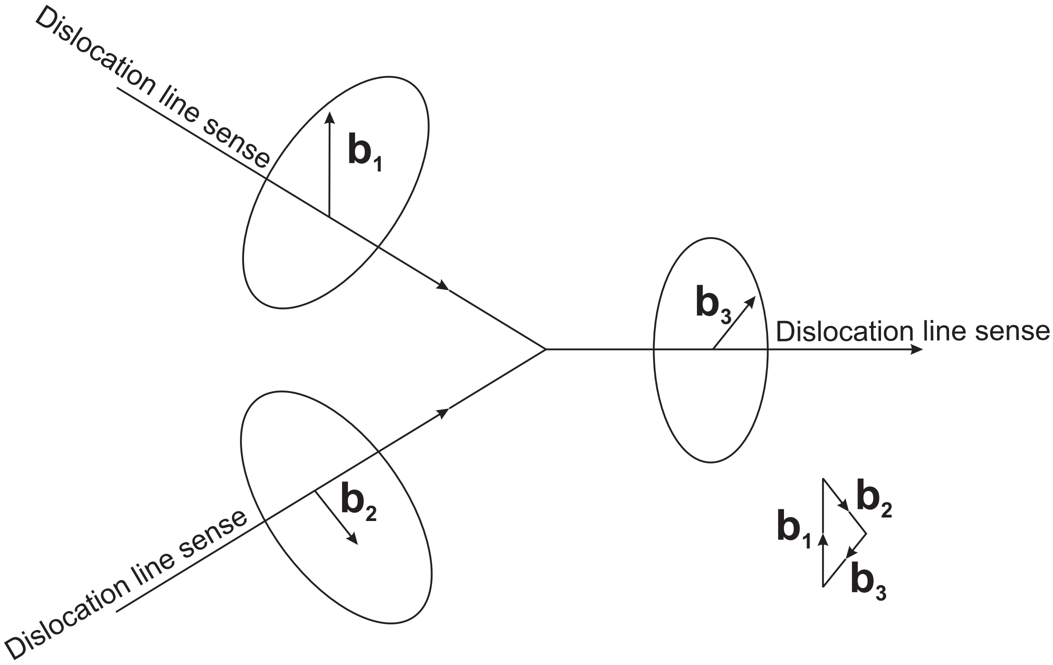
Dislocation line sense
b1
b3
Dislocation line sense
b2
Dislocation line sense
b1
b2
b3

Figure 2.10: Sum of two dislocation lines.

Dislocation density The dislocation density, usually denoted ρ, is defined by the total length of the dislocation lines per unit volume of the crystal. In a well annealed crystal, ρ is usually in a range from 10^{10} to 10^{12} m^{-2}. In a heavily cold-rolled metal, it is 10^{14} to

$10^{15}\ \mathrm{m}^{-2}$. The second way to determine the dislocation density, which seems to be more applicable, is to count the number of dislocations passed through a unit area of a planar surface of the crystal. This alternative definition provides a convenient way to predict the average distance between dislocations in a network of density ρ. Indeed, if we have a ρ intersections per unit area, then this means that each intersection occupies $1/\rho$ of the unit area. Thus, the distance between neighboring dislocations is in the order of $1/\sqrt{\rho}$.

Plastic strain due to dislocation movement To illustrate how the movement of dislocations is related to macroscopic plastic strain, we consider a single crystal with the volume hld that for simplicity's sake contains only edge dislocations, as shown in Fig. 2.11a.

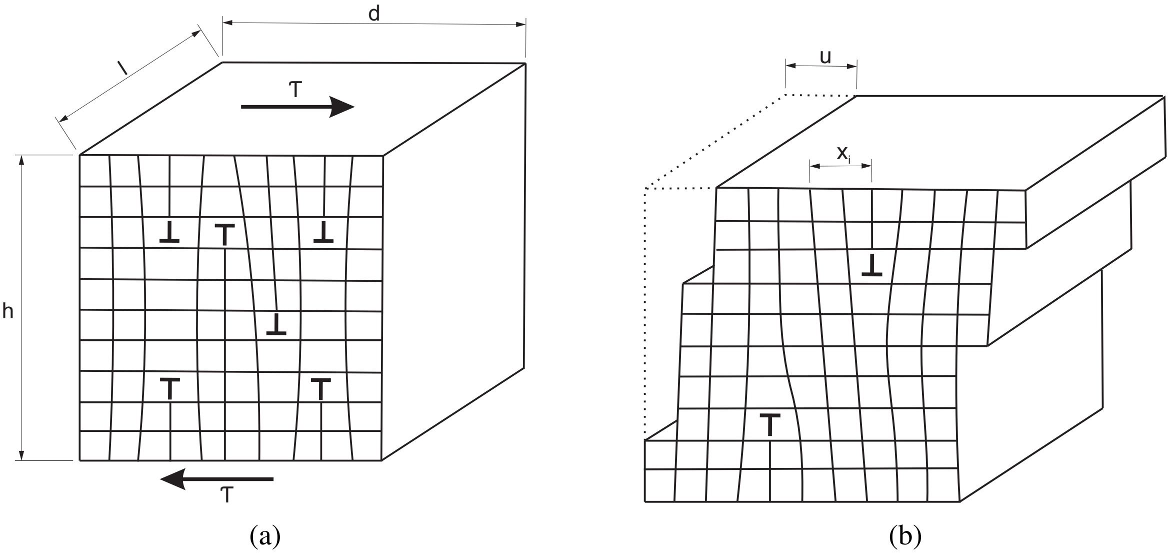

(a) (b)

Figure 2.11: Schematic illustration for Orowan relation.

These dislocations glide under a sufficiently high shear stress. Therefore, the upper side is plastically displaced by u relative to the lower side, see Fig. 2.11b. If a dislocation goes all the way through the crystal a distance d, it adds b to the total displacement u. Assuming that the dislocation would not have completely gone through the crystal, but only a distance x_i, then it contributes a displacement $(x_i/d)b$. So if there are N moving dislocations, the total displacement is

$$u = \frac{b}{d}\sum_{i=1}^{N} x_i,$$

and the plastic shear strain ε is given by

$$\varepsilon^{pl} = \frac{u}{h} = \frac{b}{hd}\sum_{i=1}^{N} x_i.$$

Denote the mobile dislocation density by $\rho = Nl/hld$ and the average moving distance of N dislocations by

$$\bar{x} = \frac{1}{N}\sum_{i=1}^{N} x_i.$$

Then the plastic shear strain is simplified to

$$\varepsilon^{pl} = b\rho\bar{x}. \tag{2.4}$$

The strain rate is therefore

$$\dot{\varepsilon}^{pl} = b\rho\bar{v}. \tag{2.5}$$

This relation is called the Orowan equation. Note that ρ in the above equations is the mobile dislocation density, because those that do not move are not included in the plastic shear strain.

2.3 Properties of dislocations

2.3.1 Stress field and self energy of dislocations

A dislocation line is surrounded by an elastic stress field that can lead to interactions with other adjacent atoms or other lattice defects like dislocations or vacancies. Apart from the region near the dislocation core, the theory of elasticity can be applied as a suitable continuum approach to obtain the stress around dislocation of both types, screw and edge dislocation. The results shown here are expressed in the cylindrical coordinate system (r, θ, z) using the Volterra (1907) model, as shown in Fig. 2.12, without details of the derivation.

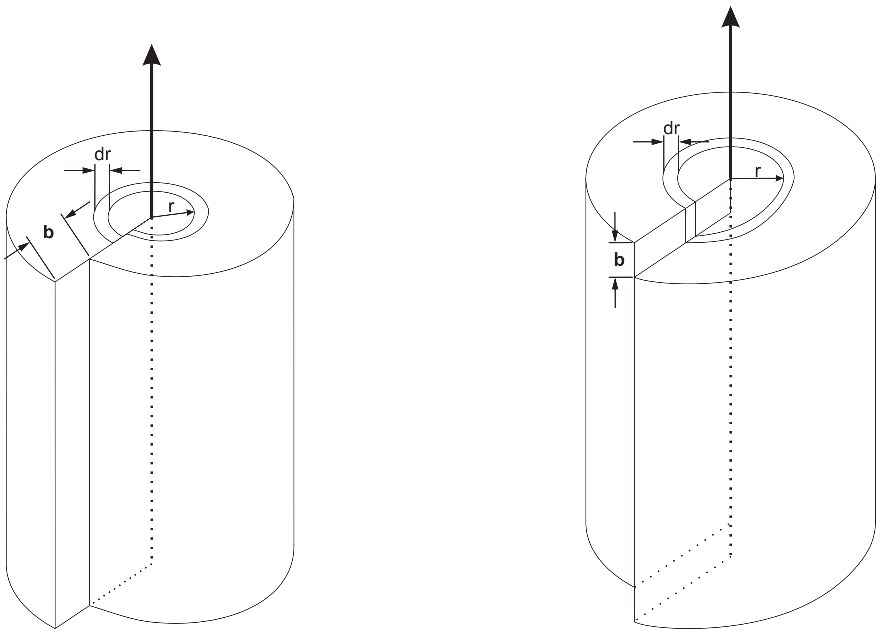

(a) Edge dislocation (b) Screw dislocation

Figure 2.12: Elasticity model.

For a screw dislocation, the stress field is

$$\sigma_{\theta z} = \frac{\mu b}{2\pi r}, \qquad \sigma_{rr} = \sigma_{\theta\theta} = \sigma_{zz} = \sigma_{r\theta} = \sigma_{rz} = 0. \tag{2.6}$$

For an edge dislocation the stress field becomes more complicated. Its non-zero components are:

$$\begin{aligned}\sigma_{rr} &= \sigma_{\theta\theta} = -\frac{\mu b \sin\theta}{2\pi(1-\nu)r},\\ \sigma_{zz} &= -\frac{\mu b \sin\theta}{\pi(1-\nu)r},\\ \sigma_{r\theta} &= \frac{\mu b \cos\theta}{2\pi(1-\nu)r}.\end{aligned} \tag{2.7}$$

Two conclusions can be drawn from this result: i) The stress fields of dislocations are long-range, but decay rapidly with increasing distance r from the dislocation core. ii) The calculated stresses for both cases are proportional to $1/r$. Thus the stress fields diverge to infinity as r tends towards zero. Since no real materials can withstand this infinite stress field, the elastic theory can be applied to obtain the stress concentration only for $r \geq r_{min}$. According to Weertman and Weertman (1964), the minimum core radius of the dislocation where elasticity theory is still applicable should be $r_{min} = 5b$, where b is the length of the Burger vector.

Due to this stress field around a dislocation line, elastic energy exists in this area, namely self-energy or stored dislocation energy. According to the assumption $r_{min} = 5b$ of Weertman and Weertman (1964) the self-energy per unit length of a dislocation takes the following form

$$E_{screw} = \frac{1}{2}\int_{5b}^{R} \sigma_{\theta z} b \, dr + E_{core} = \frac{\mu b^2}{4\pi} \ln\frac{R}{5b} + E_{core}. \tag{2.8}$$

For an edge dislocation we have

$$E_{edge} = \frac{1}{2}\int_{5b}^{R} \sigma_{r\theta} b \, dr + E_{core} = \frac{\mu b^2}{4\pi(1-\nu)} \ln\frac{R}{5b} + E_{core}, \tag{2.9}$$

where the core energy per unit length E_{core} is normally about one fifteenth of the total stored energy. Typical values for an annealed crystal $R = 100$ nm and $b = 0.2$ nm can be used to calculate the numerical value of the dislocation self-energy. An additional formula for the self-energy of the mixed dislocation per unit length whose Burgers vector is inclined at an angle θ from the dislocation line is as follows

$$E_{mixed} = \frac{\mu b^2}{4\pi}\left(\cos^2\theta + \frac{\sin^2\theta}{1-\nu}\right)\ln\frac{R}{5b} + E_{core}. \tag{2.10}$$

After some simplified steps (see Dieter and Bacon (1986)) one can conclude that the stored energy per dislocation length is proportional to the square of its Burgers vector $E_{elastic} = \alpha\mu b^2$ with $\alpha \approx 0.5 \div 1.0$, which means that the introduction of a new dislocation increases the free energy of the system. In nature, the system always tends to minimize its free energy; therefore, a crystal with dislocations is thermodynamically unbalanced. When the crystal is free of load, it will attempt to reduce its free energy by eliminating dislocations in a process such as annealing.

2.3.2 Forces on a dislocation

As we know, dislocation motion is the underlying mechanism of plastic deformation in crystalline metals. To enable this dislocation motion, the crystal must be subjected to a sufficiently large force so that the resolved shear stress τ on the slip plane is higher than its critical value. This leads to the concept of the force acting on the dislocation line. A special feature of this applied force is that it always acts in a direction perpendicular to the dislocation line.

Suppose a cube-shaped crystal of length L containing an edge dislocation[1] is subjected to a resolved shear stress τ. If the dislocation moves a distance x, the displacement of the upper half of the atoms with respect to the lower half is $(x/L)b$. With the shear force applied to the top, τL^2, the work done when the dislocation moves is equal to

$$W = \tau L^2 \left(\frac{x}{L} b\right) = \tau x b L.$$

Then, the magnitude of force per unit length acting on the dislocation can be expressed as

$$F = \frac{1}{L}\frac{dW}{dx} = \tau b. \tag{2.11}$$

Let us now consider what happens when a dislocation line is exposed to this applied shear force. In reality, dislocations are usually anchored somewhere in the crystal due to the immobile dislocation nodes. Consider a dislocation segment AB of length l held at its ends as shown in Fig. 2.13. The AB line is first straight, because the strain energy of this dislocation tries to reach its lower limit by reducing the total length of the line. Under force, however, the segment begins to bow out. The dislocation bows out until the line tension balances this applied force as follows

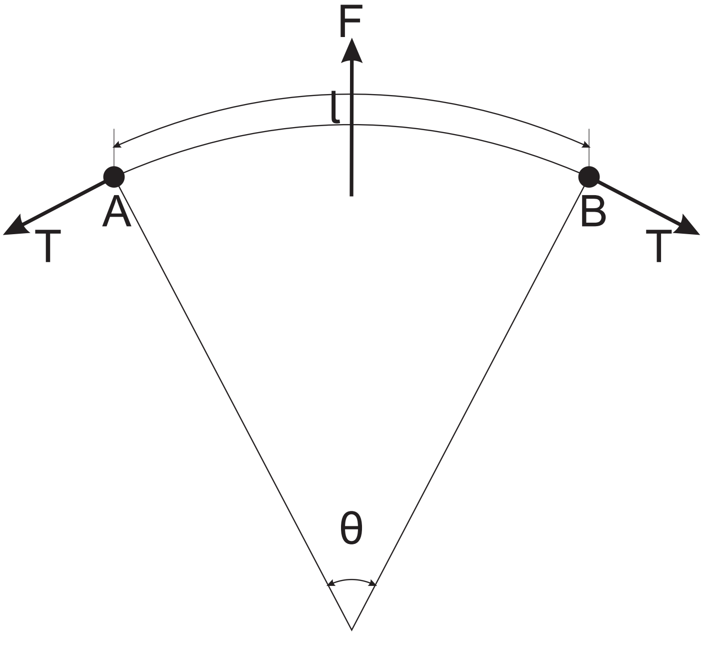

Figure 2.13: Line tension of dislocation.

$$\tau\, b\, l = 2T \sin\frac{\theta}{2}. \tag{2.12}$$

With $l = r\theta$ and $\sin\theta/2 \approx \theta/2$ for small angle θ, one obtains

$$\tau = \frac{T}{br}. \tag{2.13}$$

---

[1] The case of a screw or mixed dislocation is similar.

As presented in the previous Section, the line tension is nothing more than the elastic strain energy per unit length $T = \alpha\mu b^2$. We finally get the stress required to bend a dislocation into a circular segment of the radius r

$$\tau = \frac{\alpha\,\mu\,b}{r}. \tag{2.14}$$

Let us just further increase the resolved shear stress τ. As the relationship in Eq. (2.14) shows, the radius of the curve AB decreases until r reaches its minimum value $r_{min} = l/2$. Assuming $\alpha = 0.5$, the maximum resolved shear stress gives the following values

$$\tau_{max} = \frac{\mu\,b}{l}.$$

As long as $\tau > \tau_{max}$, the dislocation curve AB continues to expand and becomes unstable so that the two sides swing around and come into contact on the back side of the two immovable nodes. These contact parts of the dislocation curve have the same Burger vector, but are of the opposite sign, so they annihilate each other. This process creates a dislocation loop and the dislocation line AB can be imagined as a dislocation source. If the resolved shear stress remains $\tau > \tau_{max}$, the source would release endlessly dislocation loops. The whole process of this remarkable phenomenon, known as Frank-Read source (see Frank and Read (1950)), is schematically illustrated in Fig. 2.14.

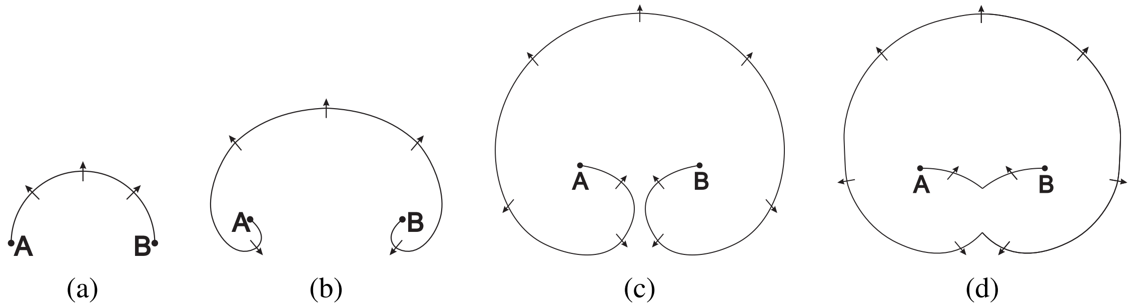

Figure 2.14: Schematic representation of Frank Read source.

The Frank Read source presented here is one of many different natural processes that cause dislocation nucleation. Another well-known example is the Bardeen-Herring-source, known as multiple cross slip mechanism for dislocation generation. These sources trigger a series of dislocations that lie in the same slip planes. The head dislocation of this series encounters obstacles such as grain boundaries or sessile dislocations, and further loop expansion is prevented, as illustrated in Fig. 2.15. The next dislocation loops then accumulate behind the leading dislocation. Due to this event, the leading dislocation acts on a high stress concentration since it is exposed not only to the applied shear stress but also to the elastically interactive stress. On the other hand, the dislocations in the vicinity of the barriers generate a back stress which acts against their movements in the slip direction.

2.3.3 Interaction of dislocations

Let us first consider the interaction between two parallel edge dislocations lying on the same plane for the sake of simplicity. They can either have the same sign or different sign. When

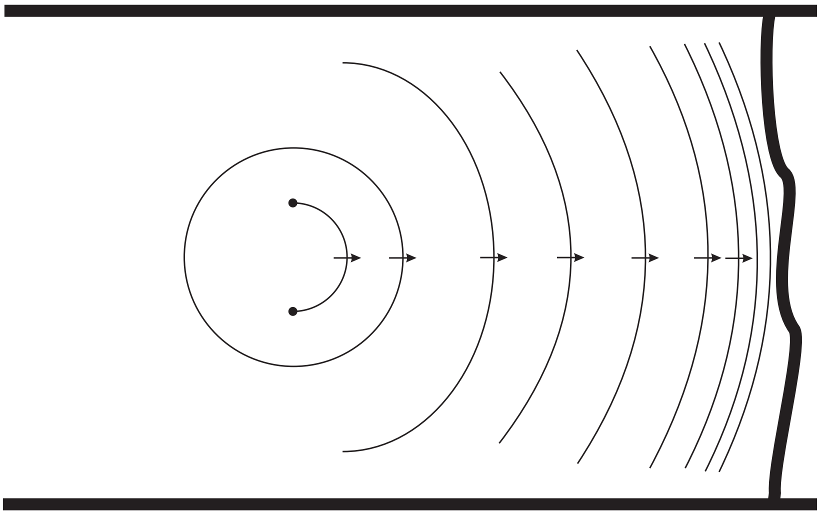

Figure 2.15: From Frank-Read source to dislocation pile-up against grain boundary.

the distance between dislocations are considerable for both cases, the total elastic energy per unit will be calculated from the Eq. (2.9)

$$E_{edge} = \frac{2\mu b^2}{4\pi(1-\nu)} \ln \frac{R}{5b}.$$

However, if they come closer, the configuration of like sign dislocation can now be considered as only one single dislocation with a Burgers vector magnitude $2b$, and the elastic energy per unit will be

$$E_{edge} = \frac{\mu (2b)^2}{4\pi(1-\nu)} \ln \frac{R}{5b}.$$

One can easily see that this is twice the energy of the dislocations when a far distance separates them; thus, the dislocations will tend to repel each other to reduce their total elastic energy. For the case when the dislocations of opposite sign are close together, the length of their Burgers vector will be zero; thus, they will attract each other, run together, and annihilate each other to reduce their total elastic energy, (see Fig. 2.16). The interaction between dislocations lying not in the same plane can be described by the interactive forces between them. Consider two edges dislocations lying parallel to z-axis as in Fig. 2.17a, the forces acting on II due to the presence of I at origin takes the form

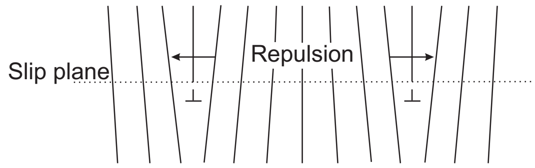

(a) Same sign.

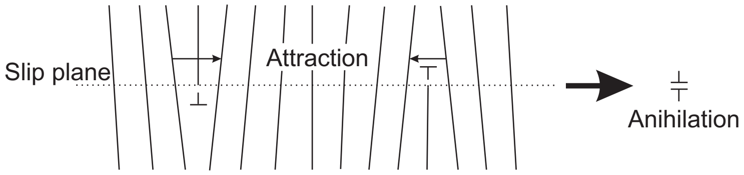

(b) Opposite sign.

Figure 2.16: Interaction of two straight edge dislocations lying on the same slip planes.

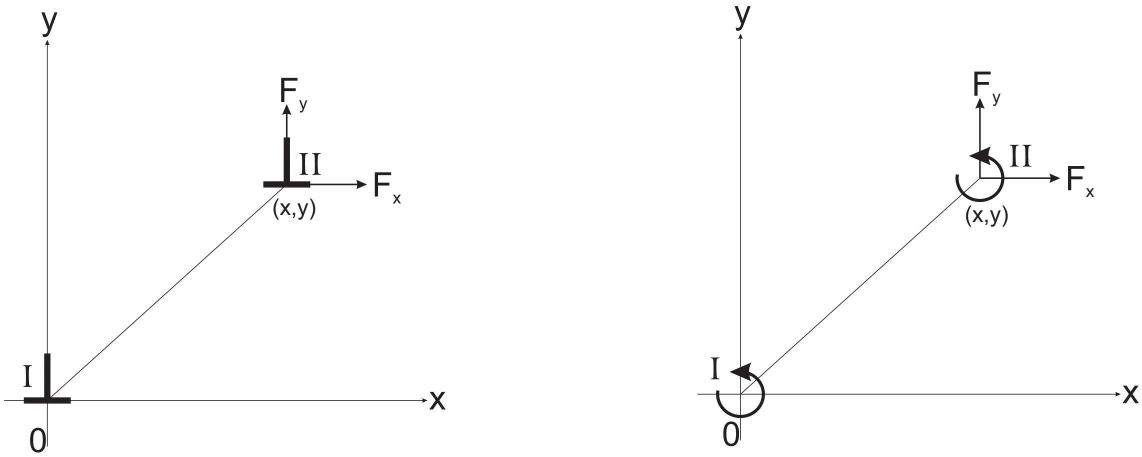

(a) Edge dislocation. (b) Screw dislocation.

Figure 2.17: Interaction of two straight parallel on different slip planes.

$$F_x = \frac{\mu b^2}{2\pi(1-\nu)} \frac{x(x^2-y^2)}{(x^2+y^2)^2} \quad \text{and} \quad F_y = \frac{\mu b^2}{2\pi(1-\nu)} \frac{y(3x^2-y^2)}{(x^2+y^2)^2}, \tag{2.15}$$

where F_x is the force in the slip direction and F_y is the force perpendicular to the slip plane. By first assuming the Burgers vector of two screw dislocations in the same direction as shown in Fig. 2.17b, the forces acting on II due to the presence of I at the origin is also presented

$$F_x = \frac{\mu b^2}{2\pi} \frac{x}{(x^2+y^2)} \quad \text{and} \quad F_y = \frac{\mu b^2}{2\pi} \frac{y}{(x^2+y^2)}. \tag{2.16}$$

It is worth mentioning that a free surface exerts an attractive force on a dislocation, because an exit from the crystal at the free surface would reduce its strain energy; conversely, a rigid surface layer would repel the dislocation. A report by Koehler (1941) has shown that this attraction force, called image force, corresponds to the force acting on an infinite body between the dislocation and its opposite sign image on the other side of the free surface. If d denotes the distance from the dislocation to this free boundary, then the image force is inversely proportional to d as follows:

$$F = \frac{\mu b^2}{4\pi(1-\nu)} \frac{1}{d}. \tag{2.17}$$

2.4 Thermodynamic Dislocation Theory (TDT) for uniform plastic deformations

The thermodynamic dislocation theory is based on two unconventional hypotheses. The first of these is that a system of dislocations, driven by external forces and irreversibly exchanging heat with its environment, must be characterized by an effective temperature that differs from the ordinary thermal temperature. Both of these temperatures are thermodynamically well-defined variables whose equations of motion determine the irreversible behaviors of these systems. The second principal hypothesis is that thermally activated depinning of entangled pairs of dislocations is the overwhelmingly dominant cause of plastic deformation. These two ideas have led to successfully predictive theories of strain hardening as in (Langer et al., 2010) or (Langer, 2015), steady-state over exceedingly wide ranges of strain rates (Langer et al., 2010), adiabatic shear banding (Langer, 2016), (Langer, 2017a), yielding transitions and grain-size (Hall-Petch) effects (Langer, 2017c).

2.4.1 Effective temperature

The TDT for uniform plastic deformations starts with a statement that the internal degrees of freedom of plastically deforming polycrystalline solid can be separated into two distinct subsystems. The first, configurational subsystem consists of coordinates that determine the mechanically stable positions of all constituent atoms, including positions of the dislocations. The second, kinetic vibrational subsystem consists of fast kinetic-vibrational coordinates that describe small fluctuations of atoms about their stable positions. The degree of freedom of two subsystems are distinguished by the time scales on which they move, i.e. the atomic rearrangements that take the configurational subsystem from one inherent structure to another one are relatively slow in comparison with the motions occur on microscopic time scales (the order of 10^{-10} s or less) inside kinetic-vibrational subsystem.

These two subsystems are a weakly interacting pair of the deforming system as a whole. One can think about two separate entities, with different temperatures and subject to various external forces, associated with each other by a poor heat conductor. The exchange energy is done between these subsystems when groups of atoms endure irreversible displacements.

For polycrystalline case, it is useful to think of a slab of material lying in a plane of applied shear stress. The dislocations oriented perpendicular to this plane is driven by the stress to move through a ”forest” of dislocations lying primarily in the plane, thus producing shear flow. Denote the energy of configurational subsystem by $U_C(S_C, \rho)$ where ρ is the total length of dislocation lines per unit volume; and $S_C(U_C, \rho)$ is the entropy calculated by adding the number of atomic configuration, taking the number of arrangements of dislocations into account, at fixed values of U_C and ρ.

The dislocations are driven by external forces to undergo chaotic motion which means they explore statistically significant parts of their configuration spaces. According to Gibbs, the entropy S_C of this configurational subsystem must be at its state of maximum probability under a specific value of the energy U_C. This is done by the balance between the input power and the rate at which energy is dissipated to the kinematic-vibrational subsystem, which serves here as the thermal reservoir. Thus the system finds a minimum of free energy which is the most probable state of the system

$$F_C = U_C - \chi S_C, \tag{2.18}$$

and the effective temperature

$$\chi = \frac{\partial U_C}{\partial S_C}, \tag{2.19}$$

the term "effective temperature", denoted here by χ to distinguish it from the ambient temperature T. Notice that, χ is an extremely large temperature, vastly greater than T because the dislocation energies are large.

2.4.2 Depinning model

The dislocations are tied by being pinned to each other. The key assumption in this model is that these pinning interactions can be broken infrequently by ordinary thermal fluctuations. When a pin is broken, the unpinned segment of a dislocation line moves spontaneously to a nearby pinning site. Moreover, the pinning times are generally much longer than the times taken by dislocations to move from one pinning site to another, the thermally activated depinning mechanism starts with Orowan's relation (described in Section 2.2) between the plastic strain rate $\dot{\epsilon}^{pl}$, the dislocation density ρ, and the average dislocation velocity v:

$$\dot{\epsilon}^{pl} = \rho\, b\, v, \tag{2.20}$$

where b is the magnitude of the Burgers vector. This relation is only geometric relation with a multiplication of following factors: shear value b/L of each dislocation as it moves across a system of linear size L, there are ρL^2 dislocations doing it at the same time, then the rate at which these occurrences are happening is v/L.

Next step is to compute the velocity v. To do this, assume that each dislocation becomes pinned and unpinned many times, and retain its identity throughout a motion across the pinning sites. If a depinned dislocation segment spends a characteristic time t_P to moves a distance of about $l \equiv 1/\sqrt{\rho}$ between pinning sites, then $v \sim l/t_P$, where thermally activated depinning rate given by

$$\frac{1}{t_P} = \frac{1}{t_0} e^{-U_P(\sigma)/k_B T}. \tag{2.21}$$

Here t_0 is a microscopic time of the order of 10^{-12} s, and $U_P(\sigma)$ is the activation barrier.

According to Langer et al. (2010), $U_P(\sigma)$ is a decrease function of σ in which the dislocation is trapped in a pinning energy $k_B T_P$ at zero stress:

$$U_P(\sigma) = k_B\, T_P\, e^{-\sigma/\sigma_T(\rho)} \tag{2.22}$$

with $\sigma_T = s\mu b\sqrt{\rho}$ being Taylor stress. The dimensionless number s is the ratio of a depinning length to the length of the Burgers vector, thus, s should be approximately independent of temperature and strain rate. When a stress σ is applied, the barrier resisting escape from the trap is lowered in the direction of σ and raised in the opposite direction. Note also that σ denotes only the magnitude of stress in this formula because this part of the analysis determines only the scalar time scale t_P. Directional information will appear in the other parts of the stress-strain relations when stresses and strains become tensors.

The resulting formula for strain rate $\dot{\epsilon}^{pl}$ becomes

$$\dot{\epsilon}^{pl} = \frac{b}{t_0}\sqrt{\rho}\,\exp\left[-\frac{T_P}{T}e^{-\sigma/\sigma_T}\right]. \tag{2.23}$$

Now, one can find the relation between true stress and Taylor stress from Eq. (2.23):

$$\sigma = \sigma_T(\rho)\,\nu(\rho, \dot{\epsilon}^{pl}, T), \tag{2.24}$$

where, (see Langer (2017b))

$$\nu(\rho, \dot{\epsilon}^{pl}, T) = \ln\left(\frac{T_P}{T}\right) - \ln\left[\ln\left(\frac{b\sqrt{\rho}}{\dot{\epsilon}^{pl}t_0}\right)\right]. \tag{2.25}$$

It is interesting to mention here that the pinning energy is large, of the order of electron volts so that the pinning temperature T_P is much larger than the ordinary temperature T. As a result, the plastic strain rate is an extremely rapidly varying function of σ and T. This strongly nonlinear behavior is the key to understand yielding transitions and shear banding as well as many other important features of polycrystalline plasticity. For example, the extremely slow variation of the steady-state stress as a function of strain rate discussed in Langer et al. (2010) is the converse of the extremely rapid variation of q as a function of σ in Eq.(2.25). In the next following chapters, the readers will see that this temperature sensitivity of the strain rate is the key to understanding important aspects of the thermomechanical behavior.

2.4.3 Non-equilibrium equations of motion

Let us start to introduce these equations of motion by considering a simple shear experimental model on a slab of material mentioned in the previous sub-section with area A, and thickness L. The total energy of this system can be written as a sum of configurational and kinematic-vibrational parts:

$$U_{total} = U_C(S_C, \rho) + U_R(S_R). \tag{2.26}$$

Here, $U_C(S_C, \rho)$ contains not only dislocation energy but also all other energies associated with all other state variables. $S_C(U_C, \rho)$ is the total entropy of the configurational subsystem, calculated by counting the number of configurations at fixed values of U_C and ρ. Also, ρ is the total length of dislocation lines per unit area. $U_R(S_R)$ is the kinetic-vibrational energy of this system, whose entropy is S_R. This subsystem works as a thermal bath, and its temperature is so-called ordinary thermal temperature (or kinetic-vibrational temperature) which is also proportional to the ambient temperature

$$k_B\,T \equiv \theta = \frac{\partial U_R}{\partial S_R}. \tag{2.27}$$

Following this assumption, one can think about splitting $U_C(S_C, \rho)$ as follows:

$$U_C(S_C, \rho) = U_0(\rho) + U_1(S_1), \tag{2.28}$$

and corresponding $S_C(U_C, \rho)$

$$S_C(U_C, \rho) = S_0(\rho) + S_1(U_1), \tag{2.29}$$

where U_0 and S_0 are, respectively, the energy and entropy of dislocations, and U_1 and S_1 are the energy and entropy of all the other configurational state variables.

$$U_0(\rho) = A\,\rho\, e_D, \quad e_D = L\,\gamma_D, \tag{2.30}$$

with γ_D is the dislocation energy per unit length, and according to Langer (2017b),

$$S_0(\rho) = -A\,\rho\,\ln(b^2\rho) + A\,\rho. \tag{2.31}$$

Then, the first law of thermodynamic for this system can be proposed as:

$$\begin{aligned}\dot{U}_{total} &= LA\,\sigma\,\dot{\epsilon}^{pl} = \dot{U}_C + \dot{U}_R, \\ &= \chi\,\dot{S}_C + \left(\frac{\partial U_C}{\partial \rho}\right)\dot{\rho} + \theta \dot{S}_R,\end{aligned} \tag{2.32}$$

the term $LA\,\sigma\,\dot{\epsilon}^{pl}$ is the rate at which the mechanical power transferred to the system by external driven force (the rate of elastic energy equals to zero). The first term $\chi\dot{S}_C$ on the second line is the rate of change of the configurational heat content while the second term implies the rate at which the configurational internal energy U_C is increasing by the formation of new dislocations at fixed configurational entropy S_C. This term can be derived to a ρ-dependent energy form by using Eqs. (2.28) and (2.29):

$$\frac{\partial U_C}{\partial \rho} = \frac{\partial(U_0 - \chi\,S_0)}{\partial \rho} \equiv \frac{\partial F_0}{\partial \rho}. \tag{2.33}$$

One can easily find the steady-state of dislocations $\rho_{ss}(\chi) = \frac{1}{b^2}e^{-e_D/\chi}$ by minimizing this free energy F_0 using Eqs. (2.30) and (2.31) (see Langer (2017b)). Whereas the last term of Eq. (2.32) implies the heat flux $\mathcal{Q}$, defined to be positive when heat is flowing from the configurational subsystem into kinematic-vibrational subsystem (thermal bath). Use this first law equation to evaluate $\dot{S}_C$, and write the second law in the form

$$\dot{S}_C + \dot{S}_R = \frac{1}{\chi}(LA\,\sigma\,\dot{\epsilon}^{pl} - \frac{\partial F_0}{\partial \rho}\dot{\rho}) + \left(1 - \frac{\theta}{\chi}\right)\dot{S}_R \geq 0. \tag{2.34}$$

For present purpose, assume the mechanical power is positive. The remaining negative term is

$$\frac{\partial F_0}{\partial \rho}\,\dot{\rho} \leq 0. \tag{2.35}$$

Langer and his colleagues have proposed an equation of motion for dislocation density

$$\dot{\rho} = \kappa_\rho \frac{\sigma\dot{\epsilon}^{pl}}{\gamma_D}\left[1 - \frac{\rho}{\rho_{ss}(\chi)}\right], \tag{2.36}$$

with dimensionless factor κ_ρ is the fraction of the mechanical power that is delivered to dislocations. The second term in the right-hand side of Eq. (2.36) can be seen as the rate of annihilated dislocations required by the second law.

Let us rewrite the first law equation in a suitable form for deriving the equation of motion for effective temperature χ:

$$\chi \, \dot{S}_C = AL \, \sigma \dot{\epsilon}^{pl} - \left(\frac{\partial F_0}{\partial \rho} \right) \dot{\rho} - \mathcal{Q}. \tag{2.37}$$

The Eqs. (2.28) and (2.29) are again used to decompose the left-hand side as

$$\chi \, \dot{S}_C = \chi \frac{\partial S_1}{\partial \chi} \dot{\chi} + \chi \frac{\partial S_0}{\partial \rho} \dot{\rho} \equiv AL \, c_{\text{eff}} \dot{\chi} + \chi \frac{\partial S_0}{\partial \rho} \dot{\rho}, \tag{2.38}$$

where the effective heat capacity is defined as $AL \; c_{\text{eff}} = \chi \partial S_1 / \partial \chi$. One can obtain a more simplified model by substituting Eq. (2.38) into Eq. (2.37)

$$AL \; c_{\text{eff}} \dot{\chi} = AL \; \sigma \dot{\epsilon}^{pl} - \left(\frac{\partial U_0}{\partial \rho} \right) \dot{\rho} - \mathcal{Q}. \tag{2.39}$$

A key observation is made here that ordinary thermal fluctuations are completely ineffective in driving these processes due to the fact that very large energies associated with nucleation and annihilation of dislocations. Langer (2017b) has therefore proposed an approximation of heat flux

$$\mathcal{Q} \approx AL \; \sigma \dot{\epsilon}^{pl} \frac{\chi}{\chi_0}, \tag{2.40}$$

with χ_0 being the effective temperature at steady state. The equation of motion for χ now becomes

$$c_{\text{eff}} \dot{\chi} = \sigma \dot{\epsilon}^{pl} \left[1 - \frac{\chi}{\chi_0} \right] - \gamma_D \, \dot{\rho}. \tag{2.41}$$

Furthermore, an equation of motion depicting the kinetic-vibrational temperature $\theta = k_B T$ should also be mentioned here

$$\left(\frac{c_p \rho_d}{k_B} \right) \dot{\theta} = \beta \sigma \dot{\epsilon}^{pl} - \mathcal{K}(\theta - \theta_0), \tag{2.42}$$

with c_p being the thermal heat capacity per unit mass, ρ_d the mass density. A positive quantity β is known as Taylor-Quinney factor which is less than unity; this dimensionless constant gives the percentage of input power that is converted into kinetic-vibrational heat. $\mathcal{K}$ is a thermal transport coefficient, and $\theta_0 = k_B T_0$ is the ambient temperature.

Finally, an equation of motion for the stress must be written here. This is simply the Hooke's law in a rate form:

$$\dot{\sigma} = \mu \dot{\epsilon}^{el} = \mu(\dot{\epsilon} - \dot{\epsilon}^{pl}), \tag{2.43}$$

with μ is the elastic shear modulus. This appoximation should be proper as long as μ is large and the elastic strains are small.

2.4.4 Scaling and dimensionless variables

As a preparation for the use of the equations of motion, it is convenient to transform variables involved in these equations into dimensionless ones, thus making it easier to identify the relevant dimensionless physical parameters. It is worth noting that the new general form of the original system introduced here will be slightly modified in the next sections to adapt to each specific physical circumstance. All systems of interest currently undergo a spatially uniform shear with constant rate $\dot{\varepsilon}$. Therefore, let $Q = \dot{\varepsilon} t_0$, where $t_0 = 10^{-12}$s is an arbitrarily chosen microscopic time scale used to express rates as meaningful dimensionless quantities. Then we can replace the time t with the accumulated total shear ε, so that $t_0 \partial/\partial t \to Q\partial/\partial\varepsilon$. Let $q = \dot{\epsilon}^{pl} t_0$, $\tilde{\rho} = b^2\rho$, $\tilde{\chi} = \chi/e_D$, and $\tilde{\theta} = T/T_P$. All these dimensionless quantities are functions of ε.

The plastic strain rate defined in Eq. (2.23) now becomes:

$$q = \sqrt{\tilde{\rho}} \exp\left[-\frac{1}{\tilde{\theta}} e^{-\sigma/\sigma_T(\tilde{\rho})}\right]; \quad \sigma_T(\tilde{\rho}) = s\mu\sqrt{\tilde{\rho}}. \tag{2.44}$$

Then, its inverse form, Eq. (2.24), reads:

$$\sigma = \sigma_T(\tilde{\rho}) \tilde{\nu}(\tilde{\rho}, q, \tilde{\theta}), \tag{2.45}$$

where ν becomes

$$\tilde{\nu}(\tilde{\rho}, q, \tilde{\theta}) = \ln\left(\frac{1}{\tilde{\theta}}\right) - \ln\left[\ln\left(\frac{\sqrt{\tilde{\rho}}}{q}\right)\right]. \tag{2.46}$$

The equation of motion for the dislocation density in Eq. (2.36) describes some fraction of the power delivered to the system by external driving which is converted into the energy of dislocations, and that energy is dissipated according to a detailed-balance analysis involving the effective temperature $\tilde{\chi}$. They can be rewritten in the new scaled variables:

$$\frac{\partial\tilde{\rho}}{\partial\varepsilon} = \kappa_\rho \frac{\sigma q}{\tilde{\gamma}_D Q}\left[1 - \frac{\tilde{\rho}}{\tilde{\rho}_{ss}(\tilde{\chi})}\right], \tag{2.47}$$

where $\tilde{\rho}_{ss}(\tilde{\chi}) = e^{-1/\tilde{\chi}}$ is the steady-state value of $\tilde{\rho}$ at given $\tilde{\chi}$, and $\tilde{\gamma}_D = \gamma_D/b^2 = e_D/b^2L$. It is interesting to reinterpret the conversion factor κ_ρ by using an important discovery from Kocks and Mecking (2003). Those investigators found that the onset slope of strain hardening, $\Theta_0 = (1/\mu)(\partial\sigma/\partial\varepsilon)_{onset}$, often (but not always) remains a material-specific constant over a wide ranges of strain rates and temperatures. To understand this behavior, we use the well-known fact that the onset of strain hardening is a transient approach to steady-state flow, in other words, hardening begins when the deformation switches from elastic to plastic, that is when $q \approx Q$ and $\tilde{\rho} \ll \tilde{\rho}_{ss}$ so that Eq. (2.47) becomes

$$\frac{\partial\tilde{\rho}}{\partial\varepsilon} \approxeq \kappa_\rho \frac{r\mu}{\tilde{\gamma}_D} \nu_Q(\tilde{\rho}, Q, \tilde{\theta})\sqrt{\tilde{\rho}}. \tag{2.48}$$

Assume that ν_Q is a slowly varied function with respect to its arguments $\tilde{\rho}$. Then the hardening rate at this onset state is:

$$\Theta_0 = \frac{1}{\mu}\frac{\partial\sigma}{\partial\varepsilon} = \frac{\nu_Q}{\mu}\frac{\partial\sigma_T}{\partial\tilde{\rho}}\frac{\partial\tilde{\rho}}{\partial\varepsilon} = \kappa_\rho \frac{\mu r^2}{\tilde{\gamma}_D}\nu_Q^2. \tag{2.49}$$

With this one can obtain κ_ρ as follows

$$\kappa_\rho = \frac{2\Theta_0\tilde{\gamma}_D}{\mu s^2 \nu_Q^2} = \frac{\tilde{\gamma}_D}{\mu s \nu_Q^2}\kappa_1. \tag{2.50}$$

Finally, Eq. (2.47) can conveniently be transformed to

$$\frac{\partial \tilde{\rho}}{\partial \varepsilon} = \kappa_1 \frac{\sigma q}{\mu s \nu_Q^2 Q} \left[1 - \frac{\tilde{\rho}}{\tilde{\rho}_{ss}(\tilde{\chi})} \right]. \tag{2.51}$$

The equation for the scaled effective temperature $\tilde{\chi}$ is a statement of the first law of thermodynamics for configurational subsystem shown in Eq. (2.41) which can be rewritten:

$$c_{\text{eff}} \frac{\partial \tilde{\chi}}{\partial \varepsilon} = \frac{\sigma q}{Q} \left(1 - \frac{\tilde{\chi}}{\tilde{\chi}_0} \right) - \tilde{\gamma}_D \frac{\partial \tilde{\rho}}{\partial \varepsilon}, \tag{2.52}$$

with the same analysis that led from Eq. (2.47) to Eq. (2.51), Eq. (2.52) becomes

$$\frac{\partial \tilde{\chi}}{\partial \varepsilon} = \kappa_2 \frac{\sigma q}{s \mu Q} \left[1 - \frac{\tilde{\chi}}{\tilde{\chi}_0} - \frac{\tilde{\gamma}_D \, \kappa_1}{s \, \mu \, \nu_Q^2} \left(1 - \frac{\tilde{\rho}}{\tilde{\rho}_0(\tilde{\chi})} \right) \right], \tag{2.53}$$

where the dimensionless factor $\kappa_2 = s \, \mu / c_{\text{eff}}$. Unlike κ_1, whose value is determined directly from experiment via Eq. (2.51), κ_2 must be detected on a case by case basis by fitting the data. The last term inside the square bracket is the rate at which configurational energy is stored in the form of dislocations. Although there are circumstances this term is important as demonstrated in Langer (2015) where it is implemented to reduce the slope of the stress-strain curves after initial rise at different small grain sizes, this term still can be assumed to be negligible for the sake of simplicity in most of the cases.

The equation of motion for the scaled, ordinary temperature, Eq. (2.42), is:

$$\frac{\partial \tilde{\theta}}{\partial \varepsilon} = K(\tilde{\theta}) \frac{\sigma q}{Q} - \frac{K_2}{Q} (\tilde{\theta} - \tilde{\theta}_0), \tag{2.54}$$

where $K(\tilde{\theta}) = \beta / (T_P \, c_p \, \rho_d)$ is a thermal conversion factor, while K_2 is a thermal transport coefficient that controls how rapidly the system relaxes toward the ambient temperature T_0, that is $\tilde{\theta} \to \tilde{\theta}_0 = T_0 / T_P$. Finally, the stress equation, Eq. (2.43), becomes

$$\frac{\partial \sigma}{\partial \varepsilon} = \mu \left[1 - \frac{q}{Q} \right]. \tag{2.55}$$

2.5 Thermodynamic Dislocation Theory (TDT) for non-uniform plastic deformations

In the previous Section of this Chapter, the TDT was discussed for uniform plastic deformations of crystals whose dislocations are neutral in the sense that their resultant Burgers vector vanishes. Cottrell (1964) called these dislocations redundant dislocations. For nonuniform plastic deformations such as the torsion of a rod, the bending of a beam or the deformation of two-phase alloys or polycrystals, another type of dislocations occurs in addition to the redundant ones in order to adapt to the plastic deformation gradient and to ensure the compatibility of the total deformations (Ashby (1970), Bilby (1955), Nye (1953)). These dislocations are called excess dislocations which appears natural from the point of view of statistical mechanics of dislocations ((Berdichevsky, 2006b; Limkumnerd & Van der Giessen, 2008; Poh et al., 2013; Zaiser, 2015)). Thanks to the development of microstructural crystallographic characterization in recent years, the density of excess dislocation can be measured indirectly by transmission electron microscopy (TEM) or electron backscattering technique (EBSD) (Kysar et al., 2010). The Continuum Dislocation Theory (CDT), which includes the density of excess dislocations as developed by Berdichevsky and Sedov (1967); Gurtin (2002); Le and Günther (2014); Le and Stumpf (1994, 1996), can describe the evolution of the dislocation network and predict the formation of a microstructure. However, the main disadvantage of this phenomenological approach is the absence of redundant dislocations and configuration temperature.

This section will discuss a TDT for non-uniform plastic deformation first proposed by Le (2018), who includes two missing quantities, the configurational temperature and the density of redundant dislocations, as state variables in its constitutive equations.

2.5.1 Kinematics

The theory starts with an assumption that there are only two kinematical quantities, the displacement field $\boldsymbol{u}(\boldsymbol{x},t)$ and plastic distortion field $\boldsymbol{\beta}(\boldsymbol{x},t)$ which characterize the observable deformation of single crystals ($\boldsymbol{x}$ is the position vector of a generic material point in cartesian coordinate). For a crystal deforming in one active slip system, the plastic distortion has the form

$$\boldsymbol{\beta}(\boldsymbol{x},t) = \beta(\boldsymbol{x},t)\boldsymbol{s}\otimes\boldsymbol{m}, \tag{2.56}$$

with plastic slip $\beta(\boldsymbol{x},t)$ being a continuously differentiable function, where the pair of the constant and mutually orthogonal unit vector $\boldsymbol{s}$ and $\boldsymbol{m}$ denote the slip direction and the normal to the slip planes. It can be easily seen that, in general, $tr\boldsymbol{\beta} = \beta_{ii} = 0$, so that the continuous plastic distortion does not cause any volumetric change. If the crystal possesses n slip systems, the plastic distortion has the following form

$$\boldsymbol{\beta}(\boldsymbol{x},t) = \sum_{i=1}^{n}\beta(\boldsymbol{x},t)\boldsymbol{s}^i\otimes\boldsymbol{m}^i. \tag{2.57}$$

The total compatible strain tensor can be obtained from the displacement field

$$\boldsymbol{\varepsilon} = \frac{1}{2}(\boldsymbol{u}\nabla + \nabla\boldsymbol{u}). \tag{2.58}$$

The incompatible strain tensor is the symmetric part of the plastic distortion field

$$\boldsymbol{\varepsilon}^p = \frac{1}{2}(\boldsymbol{\beta} + \boldsymbol{\beta}^T). \tag{2.59}$$

We limit our theory to the small strain case. Thus the additive decomposition of total strain into elastic and plastic parts will be assumed

$$\boldsymbol{\varepsilon}^e = \boldsymbol{\varepsilon} - \boldsymbol{\varepsilon}^p. \tag{2.60}$$

These three strain fields and their relations are illustrated schematically in Fig. 2.18. In this figure, the distortion of shape and lattice is always the same for an elastic deformation. This means that the internal state of the crystal is changed during an elastic deformation which

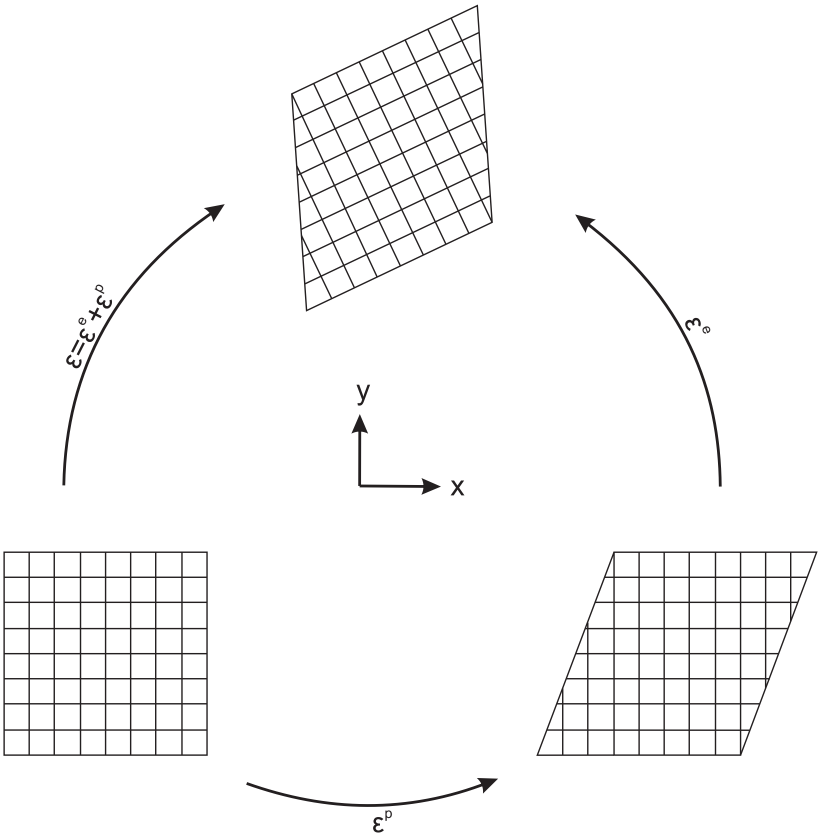

Figure 2.18: Decomposition of total strain.

results in elastic strain. In contrary, the change of shape due to the plastic deformation does not change the internal state of the crystal unless dislocations appear inside it (the lattice orientation remains the same).

Consider any infinitesimal area da through which a total number of N dislocation lines intersect. Among them there are N^+ dislocations with Burgers vector $b\boldsymbol{s}$ and N^- dislocations with Burgers vector $-b\boldsymbol{s}$, where b is the length of the Burgers vector. Then the number of excess dislocations is defined by $N^g = |N^+ - N^-|$, while the number of redundant dislocations is defined by $N^r = N - N^g$. Accordingly, the scalar density of excess and redundant dislocations is

$$\rho^g = \frac{N^g}{da}, \; \rho^r = \frac{N^r}{da}. \tag{2.61}$$

Nye (1953), Bilby (1955), and Kröner (1955) introduced the *dislocation density tensor*, $\boldsymbol{\alpha} = -\boldsymbol{\beta} \times \nabla$, which takes all excess dislocations into account. This leads to the resultant Burgers vector of all excess dislocations, whose dislocation lines cross the area da

$$d\boldsymbol{B} = \boldsymbol{\alpha} \cdot \boldsymbol{n} \, da, \tag{2.62}$$

with $\boldsymbol{n}$ being the unit vector normal to da. Therefore, the density of excess dislocation for a crystal with one active slip system can be related to the plastic distortion

$$\rho^g = \frac{|d\boldsymbol{B}|}{b \, da} = \frac{1}{b} \left| \boldsymbol{n} \cdot (\nabla \times \boldsymbol{\beta}) \right|. \tag{2.63}$$

In contrast to the excess dislocations, the redundant ones cannot be expressed in term of plastic distortion; however, they may significantly affect the creation of excess dislocations and work hardening of crystals. As a rule, this sort of dislocations exists only in the form of dislocation dipoles at a low temperature to render the low energy of the crystal. Also, the density of dislocation dipoles depends only on temperature, in other words, the dislocation dipoles can be nucleated by the mutual trapping of dislocations of different signs in a random way, or eventually, by thermal fluctuations due to their low energy. The total dislocation density is thus,

$$\rho = \rho^g + \rho^r. \tag{2.64}$$

2.5.2 Energy of dislocation network

Let us start with the free energy density to construct models of crystals with continuously distributed dislocations using the non-equilibrium thermodynamics of the externally driven system. This energy density must depend only on state variables. A variable that characterizes the body in question is called a state variable if it depends exclusively on the current state of the body. According to Kröner (1992) and Langer (2016), the elastic strain $\boldsymbol{\varepsilon}^e$, the dislocation densities ρ^r and ρ^g, the kinetic-vibrational temperature T and the configurational temperature χ are the state variables of this TDT. The reason why plastic deformation $\boldsymbol{\beta}$ or plastic strain tensor $\boldsymbol{\varepsilon}^p$ cannot be regarded as a state variable is that they are dependent on the cut surfaces and thus on the entire history of dislocation formation (for example, the climb of glide dislocations are created quite differently). In contrary, the dislocation densities ρ^g and ρ^r are state variable because they depend only on the Burgers vector and the positions of the dislocation lines that characterize the current state of the dislocations and not on how they are generated. In this theory, the author limits himself to the isothermal processes, so that the kinetic-vibrational temperature T is assumed to be constant and can be dropped into the list of arguments of free energy density. Our main assumption for the free energy is

$$\psi = \frac{1}{2}\lambda(tr\boldsymbol{\varepsilon}^e)^2 + \mu\boldsymbol{\varepsilon}^e : \boldsymbol{\varepsilon}^e + \gamma_D\rho^r + \psi_m(\rho^g) - \chi(-\rho\ln(a^2\rho) + \rho)/L. \tag{2.65}$$

The first two terms in Eq. (2.65) represent the free energy of the crystal due to the elastic strains, where λ and μ are the Lame's constants. The third term is the self-energy of redundant dislocations, where γ_D is the energy of the dislocation dipole per unit length. The fourth term represents the energy of excess dislocations. According to Berdichevsky (2006b) and Le (2018) this type of free energy should have logarithmic form to ensure that the energy for small dislocation density ρ^g increases linearly and tends toward infinity when ρ^g approaches the saturated dislocation density and thus provides an energetic barrier against supersaturation. A more detailed discussion will be given in the next Subsections. The last term was introduced by Langer (2016), where $S_C = -\rho\ln(a^2\rho) + \rho$ is the configurational entropy of dislocations, where a is the admissible nearest distance between dislocations, and L is the depth of the sample.

With this free energy density at hand, the energy functional of the crystal can be written down. Let V be the region of an undeformed single crystal. The boundary of this region, ∂V, is assumed to be the union of two non-intersecting areas ∂V_k and ∂V_s. Let the displacement vector $\boldsymbol{u}(\boldsymbol{x}, t)$ be a given smooth function of coordinates, and, consequently, the plastic slips $\beta(\boldsymbol{x}, t)$ vanish

$$\boldsymbol{u}(\boldsymbol{x}, t) = \boldsymbol{u}^*(\boldsymbol{x}, t),\ \beta(\boldsymbol{x}, t) = 0 \quad \text{for} \quad \boldsymbol{x} \in \partial V_k. \tag{2.66}$$

The remaining boundary part ∂V_s is assumed to be traction free. If no body-forces act on the crystal, then its energy functional is

$$I\left[\boldsymbol{u}(\boldsymbol{x},t),\beta(\boldsymbol{x},t),\rho^r(\boldsymbol{x},t),\chi(\boldsymbol{x},t)\right]=\int_V \psi(\boldsymbol{\varepsilon}^e,\rho^r,\rho^g,\chi)dV, \tag{2.67}$$

with dV stands for the volume element.

2.5.3 System of equations

When the external driving forces increase, the resolved shear stress also increases. When it reaches Taylor stress, the dislocation dipoles are dissolved and the dislocations that become free begin to move until they are pinned again by dislocations with opposite signs. This dislocation movement leads to a dissipation of energy, which in turn leads to resistance to the dislocation movement. Increasing the dislocation density and increasing the configuration temperature also leads to energy dissipation. In Langer et al. (2010), internal viscosity may be essential only at low strain rates and low dislocation densities, since in this case the time required for a freely moving dislocation to overcome the distance between the pinning sites may be more significant than the pinning times. At higher strain rates the internal viscosity can be neglected. Since we are considering this case, the dissipation potential can be proposed as follows

$$D(\dot{\beta},\dot{\rho},\dot{\chi})=\tau_Y\dot{\beta}+\frac{1}{2}d_\rho\dot{\rho}^2+\frac{1}{2}d_\chi\dot{\chi}^2, \tag{2.68}$$

with τ_Y is the flow stress during plastic yielding, d_ρ and d_χ are unknown functions that will be determined later. Then, the first term of Eq. (2.68) is assumed to be a homogeneous function of first order with respect to the plastic slip rate. The other two terms represent the dissipation caused by the formation of dislocations and the increase of the configuration temperature. As mentioned in Sec. 2.4, the rate of flow stress is obtained as follows:

$$\dot{\tau}_Y=\mu\frac{Q}{t_0}\left[1-\frac{q(\tau_Y,\rho)}{Q}\right], \tag{2.69}$$

where Q/t_0 is rate of shear strain, and $t_0=10^{-12}$ s is the characteristic microscopic time scale. According to Langer et al. (2010); Le (2018), the plastic slip rate is

$$\dot{\beta}=\frac{q(\tau_Y,\rho)}{t_0}=\frac{1}{t_0}b\sqrt{\rho}\,exp\left[-\frac{1}{\theta}e^{-\tau_Y/\tau_T}\right], \tag{2.70}$$

with the dimensionless temperature being $\theta=T/T_P$, T_P the pinning energy barrier, and τ_T the Taylor stress. Then, the governing equations can be derived from the following variational principle (see Sedov (1968)): Among all admissible fields $\boldsymbol{u}(\boldsymbol{x},t),\beta(\boldsymbol{x},t),\rho^r(\boldsymbol{x},t)$ and $\chi(\boldsymbol{x},t)$ satisfying the constraints (2.66), the true displacement field $\hat{\boldsymbol{u}}(\boldsymbol{x},t)$, the true plastic slip $\hat{\beta}(\boldsymbol{x},t)$, the true redundant dislocation density $\hat{\rho}^r(\boldsymbol{x},t)$, and the true configurational temperature $\hat{\chi}(\boldsymbol{x},t)$ obey the variational equation

$$\delta I+\int_V\left(\frac{\partial D}{\partial\dot{\beta}}\delta\beta+\frac{\partial D}{\partial\dot{\rho}}\delta\rho+\frac{\partial D}{\partial\dot{\chi}}\delta\chi\right)dV=0. \tag{2.71}$$

For the sake of simplicity, let us first consider a plane strain deformation of a single crystal occupying an area A and having only one active slip system. Then, the density of excess dislocations is simplified to:

$$\rho^g = \frac{1}{b} \left| \partial_s \beta \right| ,$$

where $\partial_s = s_i \partial_i$ denotes the derivative in the direction $\boldsymbol{s}$. The quasi-static equations of equilibrium of macro-forces can be obtained by varying the energy functional with respect to $\boldsymbol{u}$

$$\boldsymbol{\sigma} \cdot \nabla = 0, \quad \boldsymbol{\sigma} = \frac{\partial \psi}{\partial \boldsymbol{\varepsilon}^e} = \lambda tr(\boldsymbol{\varepsilon}^e) \boldsymbol{I} + 2\mu \boldsymbol{\varepsilon}^e, \tag{2.72}$$

subjected to the boundary conditions (2.66) and

$$\boldsymbol{\sigma} \cdot \boldsymbol{n} = 0 \quad \text{on } \partial A_s .$$

The similar calculus of variations for other quantities β, ρ^r and χ for Eq. (2.71) leads to:

$$\tau + \frac{1}{b}(\zeta \ \text{sign} \beta_{,s})_{,s} - \tau_Y + \frac{1}{b}(d_\rho \, \dot{\rho} \ \text{sign} \beta_{,s})_{,s} = 0, \tag{2.73a}$$

$$(e_D + \chi \ln(a^2 \rho))/L + d_\rho \, \dot{\rho} = 0, \tag{2.73b}$$

$$(\rho \ln(a^2 \rho) - \rho)/L + d_\chi \, \dot{\chi} = 0. \tag{2.73c}$$

Here, $e_D = L\gamma_D$, $\tau = \sigma_{ij} s_i m_j$ is the resolved shear stress, while $\zeta = \partial \psi / \partial \rho^g$, and the two terms $\frac{1}{b}(\zeta \ \text{sign}\beta_{,s})_{,s} + \frac{1}{b}(d_\rho \, \dot{\rho} \ \text{sign}\beta_{,s})_{,s}$ depict the back stress τ_B due to the interaction of excess dislocations. This equation is the balance of micro-forces acting on excess dislocations subjected to the Dirichlet boundary condition (2.66) on ∂A_k and

$$\zeta + d_\rho \, \rho = \dot{0} \quad \text{on } \partial A_s .$$

It is reasonable to expect these equations of motion to be reduced to the original equations of Langer et al. (2010) if the plastic deformations become homogeneous, because in that case the excess dislocations density vanishes. The two functions d_χ and d_ρ should be chosen as in Le (2018) to achieve this reduction:

$$d_\rho = \frac{-e_D - \chi \ln(a^2 \rho)}{L \kappa_1 \frac{\tau_Y}{a^2 \nu(T,\rho,Q)^2} \frac{q(\tau_Y,\rho)}{t_0} \left[1 - \frac{\rho}{\rho_{ss}(\chi)} \right]}, \tag{2.74}$$

$$d_\chi = \frac{\rho - \rho \ln(a^2 \rho)}{L \kappa_2 \tau_Y \frac{q(\tau_Y,\rho)}{t_0} \left[1 - \frac{\chi}{\chi_0(q)} \right]}, \tag{2.75}$$

with $\nu(T, \rho, Q)$, χ_0, and ρ_{ss} defined in Sec. 2.4.

We also expect that this TDT can be reduced to CDT if redundant dislocations and configurational temperature are neglected. This is the case with extremely slow quasistatic loading and low temperature, as then the nucleation of dislocation dipoles and the thermally assisted depinning mechanism are significantly reduced. In this case, the energy functional should have the form (Berdichevsky, 2006a, 2006b):

$$I \left[\boldsymbol{u}(\boldsymbol{x}, t), \beta(\boldsymbol{x}, t) \right] = \int_V (\frac{1}{2} \lambda (tr \boldsymbol{\varepsilon}^e)^2 + \mu \boldsymbol{\varepsilon}^e : \boldsymbol{\varepsilon}^e + \psi_m(\rho^g)) dV. \tag{2.76}$$

With regard to the dissipation potential, several models can be considered. The simplest assumption is that the resistance to dislocation motion during the plastic deformation can be neglected, which means that the dissipation is zero. In this case, we must minimize the energy functional under the constraints (2.66). If the dissipation potential D is a first order homogeneous function with respect to $\dot{\boldsymbol{\beta}}(\boldsymbol{x}, t)$, then the energy minimization should be replaced by the following variation equation:

$$\delta I + \int_V \left(\frac{\partial D}{\partial \dot{\beta}} \delta \beta \right) dV = 0. \tag{2.77}$$

In recent years, this CDT has been successfully implemented to predict the formation of micro-structure (Kochmann and Le (2009a); Koster et al. (2015); Le and Nguyen (2012)) and the size effects (Kaluza and Le (2011); Kochmann and Le (2009b); Le and Nguyen (2013)).

3 Thermal softening, adiabatic shear banding, and torsion of bars

This chapter examines the use of thermodynamic dislocation theory (TDT) to model the uniform deformation of materials subjected to thermomechanical processing. The author presents an analysis of high-temperature compression tests performed experimentally for aluminum (Shi et al., 1997a) and steel (Abbod et al., 2007). With the physically based parameters used here, which seem to be theoretically independent of strain rate and temperature, experimental stress-strain curves can be adapted for three different strain rates and three different temperatures for each of these two materials. The theoretical curves include zero strain transitions in accordance with the experiment. It is found that thermal softening effects are remarkable even at the lowest temperatures and strain rates.

In addition, the effect caused by excess dislocations is not so significant and can be neglected when considering samples the size of which is in the macro length scale. Thus, an extension of the TDT proposed by Langer (2017b); Langer et al. (2010), aimed at nonuniform plastic deformation, is possible. The author would like to introduce two applications of TDT to nonuniform plastic deformation in materials science and engineering, such as adiabatic shear band in steel from Marchand and Duffy (1988) and torsion of bars in copper from Horstemeyer et al. (2002). For the first test of Marchand and Duffy (1988) the challenge is to use a small set of physical parameters that are expected to be approximately independent of strain rate and temperature to explain experimental stress-strain curves at six different temperatures and four different strain rates. A simple model of a weak notch-like perturbation is constructed in such a way that, with sufficient loading, shear band instabilities are triggered that are quantitatively comparable to those in the experiments. For the latter test of Horstemeyer et al. (2002) the challenge is to simulate the torque-twist curve with the hardening behavior and compare it with the experimental curves. To enable this comparison, we have to identify a list of material parameters for single crystal copper under torsion from the experimental data of Horstemeyer et al. (2002).

3.1 Thermal softening effects of high-temperature deformation in aluminum and steel

3.1.1 Equations of Motion

Strictly speaking, the thermodynamic dislocation theory should be written in three-dimensional tensorial notation in order to use it in analyses of plane-strain compression tests. Moreover, Fig.1 in Shi et al. (1997b) shows a diagram of a plane-strain sample like those used in Shi et al. (1997a). Here, a thin rectangular block under uniaxial compression is shown bulging at its sides and thinning at its center in addition to undergoing pure shear. These deformations if actually as large as shown would slightly affect the interpretation of the reported stress-strain data. However, a detailed analysis of those deformations would be well beyond the scope and needs of this project.

Suppose, for simplicity, that the experimental sample is a two dimensional rectangular block in the $x\,y$ plane, being compressed between two rigid plates parallel to the x axis. The compressive stress in the y direction is $\sigma_{yy} \equiv -\sigma$. If the plates are well lubricated so that the friction between the block and the plates is negligible, then $\sigma_{xx} \approx 0$. For this uniaxial geometry, the stress tensor is naturally expressed in the $x'\,y'$ frame of reference oriented at 45° to the $x\,y$ axes. In that frame, the shear stress is $\sigma_{x'y'} = \sigma_{y'x'} = -\sigma/2$. If the material is incompressible, then the total elastic plus plastic strain rate is $\dot{\epsilon}_{yy} = -\dot{\epsilon}_{xx} \equiv -\dot{\epsilon}$. In the rotated frame, the shear rate is $\dot{\epsilon}_{x'y'} = \dot{\epsilon}_{y'x'} = -\dot{\epsilon}$. As usual, it is assumed that the elastic and plastic strain rates are simply additive, e.g. $\dot{\epsilon}_{x'y'} = \dot{\epsilon}^{el}_{x'y'} + \dot{\epsilon}^{pl}_{x'y'}$. Then, by convention, $\dot{\sigma}_{x'y'} = 2\,\mu\,\dot{\epsilon}^{el}_{x'y'}$, where μ is the shear modulus and the factor 2 accounts for the distinction between “true” and “engineering” strain. Putting these pieces together, one can write $\dot{\sigma} = \alpha\,\mu\,(\dot{\epsilon} - \dot{\epsilon}^{pl})$, where $\alpha \simeq 4$ is a geometric factor, and the directional subscripts have been dropped. In this way, the one-dimensional notation have been recovered.

Now assume that this spatially uniform system is driven at a constant shear rate $\dot{\epsilon} \equiv Q/t_0$, where $t_0 \equiv 10^{-12} s$ is a characteristic microscopic time scale. The system of equations of motion for the stress σ and the scaled internal state variables $\tilde{\rho}$, $\tilde{\chi}$, and $\tilde{\theta}$, which are functions of ϵ would be taken from Eqs. (2.51), (2.53), (2.54) and (2.55) without further detail explain:

$$\frac{d\sigma}{d\epsilon} = \alpha\,\mu\,\left[1 - \frac{q}{Q}\right], \tag{3.1}$$

$$\frac{d\tilde{\rho}}{d\epsilon} = \kappa_1\,\frac{\sigma\,q}{\nu(\tilde{\theta},\tilde{\rho},Q)^2\,\mu_T\,Q}\left[1 - \frac{\tilde{\rho}}{\tilde{\rho}_{ss}(\tilde{\chi})}\right], \tag{3.2}$$

$$\frac{d\tilde{\chi}}{d\epsilon} = \kappa_2\,\frac{\sigma\,q}{\mu_T\,Q}\left(1 - \frac{\tilde{\chi}}{\tilde{\chi}_0}\right), \tag{3.3}$$

$$\frac{d\tilde{\theta}}{d\epsilon} = K(\tilde{\theta})\,\frac{\sigma\,q}{Q} - \frac{K_2}{Q}\,(\tilde{\theta} - \tilde{\theta}_0). \tag{3.4}$$

Here, the last term of Eq. (2.53) is assumed to be negligible for the sake of simplicity. In Langer (2017c), κ_2 for copper was found to decrease from 17 to 12 when the strain rate increased by a factor of 10^6. Since changes in strain rate of at most a factor of 10^2 will be considered here, it is useful to assume that κ_2 is a constant. $K(\tilde{\theta})$ will be found to be non-trivially temperature dependent for both of the materials discussed in Secs. 3.1.2 and 3.1.3. K_2 is a thermal transport coefficient that controls how rapidly the system relaxes toward the ambient temperature T_0, that is, $\tilde{\theta} \to \tilde{\theta}_0 = T_0/T_P$. This coefficient turns out to be too small to be measured for the situations reported here, but that will not always be the case. In principle, after long enough times of steady deformation, systems must reach steady-state temperatures determined by the balance between heating and cooling terms in Eq. (3.4).

3.1.2 Comparison with experiment: Aluminum

The experimental results of Shi et al. (1997a) for aluminum, along with theoretical results based on the equations of motion in Sec. 3.1.1, are shown in Figs. 3.1, 3.2, and 3.3. These figures are presented in order of increasing strain rate, $\dot{\epsilon} = 0.25\,s^{-1}$, $2.5\,s^{-1}$, and $25\,s^{-1}$.

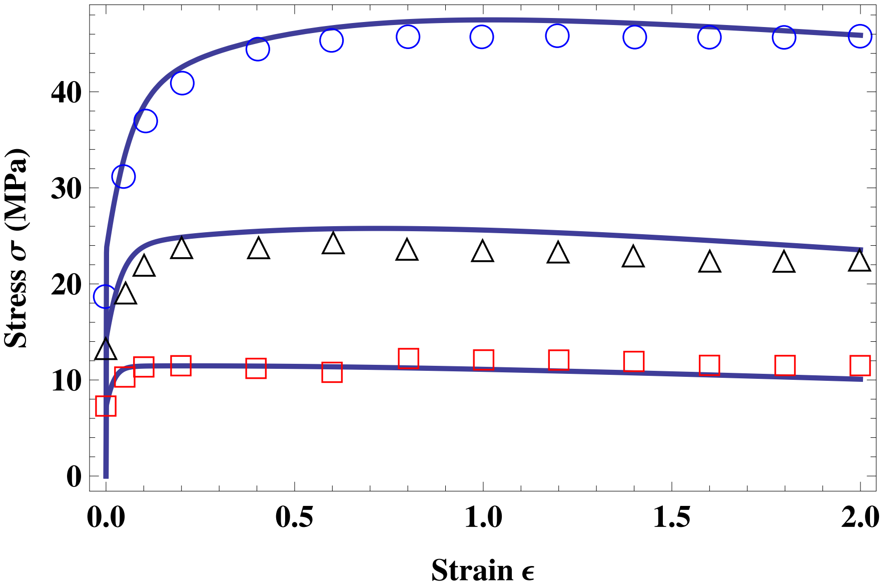

Figure 3.1: Stress-strain curves for aluminum at the small strain rate $\dot{\epsilon} = 0.25\,s^{-1}$, for temperatures $300\,C,\ 400\,C,\ 500\,C$ shown from top to bottom. The experimental points are taken from Shi et al. (1997a).

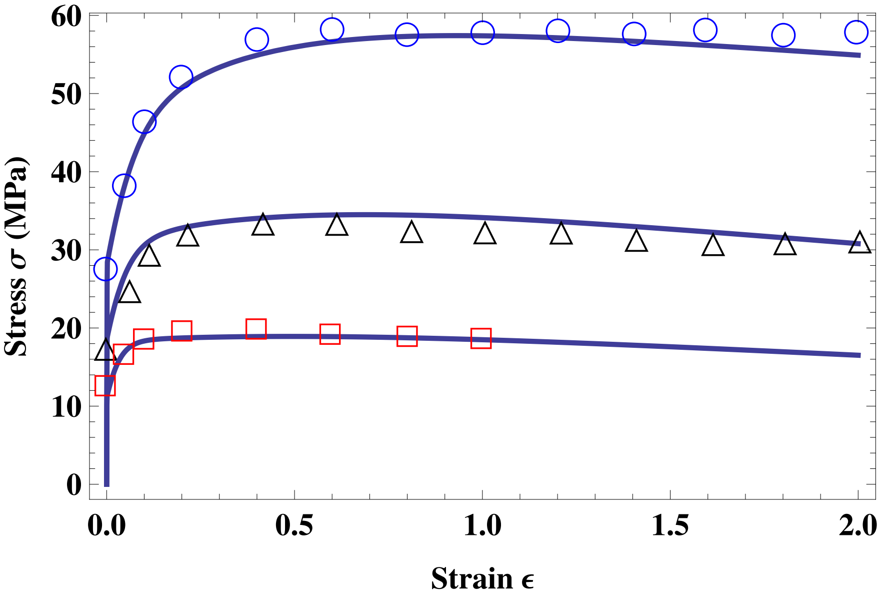

Figure 3.2: Stress-strain curves for aluminum at the strain rate $\dot{\epsilon} = 2.5\,s^{-1}$, for temperatures $300\,C,\ 400\,C,\ 500\,C$ shown from top to bottom. The experimental points are taken from Shi et al. (1997a).

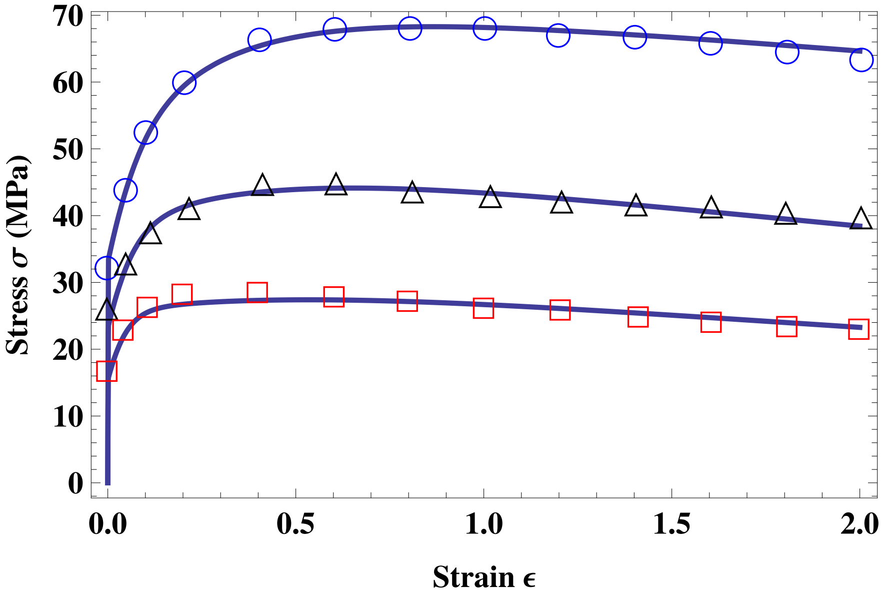

Figure 3.3: Stress-strain curves for aluminum at the highest strain rate $\dot{\epsilon} = 25\,s^{-1}$, for temperatures $300\,C,\ 400\,C,\ 500\,C$ shown from top to bottom. The experimental points are taken from Shi et al. (1997a).

Within each figure are curves for the three different temperatures $300\,C,\ 400\,C$, and $500\,C$ (blue circles, black triangles, and red squares respectively) shown from top to bottom.

In order to compute the theoretical curves in these figures, values for five system-specific parameters are needed: the activation temperature T_P, the stress ratio s, the steady-state scaled effective temperature $\tilde{\chi}_0$, and the two dimensionless conversion factors κ_1 and κ_2. We also need initial values of the scaled dislocation density $\tilde{\rho}(\epsilon = 0) \equiv \tilde{\rho}_i$ and the effective temperature $\tilde{\chi}(\epsilon = 0) \equiv \tilde{\chi}_i$, which are determined by sample preparation – presumably the same for all samples, but possibly a source of experimental uncertainty. In addition, a formula is needed for the thermal conversion factor $K(\tilde{\theta})$ in Eq. (3.4) which, for aluminum, one can take to have the linear form

$$K(\tilde{\theta}) = K_0\,\left[1 + c_1\,T_P\,(\tilde{\theta} - \tilde{\theta}_1)\right], \tag{3.5}$$

where $T_P\,\tilde{\theta}_1$ is a reference temperature, chosen here to be $573\,K$. The numbers K_0 and c_1 remain to be determined by the data. Finally, a formula for the temperature dependent shear modulus $\mu(T)$, which can be taken from Chen et al. (1998); Varshni (1970) to be

$$\mu(\tilde{\theta}) = \mu_1 - \left[\frac{D}{\exp(T_1/T_P\,\tilde{\theta}) - 1}\right], \tag{3.6}$$

where $\mu_1 = 28.8\,GPa$, $D = 3.44\,GPa$, and $T_1 = 215\,K$. (A simple linear approximation to this formula analogous to Eq. (3.5) would be completely adequate for present purposes.)

In earlier papers starting with Langer et al. (2010), the author were able to begin evaluating the parameters by observing steady-state stresses σ_{ss} at just a few strain rates Q and ambient temperatures $T_0 = T_P\,\tilde{\theta}_0$, and inverting Eq. (2.44) to find

$$\sigma_{ss} = s\,\mu\,\sqrt{\tilde{\rho}_{ss}}\;\nu(\tilde{\theta}_0, \tilde{\rho}_{ss}, Q); \quad \tilde{\rho}_{ss} = e^{-1/\tilde{\chi}_0}. \tag{3.7}$$

Knowing σ_{ss}, T_0 and Q for three stress-strain curves, we could solve this equation for T_P, s, and $\tilde{\chi}_0$, and check for consistency by looking at other steady-state situations. With that information, it was relatively easy to evaluate κ_1 and κ_2 by directly fitting the full stress-strain curves. This strategy does not work here because the thermal effects are highly nontrivial. Examination of the experimental data shown in the figures indicates that almost all of these samples are undergoing thermal softening at large strains; the stresses are decreasing and the temperatures must be increasing. Even the curves that appear to have reached some kind of steady state have not, in fact, done so at their nominal ambient temperatures.

To counter this difficulty, large-scale least-squares analyses have been resorted. (A preliminary discussion of this procedure has been presented by Le and Tran (2017).) That is, the sum of the squares of the differences between the theoretical stress-strain curves and the experimental points have been computed,

$$h(T_P, s, \chi_0, \kappa_1, \kappa_2, \tilde{\rho}_i, \tilde{\chi}_i, K_0, c_1, K_2) = \sum_{i=1}^{N} (\sigma(\varepsilon_i) - \sigma_i)^2, \tag{3.8}$$

where $(\varepsilon_i, \sigma_i), i = 1, ..., N$ correspond to the data points measured in experiment at temperatures and strain rates taken from Shi et al. (1997a), and this sum function h was minimized in the space of the unknown parameters: $T_P, s, \chi_0, \kappa_1, \kappa_2, \tilde{\rho}_i, \tilde{\chi}_i, K_0, c_1, K_2$. Options of omitting some of the data, fitting the theory to just those portions of the data have been explored that seemed most reliable. For example, the author have looked to see what happens if the yield points in this calculation is omitted on the assumption that they are most sensitive to variations in sample preparation. The results appear to be robust. They are found: $T_P = 2.40 \times 10^4\,K$, $s = 0.040$, $\chi_0 = 0.249$, $\kappa_1 = 0.97$, $\kappa_2 = 12$, $\tilde{\rho}_i = 0.0035$, $\tilde{\chi}_i = 0.224$, $K_0 = 7.0 \times 10^{-6}$, $c_1 = 0.0257$, and $K_2 = 0$. So far as one can tell, values of K_0 and c_1 are consistent with values of the Taylor-Quinney factor β of the order of unity or less. For simplicity, it is convenient to set $\alpha = 1$ in Eq. (3.1) because the slopes of the initial elastic parts of the stress-strain curves are too large to be meaningful here. Note, however, that with $\alpha \cong 4$ and $s = 0.04$, the ratio of the depinning length to the length of the Burgers vector becomes 0.16, which seems physically reasonable.

The agreement between theory and experiment seems to be well within the bounds of experimental uncertainties. Even the initial yielding transitions appear to be described accurately by this dynamical theory. There are only a few apparent discrepancies. For example, the experimental data in Fig. 3.1 for $\dot{\epsilon} = 0.25\,s^{-1}$, $T = 500\,C$ exhibit a small, abrupt increase in the stress at about $\epsilon \cong 0.8$, which may indicate some kind of instrumental problem. Also, the stresses for $T = 400\,C$ in that figure are slightly below those predicted by the theory, and there is a smaller discrepancy of the opposite sign on the curve at $\dot{\epsilon} = 2.5\,s^{-1}$, $T = 300\,C$ in Fig. 3.2. Nothing about these results leads us to believe that there are important physical ingredients missing in this theory.

It is interesting to discuss the behavior of the fractional plastic strain rate q/Q for pure aluminum at fixed strain rate $\dot{\varepsilon} = 0.25\,s^{-1}$ as function of the strain ε, shown in Fig. 3.4, where the curves are magnified near 1 to describe the strongly nonlinear behavior of the dimensionless quantity q/Q. The increase of the slope of q/Q according to the temperature rise from 300 C to 500 C can be explained as follows: At the same strain rate, the higher the normal temperature, the faster the dislocation depinning and the higher the plastic strain rate. Another important feature is that due to the additional heat generated by the movement of dislocations, in the second phase of these curves there is a slow linear increase that leads

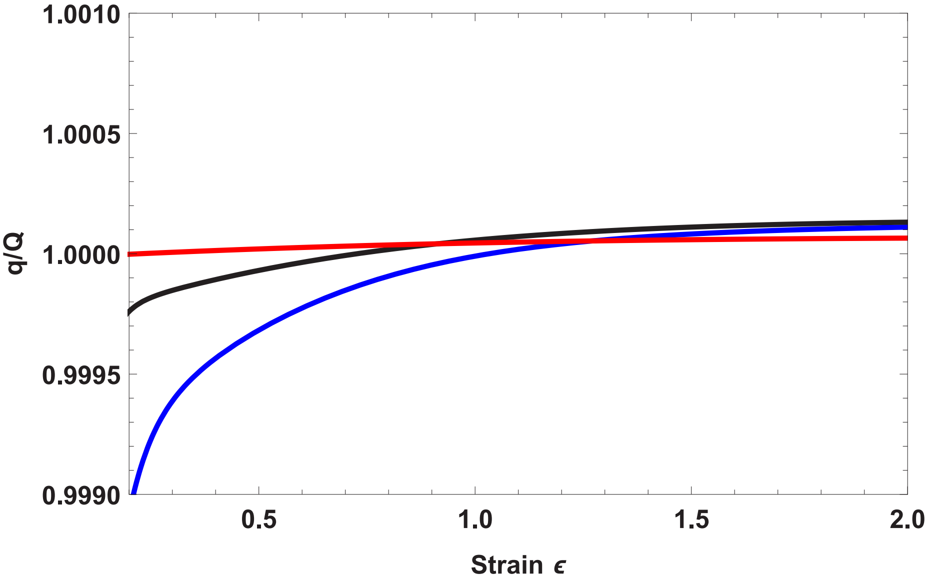

Figure 3.4: Theoretical fractional strain rate distribution for pure aluminum at the strain rate $\dot{\epsilon} = 0.25\,s^{-1}$, for temperatures $300\,C,\ 400\,C,\ 500\,C$ shown from bottom to top.

to $q > Q$ when the strain ε increases. This results in the negative tangent of the stress-strain curve represented by Eq. (3.1), which is the cause of thermal softening phenomenon.

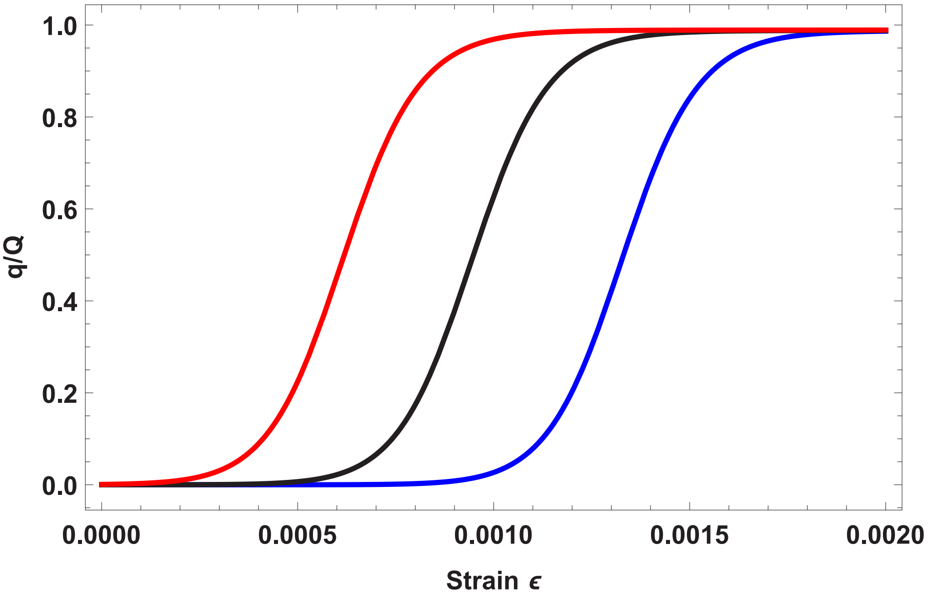

Figure 3.5: Theoretical fractional strain rate distribution across the initial yielding transition for pure aluminum at the strain rate $\dot{\epsilon} = 2.5\,s^{-1}$, for temperatures $300\,C,\ 400\,C,\ 500\,C$ shown from right to left.

Let us consider what is happening near $\varepsilon = 0$ where the three outputs under the same strain rate $\dot{\epsilon} = 2.5\,s^{-1}$ and temperatures from $300\,C$ to $500\,C$ exhibit what appear to be yielding transitions. All curves in Fig. 3.2 start with elastic sections and then bend smoothly to plastic behavior. Fig. 3.5 again confirms that the normalized dimensionless plastic strain rate q/Q jumps rapidly but smoothly during the transition from elastic to plastic deformation.

Another interesting question is how strongly the ambient temperature affects the dislocation density ρ and the configurational temperature χ. Fig. 3.6 and Fig. 3.7 show their normalized

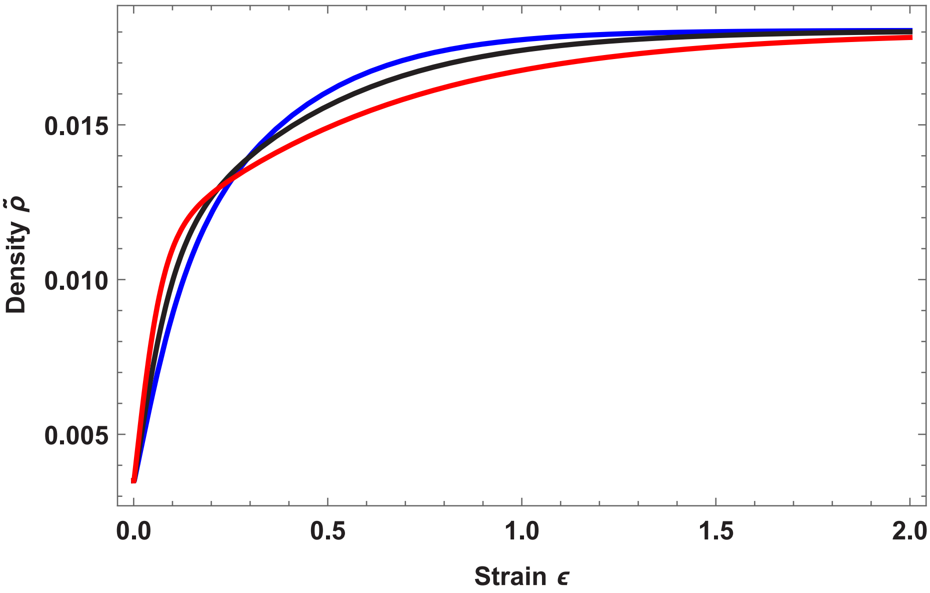

Figure 3.6: Theoretical dislocation density distribution for pure aluminum at the strain rate $\dot{\epsilon} = 25\,s^{-1}$, for temperatures $300\,C,\ 400\,C,\ 500\,C$ shown from right to left.

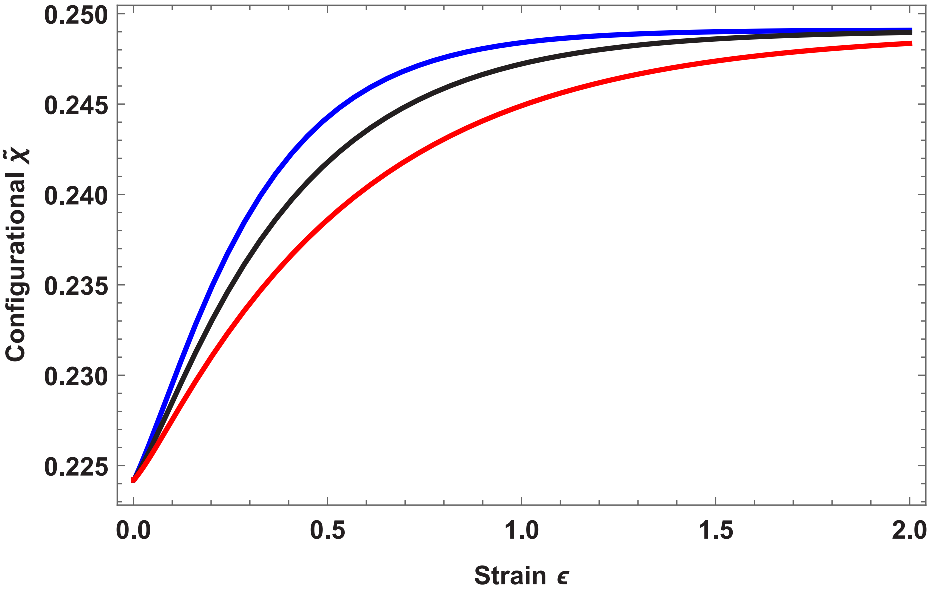

Figure 3.7: Theoretical configurational temperature for pure aluminum at the strain rate $\dot{\epsilon} = 25\,s^{-1}$, for temperatures $300\,C,\ 400\,C,\ 500\,C$ shown from left to right.

distributions at strain rate $\dot{\epsilon} = 25\,s^{-1}$ for three different temperatures $300\,C,\ 400\,C,\ 500\,C$. The equation of motion relating to the internal variable $\tilde{\chi}$ is the first law of thermodynamics applied to the configurational subsystem. The right-hand side of Eq. (3.3) shows the fraction of plastic power delivered to this system that increases the configurational temperature. At fixed strain rate Q, the higher the ambient temperature, the higher plastic strain rate q/Q, however, the lower the stress σ since the dislocations are easier to be depinned. It is, therefore, the configurational temperature would be lower for higher ambient temperature.

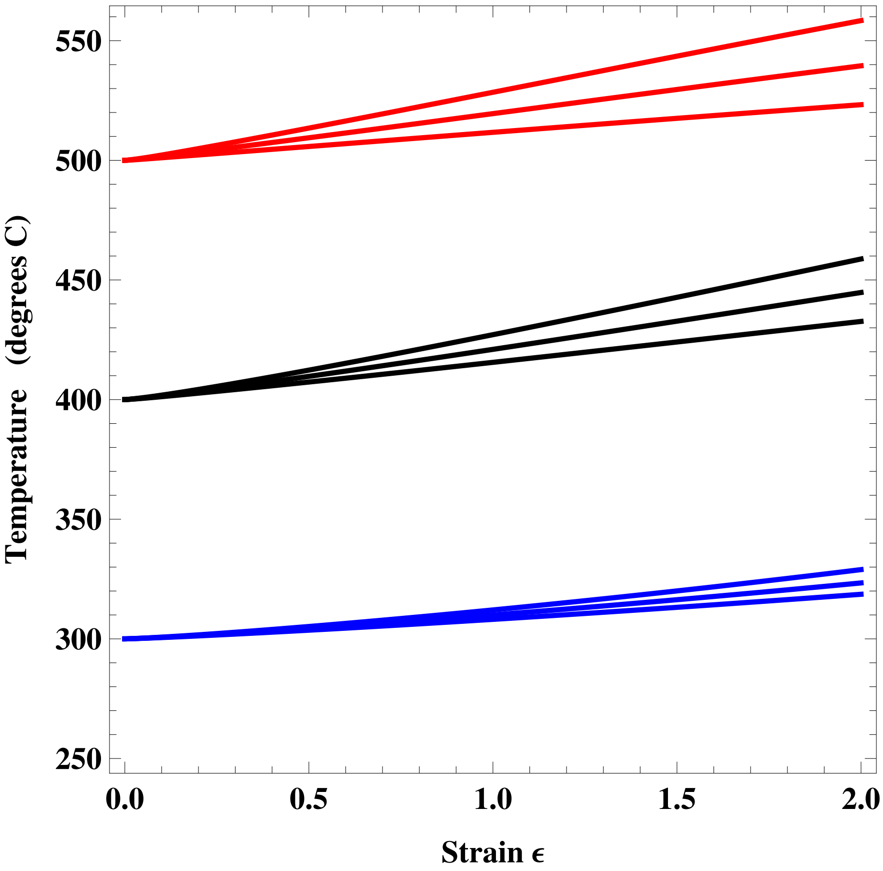

Figure 3.8: Temperature as a function of strain for each of the nine stress-strain tests shown for aluminum in the preceding figures. The initial ambient temperatures are $300\,C$, $400\,C$ and $500\,C$ (blue, black, and red) as seen on the left axis. Each group of three curves is for strain rates of $\dot{\epsilon} = 0.25\,s^{-1},\ 2.5\,s^{-1}$, and $25\,s^{-1}$, from bottom to top.

To complete the analysis of the Shi et al. (1997a) data for pure aluminum, Fig. 3.8 shows computed temperatures as functions of strain for each of the nine stress-strain curves shown in the previous figures. Here, the author may be finding an interesting discrepancy between the interpretation and that of Shi et al. (1997a). Those investigators say that “In the high strain rate tests, particularly at low temperatures, temperature rises of up to $30\,K$ was observed at the start of steady state.” temperature rises of roughly that magnitude can be seen in this calculation. However, as stated above, the author does not think that these tests have reached steady state, especially not the one at the highest strain rate and lowest temperature is shown at the top of Fig. 3.3, which is still softening at large strain. Also, as shown in Fig. 3.8, a prediction is taken that the larger increases of temperature occur at the higher ambient temperatures; because the data analysis tells that the thermal conversion factor $K(\tilde{\theta})$ in Eq. (3.4), is more significant there.

3.1.3 Comparison with experiment: Steel

As a second example of thermal processing data is demonstrated here, the Fe-30% Ni austenitic alloy studied by Abbod et al. (2007). According to those authors, this alloy is a good model material for studying hot deformation of the austenitic phases of carbon-manganese steels. For simplicity, it is referred to henceforth simply as “steel”. The experimental data was digitized from their Fig. 1 and shown it here in Figs. 3.9, 3.10 and 3.11. In analogy to the presentation of the aluminum data in Sec. 3.1.2, these figures are shown in order of increasing strain rate, $\dot{\epsilon} = 0.1\,s^{-1}$, $1.0\,s^{-1}$, and $10\,s^{-1}$. Within each figure, there are curves for the three different temperatures $850\,C$, $950\,C$, and $1050\,C$ (blue circles, black triangles, and red squares respectively) shown from top to bottom.

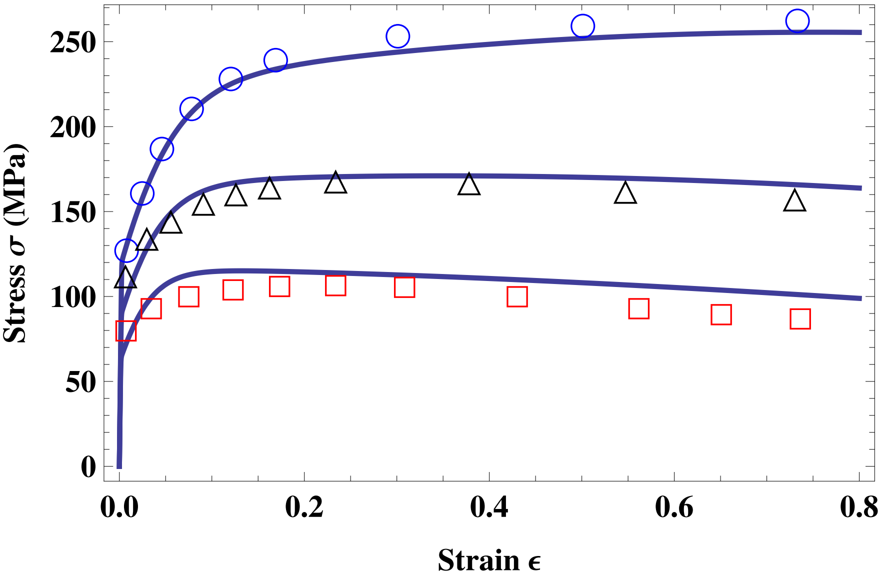

Figure 3.9: Stress-strain curves for steel at the small strain rate $\dot{\epsilon} = 0.1\,s^{-1}$, for temperatures $850\,C$, $950\,C$, $1050\,C$ shown from top to bottom. The experimental points are taken from Abbod et al. (2007).

In analyzing this data, the same least-squares method that used for aluminum have been implemented here. they are found: $T_P = 4.59 \times 10^4\,K$, $r = 0.122$, $\chi_0 = 0.284$, $\kappa_1 = 0.958$, $\kappa_2 = 5.43$, $\tilde{\rho}_i = 0.0023$, $\tilde{\chi}_i = 0.215$, and $K_2 = 0$. The one interesting difference is that a slightly nonlinear thermal conversion factor of the form

$$K(\tilde{\theta}) = K^*\,e^{-T^*/T_P\,\tilde{\theta}} \tag{3.9}$$

seems to produce a better fit to the data than the linear form used previously. they are found to be $K^* = .00879$ and $T^* = 8390\,K$. The activated form of this equation is suggestive but probably not meaningful; note that it is used only over a narrow range of temperatures. The following approximation for the shear modulus is also used (derived from data given in Galindo-Nava and Rivera-Díaz-del Castillo (2013)):

$$\mu(\tilde{\theta}) = 85,970 - 33.6\,T_P\,\tilde{\theta} + 0.0009\,(T_P\,\tilde{\theta})^2. \tag{3.10}$$

Once again, the results of this analysis seem to be within the bounds of experimental uncertainties. The one visible discrepancy is for the top curve in Fig. 3.9, for $\dot{\epsilon} = 10\,s^{-1}$ and

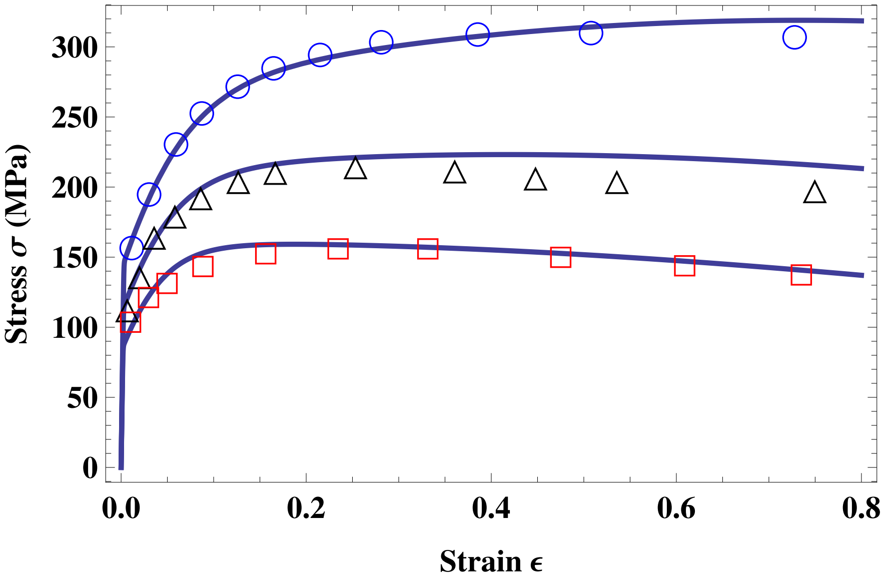

Figure 3.10: Stress-strain curves for steel at the strain rate $\dot{\epsilon} = 1.0\,s^{-1}$, for temperatures $850\,C$, $950\,C$, $1050\,C$ shown from top to bottom. The experimental points are taken from Abbod et al. (2007).

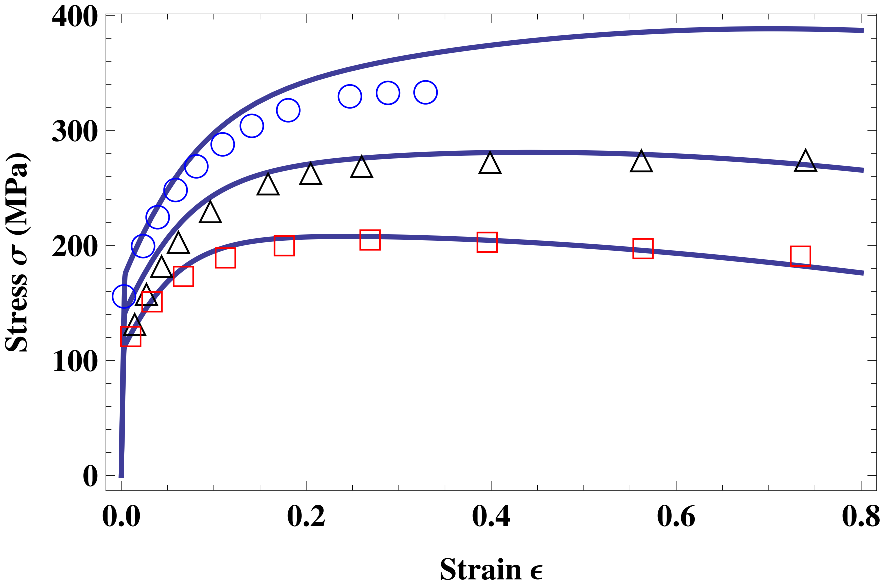

Figure 3.11: Stress-strain curves for steel at the highest strain rate $\dot{\epsilon} = 10\,s^{-1}$, for temperatures $850\,C$, $950\,C$, $1050\,C$ shown from top to bottom. The experimental points are taken from Abbod et al. (2007).

ambient temperature $850\,C$, where the experimental data drops below the author's prediction at a relatively small strain.

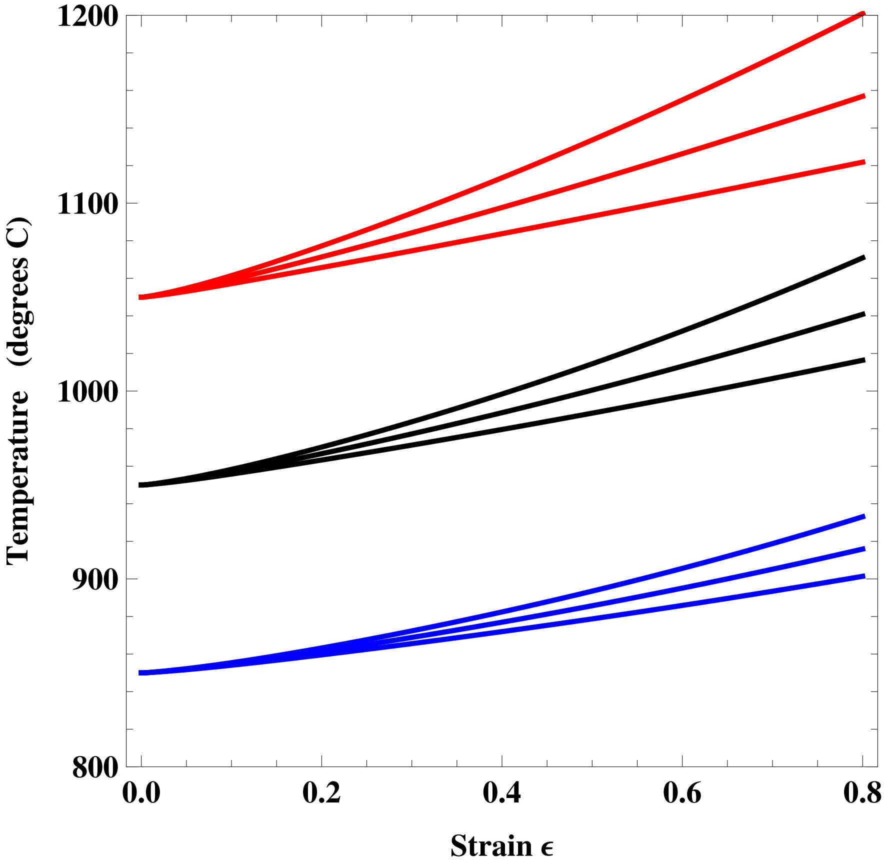

Figure 3.12: Temperature as a function of strain for each of the nine stress-strain tests shown for steel in the preceding figures. The initial ambient temperatures are $850\,C$, $950\,C$ and $1050\,C$ (blue, black, and red) as seen on the left axis. Each group of three curves is for strain rates of $\dot{\epsilon} = 0.10\,s^{-1}$, $1.0\,s^{-1}$, and $10\,s^{-1}$, from bottom to top.

The potentially most serious discrepancy pertains to the strain dependence of predicted temperatures, shown here in Fig. 3.12 in analogy to the temperatures for aluminum shown in Fig. 3.8. Supposedly the same temperatures are shown by Abbod et al. (2007) in their Fig.2, but those temperatures are not measured directly. Apparently, they are computed from the stress-strain data, perhaps using a temperature-independent thermal conversion factor. Their orders of magnitude and growth as functions of strain rate at fixed ambient temperatures are similar to the simulated results here, but their dependence on the ambient temperatures themselves is qualitatively different.

Note finally that, with $s = 0.122$ and $\alpha = 4$, the ratio of the depinning length to the length of the Burgers vector becomes 0.48 which, if true, would imply an interestingly nontrivial atomic-scale structure for the interaction between dislocations.

3.1.4 Discussions

On the whole, these results seem to be quite satisfactory. Note that the thermodynamic dislocation theory is used now not just to test its validity but also as a tool for discovering properties of structural materials. For example, the author did not know at the beginning of this investigation that thermal softening would play so important a role even for the samples subjected to very slow deformations at moderately low temperatures. One of the main reasons for the success of this theory is the extreme sensitivity of the plastic strain rate to small changes in the temperature or the stress.

To put this point in perspective, note the difference between the expression for the dimensionless plastic strain rate q in Eq. (2.44) and the phenomenological approach adopted by Shi et al. (1997a) and Abbod et al. (2007). Both of these groups of investigators base their analyses on the Zener-Hollomon parameter which, in the present notation, is $Z \equiv \dot{\epsilon}\, \exp\left(T_Z/T_P\, \tilde{\theta}\right)$, where T_Z is an activation temperature analogous to T_P. They express their results for different stresses, strains, strain rates and temperatures as functions of Z which, in analogy to Eq. (2.44), means that their strain rate $\dot{\epsilon}$ is proportional to the activation factor $\exp\left(-\,T_Z/T_P\, \tilde{\theta}\right)$ multiplied by some function of the stress. By fitting their data in this way, they find $T_Z/T_P \cong 0.79$ for aluminum and 1.7 for steel. In other words, their estimated activation energies are of roughly the same magnitude as the outcome of this thermodynamic dislocation theory.

One crucial difference between this approach and theirs is that, in Eq. (2.44), the depinning activation barrier is itself a function of the stress and the dislocation density. In this way, the thermodynamic dislocation theory is qualitatively different from conventional theories dating back to Peierls and Nabarro in which dislocations are perceived to be gliding independently through imperfect lattices, resisted by barriers whose dynamical properties are independent of the dislocations themselves. That is not what is happening in the thermodynamic dislocation theory. The nonlinear sensitivity to thermal variations that appears in the present investigation is just a mild version of the same dynamical mechanism that produces yielding transitions and adiabatic shear bands, which have been beyond the reach of conventional dislocation theories.

Even more importantly, the conventional theories are not truly dynamic. For example, in a fully dynamic theory, an activation factor such as the one occurring in the Zener-Hollomon formula should mean that an increase in temperature produces an increase in strain rate which, in turn, increases the rate of heat generation. This is the nonlinear feedback loop that produces the thermal softening seen in this paper and the runaway instability in the theory of adiabatic shear banding Langer (2017a). However, it is not easy to see how such an equation of motion could be incorporated into conventional phenomenological descriptions of dislocation enabled plasticity. This thermodynamic theory has found better ways to make progress in this field by focussing on the nonequilibrium statistical thermodynamics of these systems.

3.2 Adiabatic shear banding in steel

3.2.1 Equations of Motion

According to the work by Marchand and Duffy (1988), they made stress-strain measurements over a range of substantially different temperatures and shear rates using thin steel tubes bonded to torsional Kolsky bar. This experimental model can be simplified by considering a strip of polycrystalline material, of width $2W$, driven in simple shear in the x direction at constant velocities V_x and $-V_x$ at its top and bottom edges respectively. The total strain rate is $V_x/W \equiv Q/t_0$, where $t_0 = 10^{-12}$s is an arbitrarily chosen microscopic time scale that is used in order to express rates as meaningful dimensionless quantities. In order to observe shear localization, spatial variations in the y direction are observed, perpendicular to the x axis.

The local, elastic plus plastic strain rate is $\dot{\varepsilon}(y) = dv_x/dy$, where v_x is the material velocity in the x direction. This motion is driven by a time-dependent, spatially uniform, shear stress σ. Because the overall shear rate is constant, the time t can be replaced by the accumulated total shear strain, say ε, so that $t_0\partial/\partial t \to Q\,\partial/\partial\varepsilon$. Then the dimensionless, y-dependent plastic strain rate is denoted by $q(y,\varepsilon) \equiv t_0\,\dot{\varepsilon}^{pl}(y,\varepsilon)$.

The system of equations of motion for the scaled internal state variables $\tilde{\rho}$, $\tilde{\chi}$, and $\tilde{\theta}$, which are functions of ϵ would be taken from Eqs. (2.51), (2.53), (2.54) with minor modification:

$$\frac{d\tilde{\rho}}{d\epsilon} = \kappa_1\,\frac{\sigma\,q}{\nu(\tilde{\theta},\tilde{\rho},Q)^2\,\mu_T\,Q}\left[1-\frac{\tilde{\rho}}{\tilde{\rho}_{ss}(\tilde{\chi})}\right], \tag{3.11}$$

$$\frac{d\tilde{\chi}}{d\epsilon} = \kappa_2\,\frac{\sigma\,q}{\mu_T\,Q}\left(1-\frac{\tilde{\chi}}{\tilde{\chi}_0}\right), \tag{3.12}$$

$$\frac{\partial\tilde{\theta}}{\partial\varepsilon} = K(\tilde{\theta})\,\frac{\sigma\,q}{Q} + \frac{K_1}{Q}\frac{\partial^2\tilde{\theta}}{\partial y^2} - \frac{K_2}{Q}\,(\tilde{\theta}-\tilde{\theta}_0). \tag{3.13}$$

The equation of motion for the scale, ordinary temperature $\tilde{\theta}$ is the usual thermal diffusion equation with a source term proportional to the input power. We assume that, of the three state variables, only $\tilde{\theta}$ diffuses in the spatial dimension y. Here, $K(\tilde{\theta}) = \beta/(T_P\,c_p\,\rho_d)$ is a thermal energy conversion factor, while $K_1 = k_1 t_0/(c_p\,\rho_d)$ characterizes heat conduction in the axial direction of the tube. c_p is the thermal heat capacity per unit mass, ρ_d is the mass density, $0 < \beta < 1$ is a dimensionless constant known as the Taylor-Quinney factor, and k_1 the thermal conductivity. K_2 is a thermal transport coefficient that controls how rapidly the system relaxes toward the ambient temperature T_0, that is, $\tilde{\theta} \to \tilde{\theta}_0 = T_0/T_P$. As discussed in Le et al. (2017), $K(\tilde{\theta})$ may be non-trivially temperature dependent which, in the range of temperature under consideration, is taken to be

$$K(\tilde{\theta}) = c_0 + c_1\,e^{-c_2/(T_P\,\tilde{\theta})}. \tag{3.14}$$

We assume that K_1 and K_2 are constants, independent of the strain rate and temperature.

It remains to write an equation of motion for the stress $\sigma(\varepsilon)$ which, to an excellent approximation, should be independent of position y for this model of simple shear. Langer (2017a) derived such an equation under the assumption that the shear modulus μ does not depend on temperature. However, if the temperature rises by 600 °C during ASB formation as reported in Marchand and Duffy (1988), then such dependence could be essential. Therefore, We take Hooke's law $\sigma = \mu(\tilde{\theta})[\varepsilon(y) - \varepsilon^{pl}(y)]$, where μ depends on the ordinary temperature $\tilde{\theta}$. Differentiating this equation with respect to ε,

$$\frac{\partial\sigma}{\partial\varepsilon} = \mu(\tilde{\theta})[\frac{t_0}{Q}\frac{dv_x}{dy} - \frac{q(y,\varepsilon)}{Q}] + \mu'(\tilde{\theta})\frac{\partial\tilde{\theta}}{\partial\varepsilon}[\varepsilon(y) - \varepsilon^{pl}(y)]. \tag{3.15}$$

Neglecting the second term as small compared with the first and averaging over the width, we obtain

$$\frac{\partial\sigma}{\partial\varepsilon} = \frac{1}{2W}\left\{\left[\mu(\tilde{\theta})\frac{t_0}{Q}v_x\right]_{\tilde{\theta}(-W)=\tilde{\theta}_0}^{\tilde{\theta}(+W)=\tilde{\theta}_0} - \int_{-W}^{+W}\mu'(\tilde{\theta})\frac{d\theta}{dy}\frac{t_0}{Q}v_x dy - \int_{-W}^{+W}\mu(\tilde{\theta})\frac{q(y,\varepsilon)}{Q}dy\right\}. \tag{3.16}$$

When integrating terms on the right-hand side of Eq. (3.16), the term containing the derivative $\mu'(\tilde{\theta})$ is neglected as being small compared to the remaining terms. Also, Dirichlet boundary conditions are assumed: $\tilde{\theta}(\pm W) = \tilde{\theta}_0$, Eq. (3.16) simplified to:

$$\frac{\partial\sigma}{\partial\varepsilon} = \mu(\tilde{\theta}_0) - \int_{-W}^{+W}\frac{\mu(\tilde{\theta})}{2W}\frac{q(y,\varepsilon)}{Q}dy. \tag{3.17}$$

Note that Eq. (3.17) differs slightly from Eq. (2.55) in Chapter 2, because here the dependence of shear modulus on temperature is taken into account. For the numerical solution of Eqs. (3.13) and (3.17) it is convenient to introduce the dimensionless coordinate $\tilde{y} = y/W$. Then, Eqs. (3.13) and (3.17) keep their form if $\tilde{y}$ is substituted for y, while $K_1 \to \tilde{K}_1 = k_1 t_0/(c_p\,\rho_d W^2)$.

To complete this model of the ASB experiments, one needs to specify an instability-triggering mechanism analogous to the long, shallow "notch" that Marchand and Duffy inscribed along their equivalent of our x axis. This is done – somewhat arbitrarily – by choosing a $\tilde{y}$ dependent value of the initial effective temperature:

$$\tilde{\chi}(0,\tilde{y}) = \tilde{\chi}_i - \delta\exp(-\tilde{y}^2/2y_0^2), \tag{3.18}$$

where δ and y_0 are the depth and width of the perturbation. In using this formula $\delta, y_0 \ll 1$ are usually set to describe a small notch that is about as deep as it is wide. It is emphasized that neither the notch itself nor its assumed dimensions are necessarily realistic aspects of this model and that, for present purposes, one does not need them to be so.

3.2.2 Data Analysis

The experimental results of Marchand and Duffy (1988) for steel HY-100, referred to from here on simply as "steel," along with our theoretical results based on the preceding equations of motion, are shown by the stress-strain curves in Figs. 3.13-3.16. In each of these figures, the points represent the Marchand and Duffy data, and the solid curves are our theoretical results including the $\tilde{y}$-dependent initial perturbation defined in Eq. (3.18). The dashed curves are the partial fits to the small-strain data that used to determine the system parameters as discussed in the following paragraphs.

In order to compute the theoretical stress-strain curves, values for ten system-specific parameters, two initial conditions, and the two perturbative parameters introduced in Eq. (3.18) are required. The ten basic parameters are the following: the activation temperature T_P, the stress ratio r, the steady-state scaled effective temperature $\tilde{\chi}_0$, the two dimensionless conversion factors κ_1 and κ_2, the three coefficients c_0, c_1, and c_2 defining the function $K(\tilde{\theta})$ in Eq. (3.14), and the two thermal factors $\tilde{K}_1$ and K_2. Among them $\tilde{K}_1$ can be determined directly from the known material characteristics of steel and the geometry of the tube. The thermal diffusivity of steel HY-100 is $k_1/(c_p\,\rho_d) = 9 \times 10^{-6}\,\mathrm{m}^2\,\mathrm{s}^{-1}$ Holmquist (1987), and $W = 1.25\,\mathrm{mm}$; thus the author has found $\tilde{K}_1 = 5.76 \times 10^{-12}$. Initial values of the scaled dislocation density $\tilde{\rho}_i(0,\tilde{y}) \equiv \tilde{\rho}_i(\tilde{y})$ and the effective temperature $\tilde{\chi}_i(0,\tilde{y}) \equiv \tilde{\chi}_i(\tilde{y})$ are required; all of which are determined by sample preparation – presumably the same for all samples, but possibly a source of experimental uncertainty. For the ordinary temperature, it is supposed that $\tilde{\theta}(0,\tilde{y}) = \tilde{\theta}_0$. Finally, a formula for the temperature-dependent shear modulus $\mu(T)$, which is taken from Goto et al. (2000) to be

$$\mu(\tilde{\theta}) = \mu_1 - \left[\frac{D}{\exp(T_1/T_P\,\tilde{\theta}) - 1}\right], \tag{3.19}$$

where $\mu_1 = 7.146 \times 10^4\,\mathrm{MPa}$, $D = 2910\,\mathrm{MPa}$ and $T_1 = 215\,\mathrm{K}$.

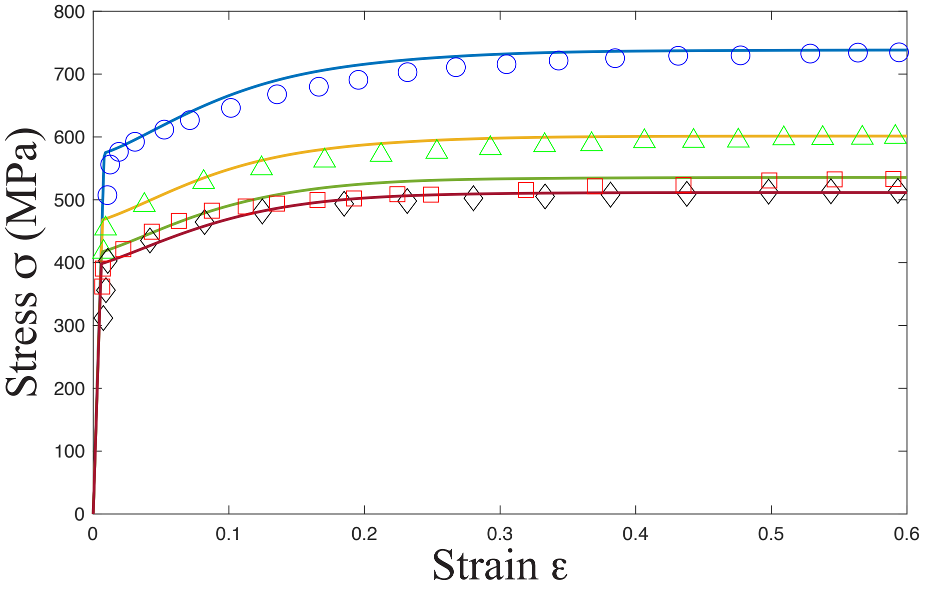

Figure 3.13: Quasi-static stress-strain curves for steel at the strain rate $\dot{\varepsilon} = 10^{-4}/\mathrm{s}$, for temperatures -190 °C, -73 °C, 25 °C, 70 °C shown from top to bottom. The experimental points are taken from Marchand and Duffy (1988).

In earlier studies starting with Langer et al. (2010), Langer and his coworkers were able to begin evaluating the parameters by observing steady-state stresses σ_{ss} at just a few strain rates Q and ambient temperatures $T_0 = T_P\,\tilde{\theta}_0$. Knowing σ_{ss}, T_0 and Q for three stress-strain curves, they could solve Eq. (2.46) for T_P, s, and $\tilde{\chi}_0$, and check for consistency by looking at other steady-state situations. With that information, it was relatively easy to evaluate κ_1 and κ_2 by directly fitting the full stress-strain curves. This strategy does not work here because the thermal effects are highly nontrivial. Examination of the experimental data shown in the figures indicates that all of these samples are undergoing thermal softening at high strain rates and large strains; the stresses are decreasing slowly, and the temperatures must be increasing. Even the curves that appear to have reached some kind of steady state have not, in fact, done so at their nominal ambient temperatures.

Another possible strategy is to use the version of Eq. (2.46) that is valid just at the yield stress σ_y, where the deformation is switching abruptly from elastic to plastic:

$$\sigma_y = s\,\mu\,\sqrt{\tilde{\rho}_i}\,\nu(\tilde{\theta}_0, \tilde{\rho}_i, Q). \tag{3.20}$$

Again, one could use measurements of σ_y to determine T_P, s, and $\tilde{\rho}_i$. Here, however, the problem is that, as seen in the Figures at the higher strain rates, these curves exhibit appreciable stress overshoots that make it difficult to evaluate the yield stresses accurately. In fact, computed curves are presumably consistent with Eq. (3.20), but the author has found it best not to rely exclusively on data at the yield points.

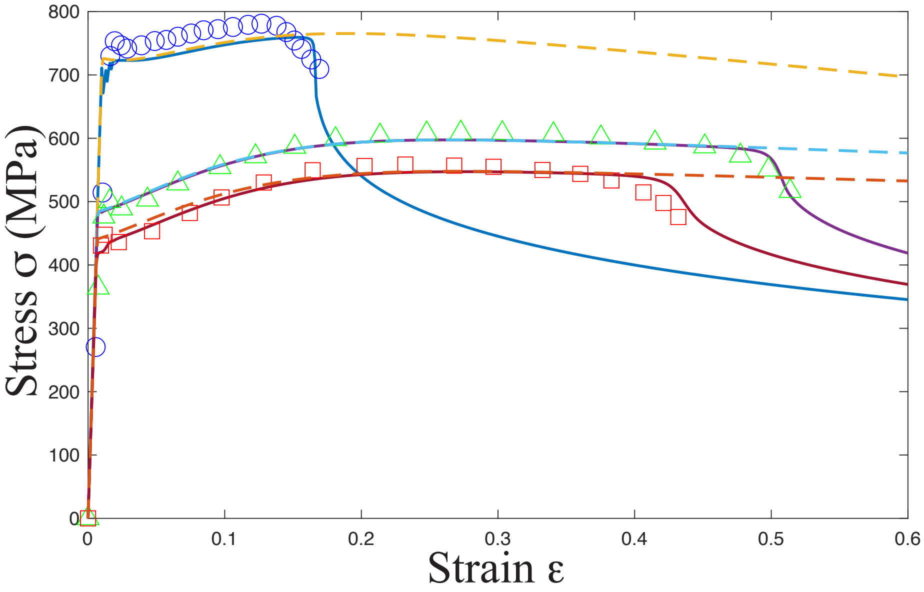

Figure 3.14: Stress-strain curves for steel at the strain rate $\dot{\varepsilon} = 1000/\mathrm{s}$, for temperatures -190 °C, 25 °C, 134 °C shown from top to bottom. The experimental points are taken from Marchand and Duffy (1988).

To counter these difficulties, the large-scale least-squares analyses used in Le and Tran (2017); Le et al. (2017) have been resorted. That is, the sum of the squares of the differences between theoretical stress-strain curves and a large set of selected experimental points are computed, and minimized this sum in the space of the unknown parameters. In order that this procedure is computationally feasible, the author has assumed that the observed stress-strain curves are independent of the notch-like perturbations during the early stages of these experiments, i.e. during what Marchand and Duffy call stages I and II in Figure 12 of their paper Marchand and Duffy (1988). Only this early-stage data has been used for the fitting procedure. In this way, only the four ordinary differential equations considered in Le et al. (2017) is needed to solve. That is, setting $\delta = 0$ in Eq. (3.18) and neglecting the $\tilde{y}$ dependence of state variables. The results are shown by the dashed curves in our Figures.

With just one exception, it is found that all twelve of the Marchand and Duffy early-stage stress-strain curves can be fit with just a single set of system parameters. These are: $T_P = 5.16\times10^5$ K, $s = 0.0178$, $\chi_0 = 0.229$, $\kappa_1 = 7.65$, $\kappa_2 = 14.3$, $c_1 = 4\times10^{-7}$(MPa)$^{-1}$, $c_2 = 2\times10^{-7}$(MPa)$^{-1}$, $c_3 = 400$ K, $\tilde{\rho}_i = 0.0076$, $\tilde{\chi}_i = 0.212$, and $K_2 = 1.66\times10^{-14}$. The single exception is that, at the lowest temperature reported by Marchand and Duffy, -190°C, and for the higher strain rate reported at that temperature, $10^3\,\mathrm{s}^{-1}$, a somewhat larger value of the initial dislocation density is required, $\tilde{\rho}_i = 0.0097$ instead of 0.0076 in order to fit the data. If a equals, say, 10 nm, then initial dislocation densities are all of the order of $10^{14}/\mathrm{m}^2$ (cf.

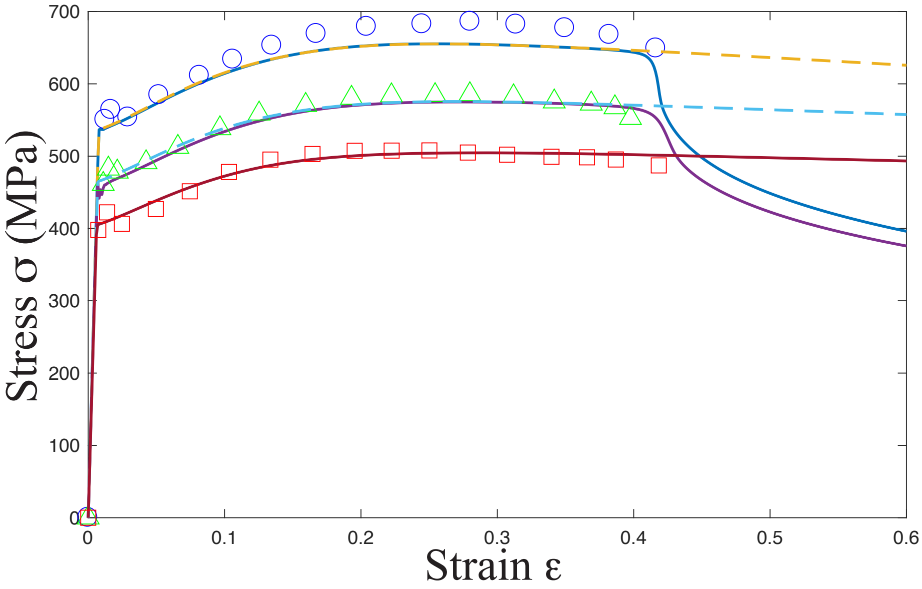

Figure 3.15: Stress-strain curves for steel at the strain rate $\dot{\varepsilon} = 1000/\mathrm{s}$, for temperatures -73 °C, 70 °C, 250 °C shown from top to bottom. The experimental points are taken from Marchand and Duffy (1988).

Basinski and Basinski (1966)). It seems that this agreement between theory and experiment is well within the bounds of experimental uncertainty.

Here is one useful check on the internal consistency of this analysis. With $\rho_d = 7748\,\mathrm{kg/m^3}$ and $c_p = 502\,\mathrm{J/kg\,K}$ (see Holmquist (1987)), the function $K(\tilde{\theta})$ implies a maximum Taylor-Quinney factor $\beta \approx 0.99$ that is slightly smaller than unity within the range of temperatures under consideration.

3.2.3 Adiabatic Shear Banding

Let us turn now to the main topic of this section – the onset and early development of adiabatic shear banding instabilities. To study these phenomena theoretically, the $\tilde{y}$-dependent notchlike initial perturbation defined in Eq. (3.18) is introduced into the equations of motion. Now, the dynamical variables $\tilde{\rho}$, $\tilde{\chi}$, and $\tilde{\theta}$ become functions of $\tilde{y}$, and the complete system of integro-differential equations (3.11)-(3.17) subject to initial and boundary conditions are needed to be solved. To do this, the equations in the interval $(-1 < \tilde{y} < 1)$ are discretized by dividing it into $2n$ sub-intervals of equal length $\Delta\tilde{y} = 1/n$. Then the second spatial derivative of $\tilde{\theta}$ in equation (3.13) is approximated by

$$\frac{\partial^2\tilde{\theta}}{\partial\tilde{y}^2}(\tilde{y}_i) = \frac{\tilde{\theta}_{i+1} - 2\tilde{\theta}_i + \tilde{\theta}_{i-1}}{(\Delta\tilde{y})^2}, \tag{3.21}$$

where $\tilde{\theta}_i = \tilde{\theta}(\tilde{y}_i)$. Similarly, the integral over $\tilde{y}$ of any function $f(\tilde{y})$ is computed by using the trapezoidal rule

$$\int_{-1}^{1} f(\tilde{y})\,d\tilde{y} = \Delta\tilde{y}[f_{-n}/2 + f_{-n+1} + \ldots + f_{n-1} + f_n/2]. \tag{3.22}$$

In this way, the four integro-differential equations are reduced to a system of $6n+1$ ordinary differential equations. These can be numerically solved using the Matlab-ode15s solver with

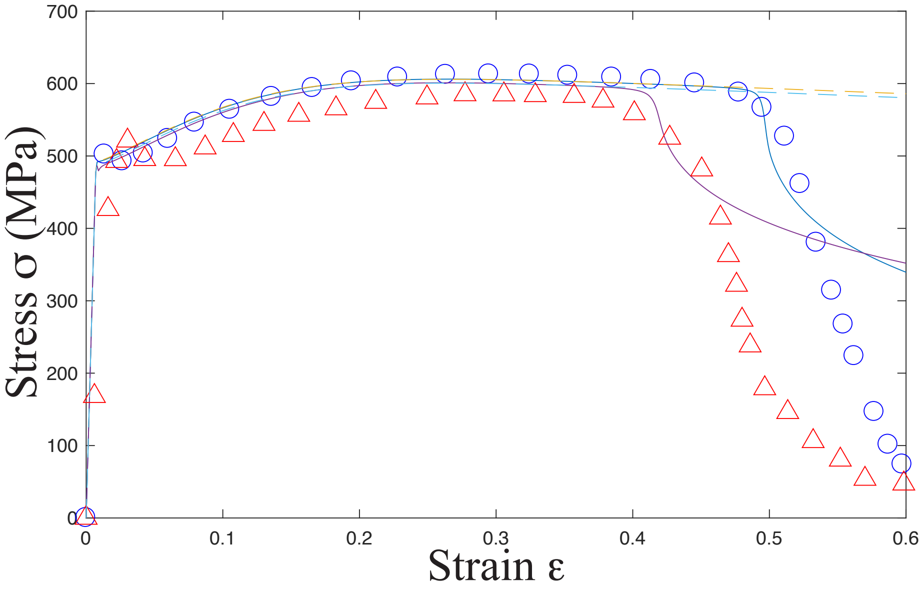

Figure 3.16: Stress-strain curves for steel at the strain rates $\dot{\varepsilon} = 3300/\mathrm{s}$ and $\dot{\varepsilon} = 1600/\mathrm{s}$ shown from top to bottom, for room temperature. The experimental points are taken from Marchand and Duffy (1988).

T (°C) $\dot{\varepsilon}$ (1/s)	-190 1000	-73 1000	25 1000	25 1600	25 3300	70 1000	134 1000	250 1000
δ	0.08	0.026	0.0271	0.0396	0.0172	0.059	0.0823	-
y_0	0.0362	0.026	0.03	0.042	0.0295	0.059	0.0705	-

Table 3.1: The values of δ and y_0

$n = 1000$ and the ε step equal to 0.001. This specific stiff solver can help to improve the efficiency and reliability by supplying the Jacobian matrix or its sparsity pattern. A Matlab supplementary code is also included in the Appendix 5 so that it supports this concept more apparently. Those solutions are shown by the solid lines in Figs. 3.13-3.16 and by the graphs of strain rate and temperature as functions of $\tilde{y}$ in Figs. 3.17-3.20.

As shown in these figures, the perturbation produced by the notch does not affect the overall stress-strain relation either for very small, quasistatic strain rates or during the early stages of the more rapid shear deformations. This is consistent with the assumption when arguing in favor of parameter-fitting procedure. In the quasistatic cases, any extra heat generated near the notch diffuses away quickly on the time scale of the inverse shear rate. During the early stages of the faster deformations, it takes appreciable times (in strain units) before the nonlinear instabilities near the notch grow enough to destabilize the system as a whole. That time before onset, or equivalently the strain at which the stress begins to drop abruptly, is strongly sensitive to the strain rate, the temperature, and the strength of the notch. The values of δ and y_0 that has been chosen to fit the observed onsets are shown in 3.1. It is emphasized again that the irregularity of these values is almost certainly an experimental artifact. There is no reason to believe that this notch model is realistic enough or that Marchand and Duffy could control their initial conditions accurately enough to expect greater precision.

The highly nonlinear onset of banding is seen most clearly in the graphs of the computed fractional strain rate $q(\varepsilon, \tilde{y})/Q$ shown in Fig. 3.17 for $\dot{\varepsilon} = 3300\,\mathrm{s}^{-1}$ at room temperature,

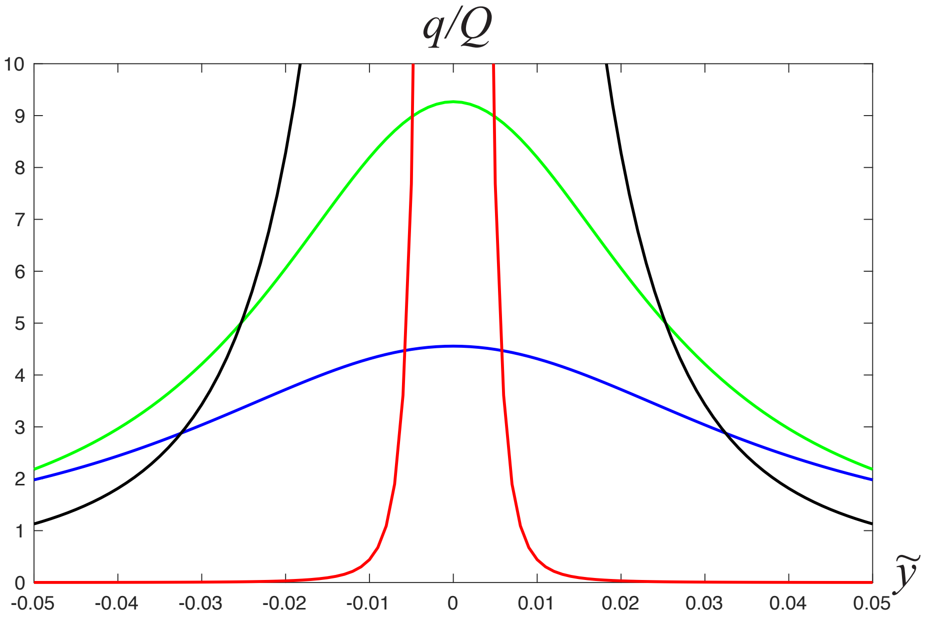

Figure 3.17: Theoretical fractional strain rate distributions for steel for $\dot{\varepsilon} = 3300/\mathrm{s}$ at room temperature: (i) at strain $\varepsilon = 0.45$ (blue), (ii) at strain $\varepsilon = 0.47$ (green), (iii) at strain $\varepsilon = 0.49$ (black), (iv) at strain $\varepsilon = 0.497$ (red).

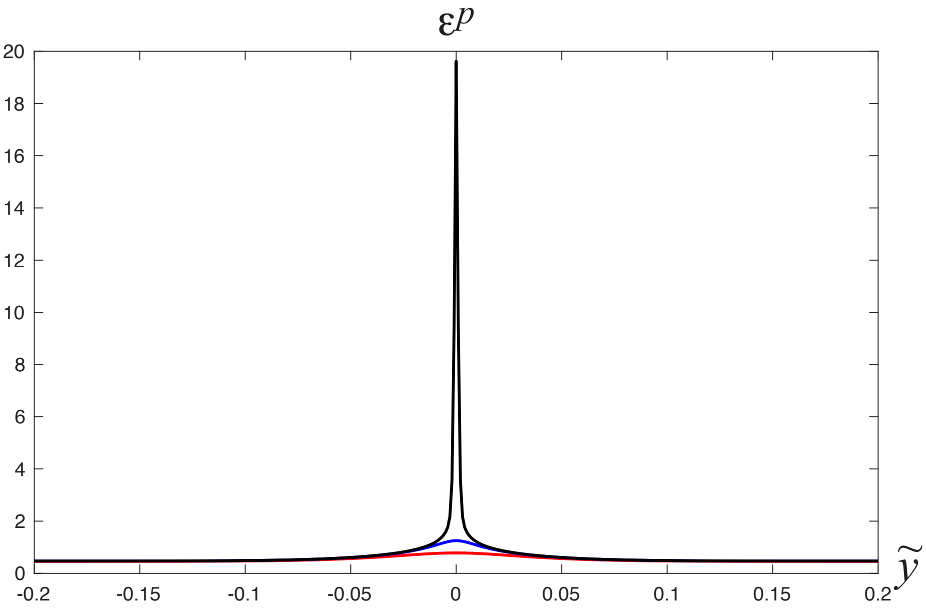

Figure 3.18: Plastic strain distributions for the strain rate $\dot{\varepsilon} = 3300$/s and room temperature at the strains $\varepsilon = 0.47$ (red), $\varepsilon = 0.49$ (blue), and $\varepsilon = 0.51$ (black).

$T \cong 25\,°\mathrm{C}$. The apparent onset strain is $\varepsilon \cong 0.50$. However, at $\varepsilon = 0.45$, q/Q at $\tilde{y} = 0$ has increased by only a factor of about 2, and the width of the perturbation has not increased appreciably from its initial value of $2\,y_0 \cong 0.1$. By $\varepsilon = 0.47$, q/Q has grown by another factor of 2 but the width has not changed, nor has q/Q changed from its initial value of unity outside the emerging band. Finally, by $\varepsilon = 0.49$, the band has begun to sharpen dramatically. By $\varepsilon = 0.497$, it has collapsed into a narrow region of width approximately 0.01 at $\tilde{y} \cong 0$. q/Q has vanished outside the narrow band, and the total strain rate Q is now concentrated inside the band with the maximum of q/Q achieving 1000 in the middle of the band (not shown on the Figure). The overall, uniform stress has dropped to the value that is needed to drive the highly concentrated plastic flow at a high temperature.

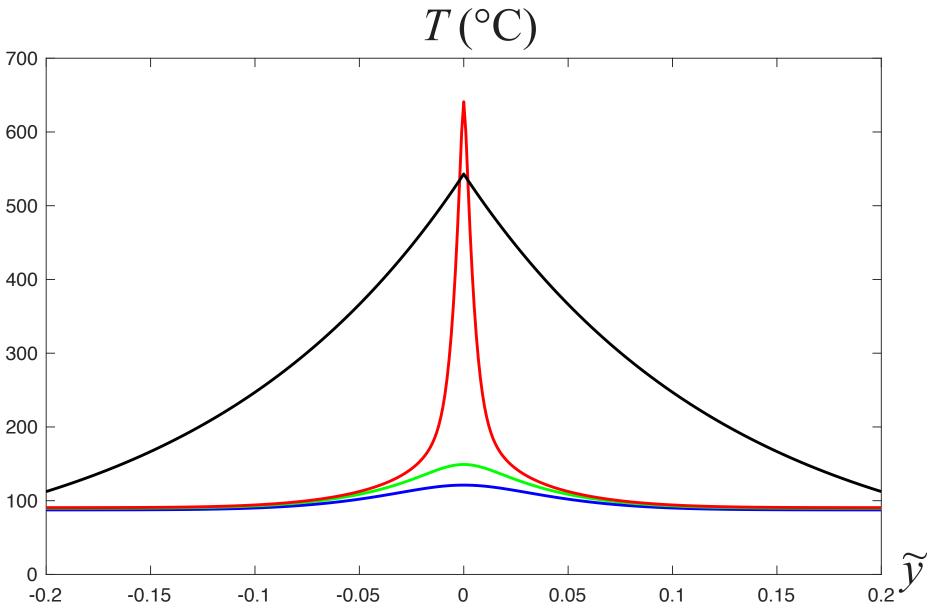

Figure 3.19: Temperature distributions for the strain rate $\dot{\varepsilon} = 3300$/s and room temperature at the strains $\varepsilon = 0.46$ (blue), $\varepsilon = 0.48$ (green), and $\varepsilon = 0.505$ (red). The black curve is the empirical law proposed by Marchand and Duffy (1988).

By integrating $q(\varepsilon, \tilde{y})/Q$ over ε, the distribution of the plastic strain shown in Fig. 3.18 is obtained for $\dot{\varepsilon} = 3300\,\mathrm{s}^{-1}$ at room temperature. At $\varepsilon = 0.47$ the plastic strain is nearly uniform. However, at $\varepsilon = 0.49$ near the onset of ASB the maximum of plastic strain has grown by factor 2. After the formation of ASB, at $\varepsilon = 0.51$ the localization of plastic strain is clearly seen, with the maximum of plastic strain slightly larger than 19. Keeping in mind that the elastic strain remains small, this magnitude agrees with that reported in Marchand and Duffy (1988).

Several graphs of temperature $T = T_P\,\tilde{\theta}(\varepsilon, \tilde{y}) - 273\,\mathrm{K}$ (in Celsius) for $\dot{\varepsilon} = 3300\,\mathrm{s}^{-1}$ at the ambient room temperature, $T \cong 25\,°\mathrm{C}$, are shown in Fig. 3.19, and a graph of the temperature at the center of the band as a function of ε is shown in Fig. 3.20. By $\varepsilon \cong 0.505$ which is the onset of ASB, the latter temperature has reached about $600\,°\mathrm{C}$, which is consistent with the value reported by Marchand and Duffy as shown in their Fig. 20. This consistency is significant. It is based on independently determined thermal parameters; thus it is a sensitive test of the strong nonlinearity of the theory. We also show in Fig. 3.19 the empirical law proposed by Marchand and Duffy, $T = a\,e^{-7.875|\tilde{y}|}$ ($a = 543\,°\mathrm{C}$), that is based on several measurements of temperature at somewhat different strain rates. This empirical distribution of temperature is wider than our simulated distribution, possibly because it was

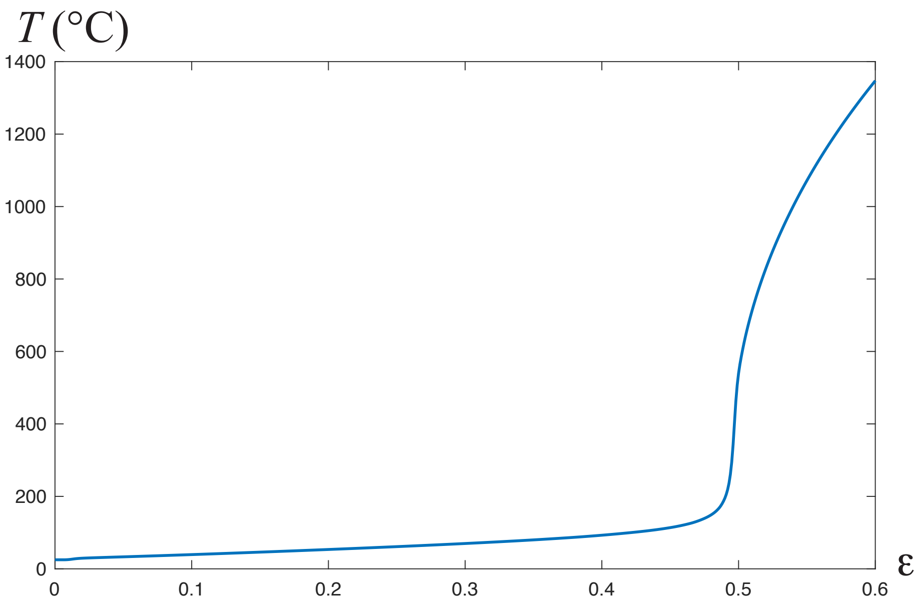

Figure 3.20: Temperature at the center of the shear band ($\tilde{y} = 0$) for the strain rate $\dot{\varepsilon} = 3300/\mathrm{s}$ and room temperature as the function of the strain.

measured at a significantly larger strain where more heat had been generated in the band and had diffused into the neighboring material.

The experimental stress drops following the onset of banding are generally much deeper than predicted by our theory. This seems reasonable because there must be other physical mechanisms that come into play in this regime. There is probably a transition between shear banding and fracture, during which the resistive mechanism switches from high-temperature plasticity to friction between the faces of two separate materials in contact with each other.

3.2.4 Discussions

The main conclusion of this section is that the statistical thermodynamic dislocation theory provides an accurate picture of adiabatic shear banding as observed by Marchand and Duffy (1988). The theory's description of the coupling between stress, temperature, and strain rate accounts quantitatively for the strong thermal instabilities leading to abrupt stress drops seen in those experiments.

More generally, two different kinds of issues are addressed here, one pertaining to first-principles theoretical physics and the other to applied materials research. On the one hand, the validity of the thermodynamic dislocation theory is being tested. On the other, the author is trying to find ways in which these new insights can be used to predict the performance of materials in engineering applications.

Because this theoretical starting point is unconventional, the author has made special efforts to construct and test it as rigorously as possible. Stringent requirements have been imposed on the equations of motion and on the choice of the parameters that appear in them. The equations themselves are statements of well known physical principles – conservation of energy and flow of entropy in accord with the second law of thermodynamics –, and they are expressed in terms of properly defined internal state variables – the dislocation density and the two thermodynamically defined temperatures. No phenomenological fitting functions are postulated. Each of the parameters that occur in the equations can, in principle, be determined either by independent measurement or first-principles computation.

A strong additional postulate is designed to test the validity of this theory. Specifically, an assumption has been proposed that almost all of the fundamental parameters remain constant across the wide range of strain rates and temperatures that are explored. This postulate includes conversion factors like κ_1 and κ_2, which are variables in some circumstances, and it also includes initial conditions that are subject to uncertainties of sample preparation. Nevertheless, this postulate works remarkably well. The twelve stress-strain curves shown in Figs. 3.13-3.16 are all in reasonable agreement with experiment. The main exception is the top curve in Fig. 3.14 where there is slightly adjusted the initial value of the dislocation density $\tilde{\rho}_i$ as discussed at the end of Subsection 3.2.2. A similar adjustment of one of the $\tilde{\rho}_i$'s in Fig. 3.16 might have improved the agreement with the experiment for the two curves shown there. The important point, however, is that these minor disagreements are much more likely to have been caused by experimental inaccuracies than by systematic errors in the theory.

Similarly, the stress overshoots at the initial yield points that appear in all the high-strain-rate experimental Marchand and Duffy curves in Figs. 3.14-3.16 are almost certainly instrumental effects having to do with the sudden onset of shear stress. As shown in Fig. 7 of Langer (2017b), the author can reproduce those overshoots simply by reducing the initial values of the scaled effective temperature $\tilde{\chi}_i$ slightly. However, doing so would require readjusting the $\tilde{\chi}_i$'s for the quasistationary cases where no overshoots occur. Thus, like the failure during late-stage ASB, the initial stress overshoots are caused by physical mechanisms outside the range of this theory.

By far the most important outstanding questions are those pertaining to physical interpretations of this theory and, thus, to connections between the theory and its applications. The skeptical reader will have noticed that terms such as "cross slip," "stacking fault," "dislocation pile-up," or even "crystal symmetry" or "glide plane" do not appear in this chapter. It is argued that physical concepts like these belong in first-principles calculations of dynamic quantities such as κ_1, κ_2 or the parameter r that determines the relationship between stress and plastic strain rate. The standard practice in conventional literature has been to try to go directly from observed microscopic behaviors of small groups of dislocations to phenomenological models of strain hardening or fracture toughness. That strategy, however, has not succeeded in producing usefully predictive theories. The present line of investigation seems to be more promising.

3.3 Torsion of bars in copper

3.3.1 Equations of motion

Suppose a single crystal bar with a circular cross-section, of radius R and length L, is subjected to torsion (see the bar with its cross-section in Fig. 3.21). For this particular geometry of the bar and under the condition $R \ll L$ it is natural to assume that the warping

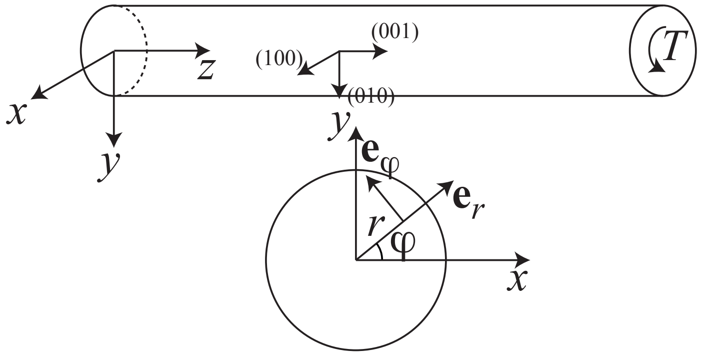

Figure 3.21: Torsion of a single crystal bar.

of the bar vanishes, while the circumferential displacement is $u_\varphi = \omega r z$, with ω being the twist angle per unit length. Thus, the total shear strain of the bar $\gamma = 2\epsilon_{\varphi z} = \omega r$ and the shear strain rate $\dot{\gamma} = \dot{\omega} r$ turn out to be non-uniform as they are linear functions of radius r. The equation of motion for the shear stress which is Hooke's law in rate form

$$\dot{\tau} = \mu(\dot{\gamma} - q(\gamma)/t_0), \tag{3.23}$$

with μ being the shear modulus. Note that $q(\gamma)/t_0$ equals the plastic shear rate and t_0 is a characteristic microscopic time scale. Now, let this system be driven at a constant twist rate $\dot{\omega} \equiv \varpi_0/t_0$. We can replace the time t by the total twist angle (per unit length) ω so that $t_0\, \partial/\partial t \to \varpi_0\, \partial/\partial\omega$:

$$\frac{\varpi_0}{t_0}\frac{\partial\tau}{\partial\omega} = \mu\left(r\frac{\varpi_0}{t_0} - \frac{q(\gamma)}{t_0}\right). \tag{3.24}$$

After simplification, the Hooke's law in rate form becomes

$$\frac{\partial\tau}{\partial\omega} = \mu\left[r - \frac{q(\gamma)}{\varpi_0}\right]. \tag{3.25}$$

The system of equations of motion for the scaled internal state variables $\tilde{\rho}$, $\tilde{\chi}$, which are functions of r and ω would be taken from Eqs. (2.51), (2.53) with minor modification:

$$\frac{\partial\tilde{\rho}}{\partial\omega} = \kappa_1\,\frac{\tau\, q}{\tilde{\nu}(\theta,\tilde{\rho},\varpi_0 r)^2\mu_T\,\varpi_0}\left[1 - \frac{\tilde{\rho}}{\tilde{\rho}_{ss}(\tilde{\chi})}\right], \tag{3.26}$$

$$\frac{\partial\tilde{\chi}}{\partial\omega} = \kappa_2\,\frac{\tau\, q}{\mu_T\varpi_0}\left(1 - \frac{\tilde{\chi}}{\tilde{\chi}_0}\right), \tag{3.27}$$

For the purpose of numerical integration, let us introduce the following variables:

$$\tilde{r} = r/R, \quad \tilde{\tau} = \tau/\mu, \quad \phi = R\omega/\eta, \quad \eta = \frac{\pi R}{180^\circ L}, \quad \tilde{\varpi}_0 = (a/b)R\varpi_0,$$

where the scaled shear stress is $\tilde{\tau} = \tau/\mu$, the scaled radius $\tilde{r}$ changes from zero to 1. The variable ϕ has the meaning of the total twist angle measured in degree (in Horstemeyer et al. (2002) ϕ changes from zero to $\phi_* = 73.35^\circ$). The calculation of the torque as a function of ϕ is convenient for the later comparison with the torque-twist curve from Horstemeyer et al. (2002). Then, the system of equation Eqs. (3.25), (3.26), (3.27) becomes

$$\frac{\partial \tilde{\tau}}{\partial \phi} = \eta \left[\tilde{r} - \frac{q(\tilde{\tau}, \tilde{\rho})}{\tilde{\varpi}_0} \right], \tag{3.28}$$

$$\frac{\partial \tilde{\rho}}{\partial \phi} = \eta \kappa_1 \, \frac{\tilde{\tau}\, q}{\tilde{\nu}(\theta, \tilde{\rho}, \tilde{\varpi}_0 r)^2 \, \varpi_0} \left[1 - \frac{\tilde{\rho}}{\tilde{\rho}_{ss}(\tilde{\chi})} \right], \tag{3.29}$$

$$\frac{\partial \tilde{\chi}}{\partial \phi} = \eta \kappa_2 \, \frac{\tilde{\tau}\, q}{\tilde{\varpi}_0} \left(1 - \frac{\tilde{\chi}}{\tilde{\chi}_0} \right). \tag{3.30}$$

To solve this system of differential equations subject to initial conditions numerically, we discretize the equations in the interval $(0 < \tilde{r} < 1)$ by dividing it into n sub-intervals of equal length $\Delta \tilde{r} = 1/n$ and writing the corresponding equations at n nodes $\tilde{r}_i = i \Delta \tilde{r}$, $i = 1, \ldots, n$. In this way, we reduce the three differential equations depending on $\tilde{r}$ to a system of $3n$ ordinary differential equations at n nodes that will be solved by Matlab-ode15s.

After finding the solution, we can compute the torque as a function of the twist angle according to

$$T = 2\pi \mu R^3 \int_0^1 \tilde{\tau} \tilde{r}^2 d\tilde{r}. \tag{3.31}$$

3.3.2 Parameter identification and numerical simulations

In order to simulate the theoretical torque-twist curves, we need values for five system-specific parameters and two initial conditions from each sample. The five basic parameters are the following: the activation temperature T_P, the stress ratio s, the steady-state scaled effective temperature $\tilde{\chi}_0$, and the two dimensionless conversion factors κ_1 and κ_2. We also need initial values of the scaled dislocation density $\tilde{\rho}_i$ and the effective disorder temperature $\tilde{\chi}_i$; all of which are determined by the sample preparation. The other parameters required for numerical simulations but known from the experiment are: the ambient temperature $T = 298$K, the shear modulus $\mu = 48$GPa, the length $L = 17.6$mm and radius $R = 6.35$mm of the bar, the length of Burgers' vector $b = 2.55$Å, the twist rate $\dot{\phi} = 0.25°/$s, and consequently, $\tilde{\varpi}_0 = 1.57427 \times 10^{-15}/$s. Since a corresponds to the smallest admissible distance between dislocations in the state of maximum disorder in crystal, we take $a = 10b$. Note that a only affects the dislocation density, not the torque-twist curves.

In earlier studies dealing with the uniform deformations (Langer, 2015, 2016, 2017a; Langer et al., 2010), it was possible to begin evaluating the parameters by observing steady-state stresses σ_{ss} at just a few strain rates Q and ambient temperatures $T_0 = T_P \, \tilde{\theta}_0$. Knowing σ_{ss}, T_0 and Q for three stress-strain curves, one could solve equation

$$\sigma = \sigma_T(\tilde{\rho}) \, \nu(\tilde{\theta}, \tilde{\rho}, Q), \tag{3.32}$$

which is the inverse of Eq. (2.44) for T_P, s, and $\tilde{\chi}_0$, and check for consistency by looking at other steady-state situations. With that information, it was relatively easy to evaluate κ_1 and κ_2 by directly fitting the full stress-strain curves. This strategy does not work here because the stress state of twisted bars is non-uniform. We may still have local steady-state

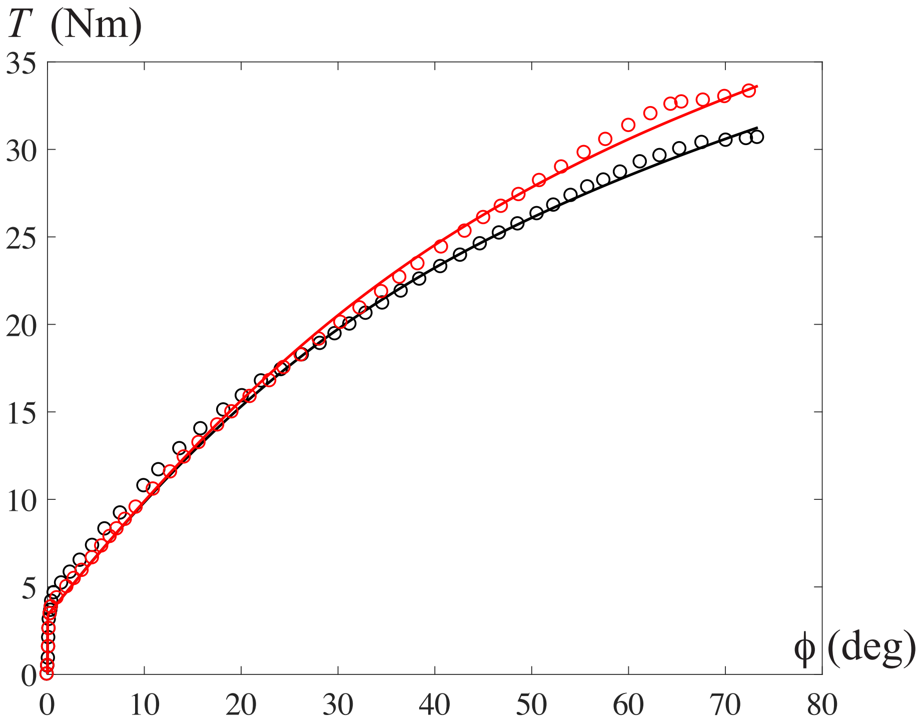

Figure 3.22: The torque-twist curves at the twist rate $\dot{\phi} = 0.25°/\text{s}$ and for room temperature: (i) sample 1: TDT-theory: black curve, experiment Horstemeyer et al. (2002): black circles (ii) sample 2: TDT-theory: red/dark gray curve, experiment Horstemeyer et al. (2002): red/dark gray circles.

stresses as a function of the radius r, but it is impossible to extract this information from the experimental torque-twist curve. Furthermore, the similar parameters for copper found in (Langer, 2015, 2016, 2017a; Langer et al., 2010) cannot be used here, since we are dealing with torsional deformations having the energy barrier T_P and other characteristics different from those identified in the above references.

To counter these difficulties, we have resorted to the large-scale least-squares analyses that we have used in (Le and Tran (2017); Le et al. (2017)). That is, we have solved the system of ordinary differential equations (ODEs) numerically, provided a set of material parameters is known. Based on this numerical solutions we then computed the sum of the squares of the differences between our theoretical torque-twist curves and a large set of selected experimental points, and minimized this sum in the space of the parameters. The ODEs were solved numerically using the Matlab-ode15s, while the finding of least squares was realized with the Matlab-globalsearch. To keep the calculation time manageable and simultaneously ensure the accuracy, we have chosen $n = 1000$ and the ϕ-step equal to $\phi_*/7335$. We have found that the torque-twist curves for both samples taken from Horstemeyer et al. (2002) can be fit with just a single set of system parameters. These are: $T_P = 26976\,\text{K}, s = 0.0152$, $\chi_0 = 0.2496$, $\kappa_1 = 50.3$, $\kappa_2 = 377$. The initial parameters for sample 1 are: $\tilde{\rho}_{i1} = 6.04 \times 10^{-5}$, $\tilde{\chi}_{i1} = 0.187$, while for sample 2 we have: $\tilde{\rho}_{i2} = 6 \times 10^{-5}$, and $\tilde{\chi}_{i2} = 0.2$. The precision of the fit could be measured by the minimum of the sum of squares which is equal to $f_{min} = 48.442\,\text{N}^2\text{m}^2$ in this case. Note that f_{min} depends also on the number of points selected from the experimental torque-twist curves. The mean square of the deviation (or the square of the error per point) can be characterized by f_{min}/N, where N is the total number of points. We took 48 points from each curve of Horstemeyer et al. (2002), so the

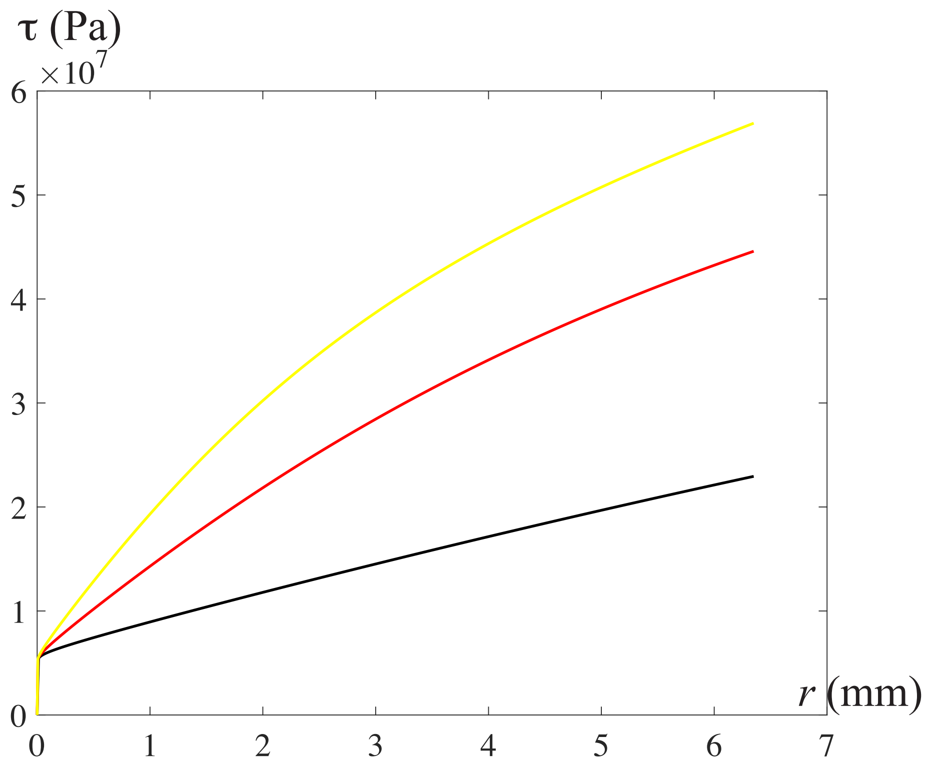

Figure 3.23: Stress distribution $\tau(r)$ at the twist rate $\dot{\phi} = 0.25°/\mathrm{s}$ and for room temperature: (i) $\phi = 10°$ (black), (ii) $\phi = 30°$ (red/dark gray), (iii) $\phi = 50°$ (yellow/light gray).

mean square of the deviation is approximately $0.5\,\mathrm{N}^2\mathrm{m}^2$. Numerous numerical results of the least squares analysis with the disturbed torque-twist curves (not shown in the paper) confirm that our method for parameter identification is robust against small experimental uncertainties. For comparison we show the values of basic parameters for copper identified for uniform compression tests in Langer et al. (2010): $T_P = 40800\,\mathrm{K}, s = 0.032$, $\chi_0 = 0.25$, $\kappa_1 = 96.875$, $\kappa_2 = 350$. As already mentioned, the dislocations in those tests, in contrast to the predominantly screw dislocations in our torsion tests, are of edge character, so that the differences between the basic parameters are not surprising.

With the identified parameters we can now simulate the torque-twist curves for the single crystal copper bars. The result is presented in Fig. 3.22. In this figure, the circles represent the selected experimental points in Horstemeyer et al. (2002) while the solid curves are our theoretical simulation. One can see that even the initial yielding transition appears to be described accurately by this theory. There is only two visible discrepancies: for sample 1 and for $\phi \in (0°, 25°)$ the torques are slightly above those predicted by the theory, and for large twist angles ($\phi > 70°$) they are slightly below those predicted by the theory. For sample 2 the torques are slightly above those predicted by the theory for $\phi \in (60°, 70°)$. Nothing about this result leads us to believe that there are relevant physical ingredients missing in the theory.

The results of numerical simulations for other quantities using the above set of parameters and the initial values of sample 1 are shown in Figs. 3.23-3.26. We plot in Fig. 3.23 the shear stress distribution τ at three different twist angles $\phi = 10°$ (black), $\phi = 30°$ (red/dark gray), and $\phi = 50°$ (yellow/light gray). In a small elastic zone near the center of the cross-section, the stress depends linearly on r. In the plastic zone, the stress does not remain constant but

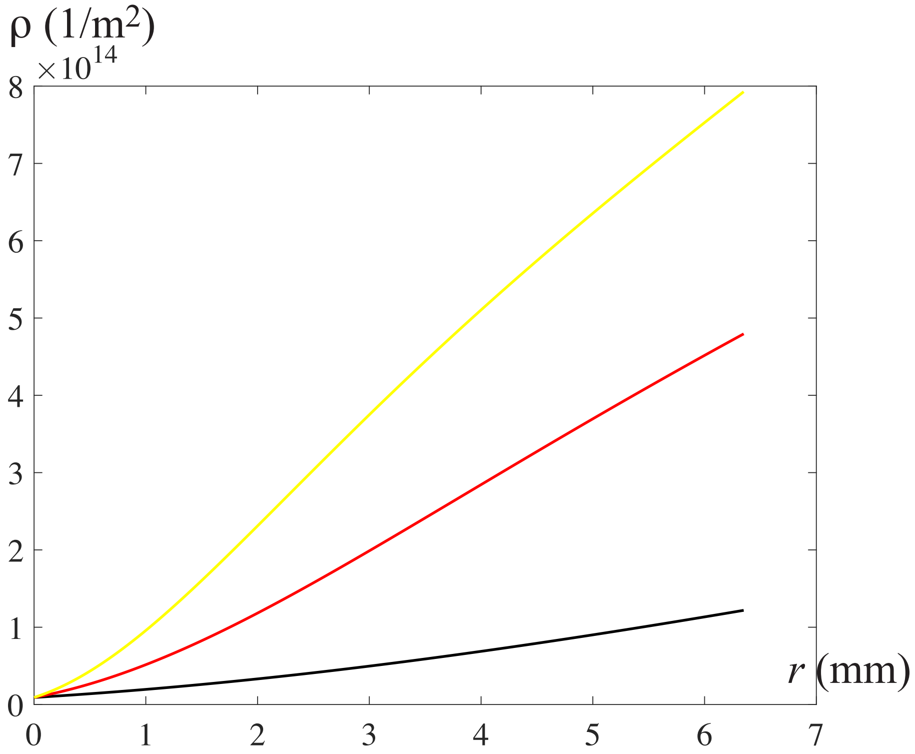

Figure 3.24: Total density of dislocations $\rho(r)$ at the twist rate $\dot{\phi} = 0.25°/\text{s}$ and for room temperature: (i) $\phi = 10°$ (black), (ii) $\phi = 30°$ (red/dark gray), (iii) $\phi = 50°$ (yellow/light gray).

increases with increasing r and reaches a maximum at $r = R$, as opposed to the similar distribution obtained by the phenomenological theory of ideal plasticity. This exhibits the isotropic hardening behavior due to the entanglement of dislocations. Fig. 3.24 presents the density of dislocations at the above three different twist angles. The density of dislocations is an increasing function of r and achieves the highest value at $r = R$.

Another interesting question is how strongly the twist rate and ambient temperature affect the torque-twist curve. Fig. 3.25 shows the three torque-twist curves for three samples loaded at the room temperature and at three different twist $\dot{\phi} = 0.25°/\text{s}$ (black), $\dot{\phi} = 2.5°/\text{s}$ (red/dark gray), and $\dot{\phi} = 25°/\text{s}$ (yellow/light gray). The radius of the samples is $R = 6.35$mm, while all other parameters remain unchanged. We see that the twist rate affects the strain hardening: the higher the twist rate, the higher the slope of the torque-twist curve. Fig. 3.26 shows the three torque-twist curves for three samples loaded at the same twist rate $\dot{\phi} = 0.25°/\text{s}$ but at three different ambient temperatures: $T = 25$°C (black), $T = 250$°C (red/dark gray), and $T = 500$°C (yellow/light gray). Thus, the higher the temperature, the lower the slope of the torque-twist curve and the smaller the hardening. As far as the size effect is concerned, we could not find reliable experimental data for single crystal copper under torsion at different bar radii, in contrast to twisted polycrystalline copper wires of different radii (cf.Liu, Zhang, Li, and Dunstan (2018)).

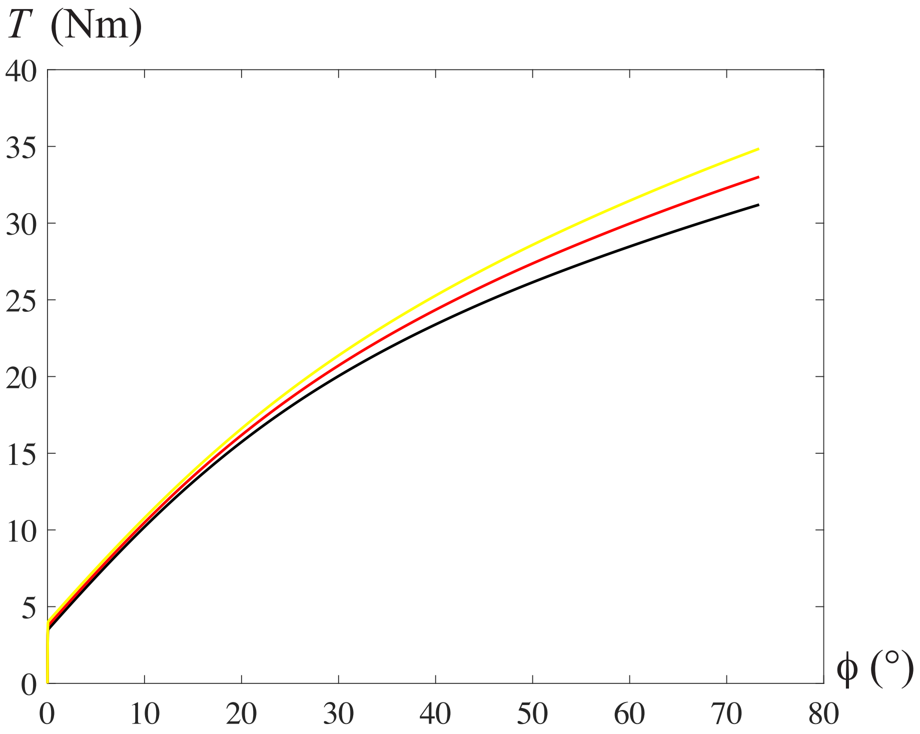

Figure 3.25: The torque-twist curves for the bars twisted at different twist rates and for room temperature: (i) $\dot{\phi} = 0.25^\circ/\mathrm{s}$ (black), (ii) $\dot{\phi} = 2.5^\circ/\mathrm{s}$ (red/dark gray), (iii) $\dot{\phi} = 25^\circ/\mathrm{s}$ (yellow/light gray).

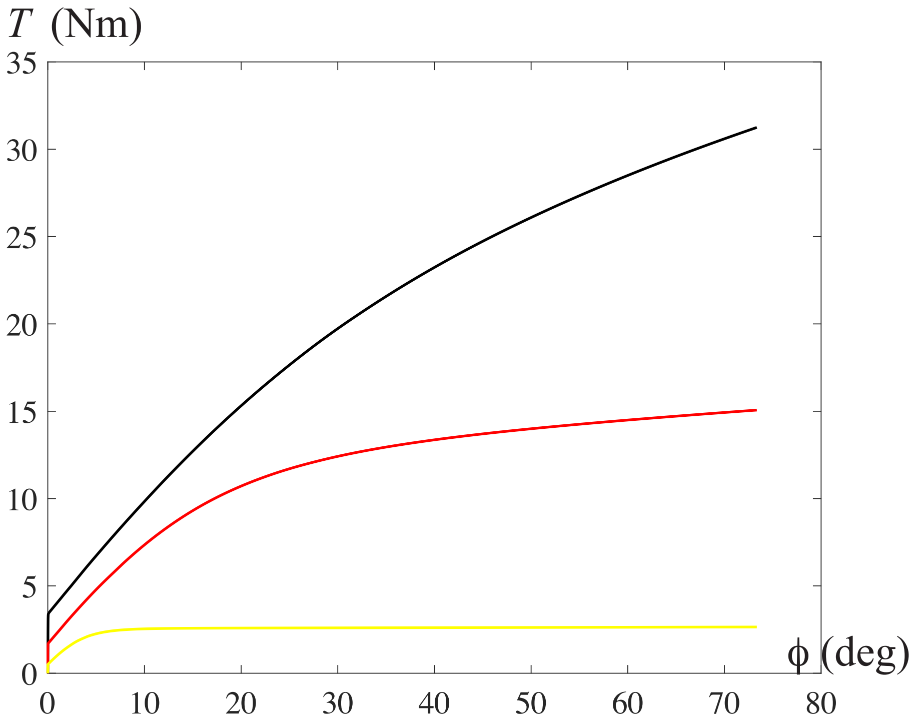

Figure 3.26: (Color online) The torque-twist curves for the bars twisted at the same twist rate $\dot{\phi} = 0.25^\circ/\mathrm{s}$ and for three different ambient temperatures: (i) $T = 25^\circ\mathrm{C}$ (black), (ii) $T = 250^\circ\mathrm{C}$ (red/dark gray), (iii) $T = 500^\circ\mathrm{C}$ (yellow/light gray).

4 Micro-indentation and anti-plane shear

In this chapter, the author introduces finite element simulations of the displacement controlled wedge indentation for single crystals within a simplified TDT (former name is Continuum Dislocation Theory) material model incorporating the density of excess dislocations. Under the assumption of plane strain deformation of the crystal having only one active slip system on each side of the wedge the load-displacement curve, as well as the excess dislocation density, are computed for the loading and unloading path in terms of the indentation depth. The results of numerical simulations are compared with those obtained from the experiments which show qualitative agreement.

Furthermore, the thermodynamic dislocation theory (TDT) developed for non-uniform plastic deformations is used here to simulate the stress-strain curves for crystals subjected to anti-plane shear-controlled load reversal. It is shown that the presence of the positive back stress during the load reversal reduces the magnitude of shear stress required to pull excess dislocations back to the center of the specimen. There, the excess dislocations of opposite signs meet and annihilate each other leading to the Bauschinger effect.

4.1 Dislocation structure during micro-indentation

4.1.1 Plane strain wedge indentation

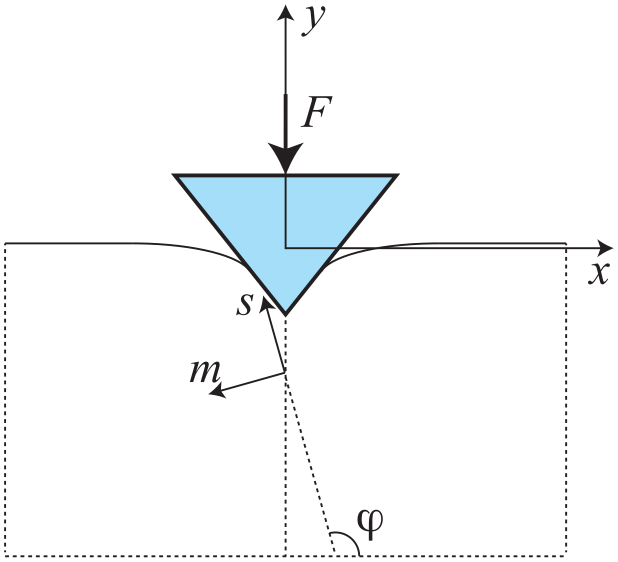

Figure 4.1: Wedge indentation.

Consider a single crystal subjected to indentation by a rigid cylindrical wedge (see Fig. 4.1). The depth of the crystal in the z-direction (which is equal to the length of the rigid indenter) is taken large enough to guarantee the plane strain state has two components of displacement $u_x = u(x,y)$ and $u_y = v(x,y)$. Besides, the sizes of the crystal's cross-section are much larger than those of the indenter so that the influence of the outer boundary can be neglected. If the crystal is oriented in such a way that its lattice and mechanical properties are symmetric with respect to the reflection about the y-axis, then it is sufficient to consider the left-half of the crystal, provided the indenter is also symmetric with respect to the y-axis. We assume that, during the plastic deformation of the crystal, only one slip system from each side of the wedge is active. Letting $s = (\cos\varphi, \sin\varphi)$ denote the slip direction, and $m = (-\sin\varphi, \cos\varphi)$ the normal vector to the slip plane, the plastic distortion tensor may be expressed in the form $\boldsymbol{\beta} = \beta(x,y)\mathbf{s}\otimes\mathbf{m}$. Regarding the vertical displacement of the indenter $-h$ as the control parameter in our problem, we are going to determine the displacements $u(x,y)$, $v(x,y)$, and the plastic slip $\beta(x,y)$ in terms of the indentation depth h. For the plane strain state the in-plane components of the symmetric strain tensor $\boldsymbol{\varepsilon} = \frac{1}{2}(\nabla\mathbf{u} + \mathbf{u}\nabla)$ are

$$\varepsilon_{xx} = u_{,x}, \quad \varepsilon_{xy} = \frac{1}{2}(u_{,y} + v_{,x}), \quad \varepsilon_{yy} = v_{,y}.$$

Throughout this section, the comma standing before an index is used to denote the partial derivative with respect to the corresponding coordinate. The in-plane components of the symmetric plastic strain tensor $\boldsymbol{\varepsilon}^p = \frac{1}{2}(\boldsymbol{\beta} + \boldsymbol{\beta}^T)$ equal

$$\varepsilon^p_{xx} = -\frac{1}{2}\beta\sin 2\varphi, \quad \varepsilon^p_{xy} = \frac{1}{2}\beta\cos 2\varphi, \quad \varepsilon^p_{yy} = \frac{1}{2}\beta\sin 2\varphi.$$

With these total and plastic strain tensors, we obtain the in-plane components of the symmetric elastic strain tensor $\boldsymbol{\varepsilon}^e = \boldsymbol{\varepsilon} - \boldsymbol{\varepsilon}^p$ in the form

$$\varepsilon^e_{xx} = u_{,x} + \frac{1}{2}\beta\sin 2\varphi,\ \varepsilon^e_{xy} = \frac{1}{2}(u_{,y} + v_{,x} - \beta\cos 2\varphi),\ \varepsilon^e_{yy} = v_{,y} - \frac{1}{2}\beta\sin 2\varphi. \quad (4.1)$$

Let us compute Nye-Bilby-Kröner's dislocation density tensor $\boldsymbol{\alpha} = -\boldsymbol{\beta}\times\nabla$, with $\times$ being the vector product (Bilby (1955); Kröner (1955); Nye (1953)). For plane strain plastic distortion there are two non-zero components of this tensor given by

$$\alpha_{xz} = (\beta_{,x}\cos\varphi + \beta_{,y}\sin\varphi)\cos\varphi, \quad \alpha_{yz} = (\beta_{,x}\cos\varphi + \beta_{,y}\sin\varphi)\sin\varphi.$$

These are the component of the net Burgers' vector of all excess dislocations whose dislocation lines cut the area perpendicular to the z-axis. Thus, the net Burgers' vector of excess dislocations shows in the slip direction s and the scalar dislocation density equals

$$\rho = \frac{1}{b}\sqrt{\alpha^2_{xz} + \alpha^2_{yz}} = \frac{1}{b}|\beta_{,x}\cos\varphi + \beta_{,y}\sin\varphi| = \frac{1}{b}\nabla\beta\cdot\mathrm{s}. \quad (4.2)$$

Since the lattice rotation can directly be measured by the Electron Back Scatter Diffraction (EBSD) technique, it is interesting to express it in terms of the displacement gradient and plastic slip. Using the additive decomposition for the displacement gradients $\boldsymbol{u}\nabla = \boldsymbol{\varepsilon} + \boldsymbol{\omega}$, we find the components of the total rotation tensor in the form

$$\omega_{ij} = \frac{1}{2}(u_{i,j} - u_{j,i}).$$

This tensor is obviously skew-symmetric. The plastic rotation tensor is the skew-symmetric part of the plastic distortion

$$\omega^p_{ij} = \frac{1}{2}(\beta_{ij} - \beta_{ji}) = \frac{1}{2}\beta(s_i m_j - s_j m_i).$$

The elastic (lattice) rotation tensor is the difference between these two tensors

$$\omega^e_{ij} = \omega_{ij} - \omega^p_{ij} = \frac{1}{2}(u_{i,j} - u_{j,i}) - \frac{1}{2}\beta(s_i m_j - s_j m_i).$$

Since all these rotation tensors are skew-symmetric, they can be associated with the axial vectors called rotation vectors. In our two-dimensional case only the z-components of these vectors are non-zero, so, from the above formulas the lattice rotation is obtained in the form

$$w^e_z = -\omega^e_{xy} = \omega^e_{yx} = \frac{1}{2}(v_{,x} - u, y) + \frac{1}{2}\beta. \tag{4.3}$$

For most metals, the elastic strain tensor ε^e is usually small. Therefore the free energy density per unit volume of the crystal with continuously distributed dislocations can be proposed in the form (Berdichevsky (2006a, 2006b))

$$\psi(\varepsilon^e, \rho) = \frac{1}{2}\lambda(\mathrm{tr}\varepsilon^e)^2 + \mu\varepsilon^e{:}\varepsilon^e + \mu k \ln\frac{1}{1 - \frac{\rho}{\rho_s}}, \tag{4.4}$$

with λ and μ being the Lamé constants, ρ_s the saturated dislocation density, and k the material constant. The first two terms in Eq. (4.4) represents the contribution to the energy coming from the elastic strain, while the last term corresponds to the energy of the dislocation network. The logarithmic energy term stems from two facts: i) energy of the dislocation network for small dislocation densities is the sum of energy of non-interacting dislocations (see the reasonings based on the statistical mechanics of dislocations in (Le (2010); Le and Berdichevsky (2001)), and ii) there exists a saturated dislocation density which characterizes the closest packing of dislocations admissible in the discrete crystal lattice. The logarithmic term (Berdichevsky (2006b)) ensures a linear increase of the energy for small dislocation density ρ and tends to infinity as ρ approaches the saturated dislocation density ρ_s hence providing an energetic barrier against over-saturation. This energy density form is schematically depicted in Fig. 4.2.

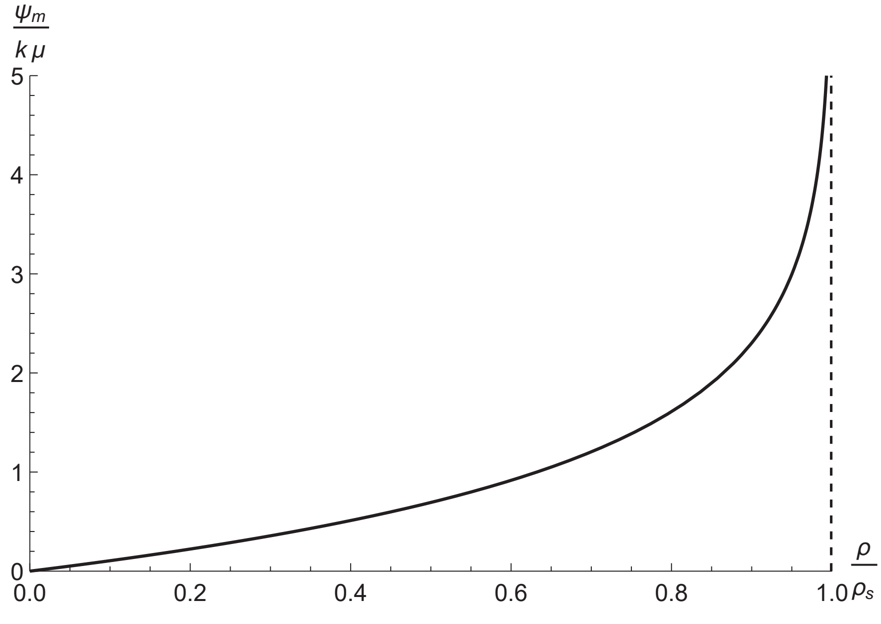

Figure 4.2: Energy density of dislocation network.

With Eq. (4.1, 4.2, and 4.4), the bulk energy density per unit volume of the crystal with continuously distributed dislocations in our plane strain case reads

$$\psi(\boldsymbol{\varepsilon}^e,\rho)=\frac{1}{2}\lambda(u_{,x}+v_{,y})^2+\mu(u_{,x}+\frac{1}{2}\beta\sin 2\varphi)^2+\mu(v_{,y}-\frac{1}{2}\beta\sin 2\varphi)^2 \\ +\frac{1}{2}\mu(u_{,y}+v_{,x}-\beta\cos 2\varphi)^2+\mu k\ln\frac{1}{1-\frac{\rho}{\rho_s}}, \quad (4.5)$$

and the total energy functional per unit depth becomes

$$I[u,v,\beta]=\int_\Omega\Big[\frac{1}{2}\lambda(u_{,x}+v_{,y})^2+\mu(u_{,x}+\frac{1}{2}\beta\sin 2\varphi)^2+\mu(v_{,y}-\frac{1}{2}\beta\sin 2\varphi)^2 \\ +\frac{1}{2}\mu(u_{,y}+v_{,x}-\beta\cos 2\varphi)^2+\mu k\ln\frac{1}{1-\frac{\rho}{\rho_s}}\Big]\,dxdy, \quad (4.6)$$

where $\Omega=(-L,0)\times(-H,0)$ is the domain occupied by the left-half of the undeformed crystal.

Since the material points of the crystal cannot penetrate the rigid indenter, its deformed upper boundary must lie below the lower boundary of the indenter. Let the lower boundary of the indenter be described by the set of points $(x,w_0(x))$ in the (x,y)-coordinate system, where $w_0(x)$ is a smooth function. We shall assume that the material points of the crystal, once in contact, stick to the contact area of the indenter and no sliding occurs. Since the displacements in the contact zone are smooth, dislocations cannot reach this part of the boundary, so the plastic slip must vanish there. Because the remaining part of the upper boundary is free, no kinematic constraints apply to u,v and β so that they can be varied arbitrarily. Along the y-axis which is the anti-symmetry axis the displacement u mush vanish. Because of this, the plastic slip must vanish too. On the left (and at the lower) boundary which are far away from the indenter, we may pose the boundary conditions of vanishing horizontal (respectively vertical) displacement and plastic slip. In this contact problem, it is convenient to present the above-formulated constraints in the incremental form. Consider the time-discretization $0=t_0<t_1<\ldots<t_n=T$ and assume that the solution $(u_{j-1},v_{j-1},\beta_{j-1})$ as well as the length l_{j-1} of the contact zone are known at the time instant t_{j-1} corresponding to the indentation depth h_{j-1} (in this rate-independent quasi-static loading process the time instants and the time increment represent the indentation depths and the indentation depth increment). We want to find the solution (u_j,v_j,β_j) and l_j at t_j at which the indentation depth is h_j. Due to the non-sliding boundary condition on the contact area we set

$$u_j(x,0)=u_{j-1}(x,0),\quad v_j(x,0)=w_0(x)-h_j,\quad \beta_j(x,0)=0 \quad (4.7)$$

for $x\in(-l_j,0)$, and $w_0(x)=-\cot\frac{\alpha}{2}x$ with α being the angle of the indenter. It is seen from Eq. $(4.7)_2$ that the vertical displacement of the material points underneath the indenter is equal to the given vertical displacement of the indenter. For the remaining part of the upper boundary $x\in(-L,-l_j)$ no kinematic constraints apply to u_j,v_j,β_j. Along the y-axis, due to the mirror symmetry, the boundary conditions are posed

$$u_j(x,y)=0,\quad v_j(x,y)=0,\quad \beta(x,y)=0\quad \text{for}\ y\in(-H,0), \quad (4.8)$$

but $v_j(0,y)$ may be varied arbitrarily. Finally, on the left and the lower boundaries which are far away from the indenter we may pose the boundary conditions

$$u_j(-L,y)=0,\quad \beta_j(-L,y)=0,\quad v_j(x,-H)=0,\quad \beta_j(x,-H)=0. \quad (4.9)$$

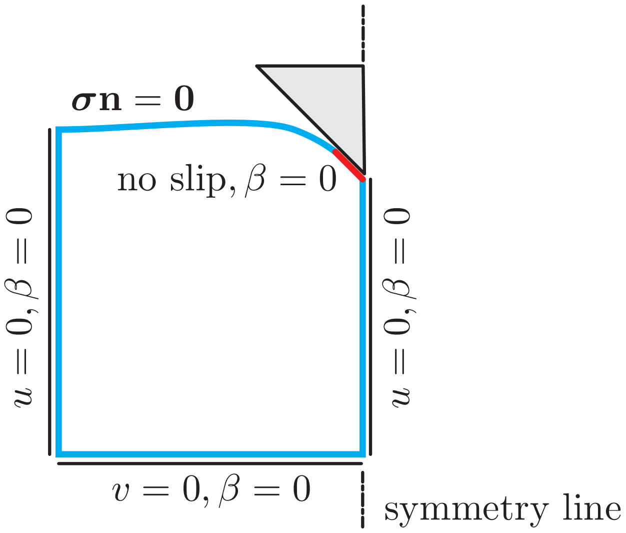

Figure 4.3: Boundary conditions for symmetric left-half.

The crystal is loaded so slowly that the inertia can be neglected and at each small indentation depth increment the final equilibrium state can be established (quasi-static loading process). Fig. 4.3 schematically shows a visualization of boundary conditions mentioned above.

By the final state of indentation we mean the equilibrium state which is established at fixed loading condition after dislocation nucleation and after the movement of dislocations toward their equilibrium positions is finished. If the dissipation caused by the dislocation motion is negligible, then the true displacements $u_j(x,y), v_j(x,y)$ and plastic slip $\beta_j(x,y)$ in the final state of indentation minimize energy functional Eq. (4.6) among all admissible displacements and plastic slips satisfying the boundary conditions (4.7)-(4.9).

In case the dissipation due to the dislocation motion cannot be neglected, the energy minimization should be replaced by the variational equation (Sedov (1968))

$$\delta I + \int_{\Omega} \frac{\partial D}{\partial \dot{\beta}} \delta\beta \, dxdy = 0. \tag{4.10}$$

The last term in this equation describes the energy dissipation due to the dislocation motion, where the dissipation function $D(\dot{\beta})$ is assumed to depend only on the rate of the plastic distortion. The simplest rate-independent theory is considered for which

$$D(\dot{\beta}) = K|\dot{\beta}|,$$

with K the critical resolved shear stress.

4.1.2 Finite element formulation at Zero Dissipation

Let us now discretize the above two-dimensional variational problems by the finite element method. For this purpose, it is convenient to reformulate them using Voigt's notation. We let $\mathbf{w}$ denote function of the generalized displacement vector

$$\mathbf{w} = (u, v, \beta)^T.$$

Furthermore, we introduce the total strain vector

$$\boldsymbol{\varepsilon} = (u_{,x}, v_{,y}, u_{,y} + v_{,x})^T,$$

and the plastic strain vector

$$\boldsymbol{\varepsilon}^p = (-\frac{1}{2}\beta\sin 2\varphi, \frac{1}{2}\beta\sin 2\varphi, \beta\cos 2\varphi)^T,$$

such that the elastic strain vector is $\boldsymbol{\varepsilon}^e = \boldsymbol{\varepsilon} - \boldsymbol{\varepsilon}^p$. Inserting the elastic strain vector $\boldsymbol{\varepsilon}^e$, the free energy density (4.5) in Voigt's notation is now presented as

$$\psi(\boldsymbol{\varepsilon}^e, \rho) = \frac{1}{2}\left(\boldsymbol{\varepsilon}^e\right)^T \mathbf{E}\boldsymbol{\varepsilon}^e + \psi_m(\rho) \tag{4.11}$$

with the plane strain elasticity matrix

$$\mathbf{E} = \begin{pmatrix} \lambda + 2\mu & \lambda & 0 \\ \lambda & \lambda + 2\mu & 0 \\ 0 & 0 & \mu \end{pmatrix}.$$

In order to express the free energy density (4.11) in terms of the displacement function $\mathbf{w}$, the matrix differential operator

$$\mathbf{D}^\varepsilon = \begin{pmatrix} \partial_x & 0 & \frac{1}{2}\sin 2\varphi \\ 0 & \partial_y & -\frac{1}{2}\sin 2\varphi \\ \partial_y & \partial_x & -\cos 2\varphi \end{pmatrix}$$

is introduced such that $\boldsymbol{\varepsilon}^e = \mathbf{D}^\varepsilon \mathbf{w}$. By an additional differential operator

$$\mathbf{D}^\rho = (0, 0, \cos\varphi\,\partial_x + \sin\varphi\,\partial_y)$$

the scalar dislocation density (4.2) is expressed in terms of $\mathbf{w}$ as

$$\rho = \frac{1}{b}|\beta_{,x}\cos\varphi + \beta_{,y}\sin\varphi| = \frac{1}{b}|\mathbf{D}^\rho\mathbf{w}|.$$

Thus, the energy density of dislocation network can be defined as function

$$\tilde{\psi}_m(\mathbf{D}^\rho\mathbf{w}) = \mu\, k \ln \frac{1}{1 - \frac{1}{\rho_s b}|\mathbf{D}^\rho\mathbf{w}|}.$$

such that (4.11) finally becomes

$$\psi(\mathbf{w}) = \frac{1}{2}\left(\mathbf{D}^\varepsilon\mathbf{w}\right)^T \mathbf{E}\,\mathbf{D}^\varepsilon\mathbf{w} + \tilde{\psi}_m(\mathbf{D}^\rho\mathbf{w}).$$

Now we can rewrite the functional (4.6) in terms of the generalized displacement as

$$I[\mathbf{w}_j] = \int_\Omega \left[\frac{1}{2}(\mathbf{D}^\varepsilon\mathbf{w}_j)^T\mathbf{E}(\mathbf{D}^\varepsilon\mathbf{w}_j) + \tilde{\psi}_m(\mathbf{D}^\rho\mathbf{w}_j)\right] dxdy \tag{4.12}$$

The necessary condition for (4.12) to achieve a (local) minimum is that the variation

$$\delta I[\mathbf{w}, \delta\mathbf{w}] = \int_\Omega \left[(\mathbf{D}^\varepsilon\mathbf{w})^T\mathbf{E}(\mathbf{D}^\varepsilon\delta\mathbf{w}) + \tilde{\psi}_m'(\mathbf{D}^\rho\mathbf{w})\mathbf{D}^\rho\delta\mathbf{w}\right] dxdy \tag{4.13}$$

vanishes for all admissible test functions $\delta\mathbf{w} = (\delta u, \delta v, \delta\beta)^T$. Furthermore, we need the linearization

$$D\delta I[\mathbf{w}, \delta\mathbf{w}, \Delta\mathbf{w}] = \int_\Omega \left[(\mathbf{D}^\varepsilon\Delta\mathbf{w})^T\mathbf{E}(\mathbf{D}^\varepsilon\delta\mathbf{w}) + \tilde{\psi}_m''(\mathbf{D}^\rho\mathbf{w}_j)\,\mathbf{D}^\rho\Delta\mathbf{w}\,\mathbf{D}^\rho\delta\mathbf{w}\right] dxdy \tag{4.14}$$

of (4.13) in direction $\Delta\mathbf{w} = (\Delta u, \Delta v, \Delta\beta)^T$ in order to set up the tangential stiffness matrix in the Newton-Raphson solution procedure (see, e.g., (Holzapfel, 2000)).

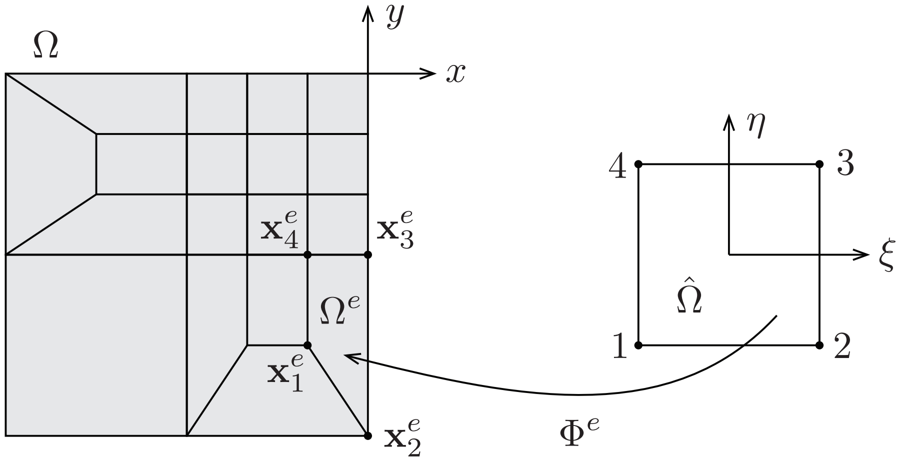

Figure 4.4: Discretization of the domain Ω into bilinear isoparametric elements Ω^e, $e = 1, \ldots, n_e$. Each element Ω^e is obtained by the mapping (4.15) from the square $\hat{\Omega} = (-1, 1) \times (-1, 1)$ in the (ξ, η)-plane, with counterclockwise node numbering.

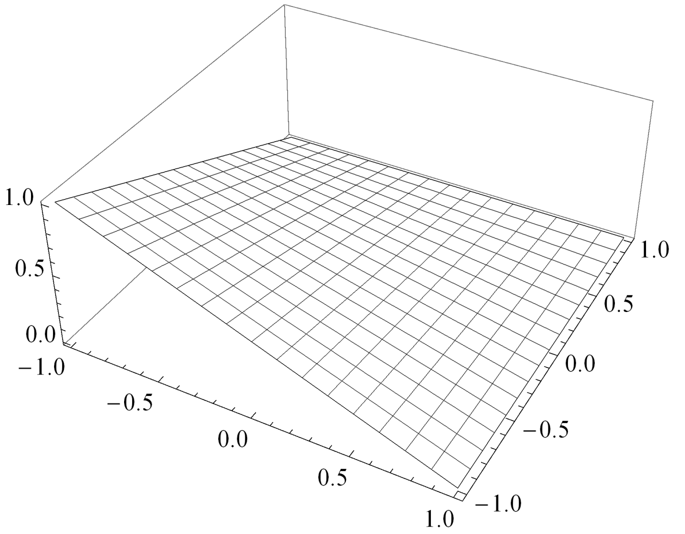

Figure 4.5: Example of bilinear shape functions in reference space $\hat{\Omega}$.

Finite element discretization Let Ω be now subdivided into a finite number n_e of bilinear isoparametric quadrilateral elements Ω^e ($e = 1, \ldots, n_e$) as shown schematically in Fig. 4.4. Each element Ω^e can be obtained from a square $\hat{\Omega} = (-1, 1) \times (-1, 1)$ in the (ξ, η)-plane by the mapping

$$\mathbf{x} = \Phi^e(\xi, \eta) = \sum_{i=1}^{4} N_i(\xi, \eta)\, \mathbf{x}_i^e, \tag{4.15}$$

where $\mathbf{x}_i^e = (x_i^e, y_i^e)^T$ are coordinates of node i and $N_i(\xi, \eta)$ the shape functions.

$$N_1(\xi, \eta) = \frac{1}{4}(1 - \xi)(1 - \eta), \qquad N_2(\xi, \eta) = \frac{1}{4}(1 + \xi)(1 - \eta),$$
$$N_3(\xi, \eta) = \frac{1}{4}(1 + \xi)(1 + \eta), \qquad N_4(\xi, \eta) = \frac{1}{4}(1 - \xi)(1 + \eta).$$

Following the iso-parametric concept, we use the same shape functions in order to approximate the displacements u, v, and the plastic slip β on each element e as

$$\mathbf{w}_h^e = (u_h^e, v_h^e, \beta_h^e)^T = \sum_{i=1}^{12} \mathbf{N}_i \hat{u}_i^e = \mathbf{N}\hat{\mathbf{u}}^e, \tag{4.16}$$

with the vector valued shape functions

$$\mathbf{N}_i(\xi,\eta) = N_j(\xi,\eta)\mathbf{e}_k, \quad i = 3(j-1)+k, \quad j = 1,\dots,4, \quad k = 1,\dots,3$$

forming the columns of the shape function matrix $\mathbf{N}$ and the coefficient vector

$$\hat{\mathbf{u}}^e = (\hat{u}_1^e, \hat{v}_1^e, \hat{\beta}_1^e, \hat{u}_2^e, \hat{v}_2^e, \hat{\beta}_2^e, \hat{u}_3^e, \hat{v}_3^e, \hat{\beta}_3^e, \hat{u}_4^e, \hat{v}_4^e, \hat{\beta}_4^e)^T.$$

Eqs. (4.15) and (4.16) in conjunction with the nodal shape functions ensure that $(x,y) = (x_i^e, y_i^e)$ and $\mathbf{w}_h^e = (\hat{u}_i^e, \hat{v}_i^e, \hat{\beta}_i^e)$ at each node since the shape function N_i equals 1 at node i and zero at all other nodes (see Fig. 4.5). Thus, the displacements and the plastic slip are equal to their respective nodal values as required.

The current configuration of a bilinear element is isoparametrically mapped from the physical space onto the square element; there is a discrepancy between the actual position of points of the element in the physical space and of those in the mapped square element. Due to this mapping in (4.15), the spatial derivatives of displacements and plastic slip with respect to x, y have to be transformed to the derivatives with respect to ξ, η using the Jacobian matrix

$$\mathbf{J}^e = \begin{pmatrix} x_{,\xi} & x_{,\eta} \\ y_{,\xi} & y_{,\eta} \end{pmatrix} = \frac{1}{4}\begin{pmatrix} x_1^e & x_2^e & x_3^e & x_4^e \\ y_1^e & y_2^e & y_3^e & y_4^e \end{pmatrix} \begin{pmatrix} -(1-\eta) & -(1-\xi) \\ (1-\eta) & -(1+\xi) \\ (1+\eta) & (1+\xi) \\ -(1+\eta) & (1-\xi) \end{pmatrix}.$$

We denote the determinant of the Jacobian matrix by J^e and define the spatial derivatives

$$\nabla_x N_i = \begin{pmatrix} N_{i,x} \\ N_{i,y} \end{pmatrix} = (\mathbf{J}^e)^{-T} \begin{pmatrix} N_{i,\xi} \\ N_{i,\eta} \end{pmatrix}$$

in terms of the local coordinates ξ, η.

In order to obtain the vector of internal forces, which is the basis for the Newton-Raphson solution procedure, we insert the discretized virtual displacements $\delta\mathbf{w}_h^e = \mathbf{N}\delta\hat{\mathbf{u}}^e$ in the variation of the energy functional (4.13) and integrate element-wise to obtain

$$\begin{aligned} \delta I(\hat{\mathbf{u}}^e, \delta\hat{\mathbf{u}}^e) &= \sum_{e=1}^{n_e} (\delta\hat{\mathbf{u}}^e)^T \int_{\hat{\Omega}^e} \left[\mathbf{B}^T\mathbf{E}\mathbf{B}\hat{\mathbf{u}}^e + \tilde{\psi}_m'(\mathbf{Q}\hat{\mathbf{u}}^e)\mathbf{Q}^T\right] J^e d\xi d\eta \\ &= \sum_{e=1}^{n_e} (\delta\hat{\mathbf{u}}^e)^T \mathbf{f}_{\text{int}}^e(\hat{\mathbf{u}}^e), \end{aligned}$$

where $\mathbf{f}^e_{\text{int}}(\hat{\mathbf{u}}^e)$ is the internal force vector of element e and

$$\begin{aligned}
\mathbf{B} &= \mathbf{D}^{\varepsilon}\mathbf{N}\\
&= \left(\begin{matrix} N_{1,x} & 0 & s_2/2\,N_1 & N_{2,x} & 0 & s_2/2\,N_2 \\ 0 & N_{1,y} & -s_2/2\,N_1 & 0 & N_{2,y} & -s_2/2\,N_2 \\ N_{1,y} & N_{1,x} & -c_2\,N_1 & N_{2,y} & N_{2,x} & -c_2\,N_2 \end{matrix}\right.\\
&\qquad\qquad \left.\begin{matrix} N_{3,x} & 0 & s_2/2\,N_3 & N_{4,x} & 0 & s_2/2\,N_4 \\ 0 & N_{3,y} & -s_2/2\,N_3 & 0 & N_{4,y} & -s_2/2\,N_4 \\ N_{3,y} & N_{3,x} & -c_2\,N_3 & N_{4,y} & N_{4,x} & -c_2\,N_4 \end{matrix}\right),\\
\mathbf{Q} &= \mathbf{D}^{\rho}\mathbf{N}\\
&= \big(0, 0, cN_{1,x} + sN_{1,y}, 0, 0, cN_{2,x} + sN_{2,y},\\
&\qquad\qquad 0, 0, cN_{3,x} + sN_{3,y}, 0, 0, cN_{4,x} + sN_{4,y}\big)\,.
\end{aligned}$$

Note that we used the shorthand forms $s = \sin\varphi, c = \cos\varphi, s_2 = \sin 2\varphi$ and $c_2 = \cos 2\varphi$. Finally, we plug the discretized displacement increment $\Delta\mathbf{w}^e_h = \mathbf{N}\Delta\hat{\mathbf{u}}^e$ into the linearized variation of the internal energy (4.14) and find

$$\begin{aligned}
D\delta I(\mathbf{u}^e, \delta\mathbf{u}^e, \Delta\mathbf{u}^e) &= \sum_{e=1}^{n_e}(\delta\hat{\mathbf{u}}^e)^T \int_{\hat{\Omega}^e}\Big[\mathbf{B}^T\mathbf{E}\mathbf{B} + \tilde{\psi}''_m(\mathbf{Q}\hat{\mathbf{u}}^e)\mathbf{Q}^T\mathbf{Q}\Big]\, J^e d\xi d\eta\, \Delta\hat{\mathbf{u}}^e\\
&= (\delta\hat{\mathbf{u}}^e)^T\mathbf{K}^e_{\text{int}}(\hat{\mathbf{u}}^e)\Delta\hat{\mathbf{u}}^e,
\end{aligned}$$

with the element tangent stiffness matrix $\mathbf{K}^e_{\text{int}}(\hat{\mathbf{u}}^e)$.

Contact formulation The boundary conditions (4.7) stemming from the rigid indenter are incorporated into the numerical model by a node-to-rigid-surface contact formulation. The domain of the indenter is implicitly represented by the set of points

$$\{(x, y) \in \mathbb{R}^2 \mid g(x, y) < 0\}$$

where g is a function $\mathbb{R}^2 \to \mathbb{R}$. For example, in the case of rounding wedge-shaped indenter, we take

$$g(x, y) = \begin{cases} -\big(x\cos\frac{\alpha}{2} + (y + h - r)\sin\frac{\alpha}{2}\big)^{\frac{1}{2m}} - r^{\frac{1}{2m}} & \text{if } s \geq 0 \\ (x^2 + (y + h - r)^2)^{\frac{1}{4m}} - r^{\frac{1}{2m}} & \text{if } s < 0 \end{cases}$$

with parameter m being chosen incrementally from $1, 2, 3, ...$, and selection criterion $s = -x\sin\frac{\alpha}{2} + (y + h - r)\cos\frac{\alpha}{2}$. Parameter m is introduced to make the finite element code robust with respect to the change of geometry of the indenter. Note that function $g(x, y)$ also depends on the indentation depth h. Correspondingly, we replace the boundary condition $(4.7)_2$ by the requirement that $g(x^n + u^n, y^n + v^n) \geq 0$ which has the advantage that we do not have to compute the *a priori* unknown length of the contact zone. Following the classical approach from contact mechanics (Wriggers & Zavarise, 2004), we introduce nodal Lagrange multipliers $\lambda^n_x, \lambda^n_n, \lambda^n_\beta$ for the x-direction, the normal-direction, and β respectively. All nodal unknowns are collected in a vector $\mathbf{w}^n = (u^n_j, v^n_j, \beta^n_j, \lambda^n_x, \lambda^n_n, \lambda^n_\beta)^T$. Then, at time instant t_j, the contribution of node n to the contact energy I_c becomes

$$I^n_c(\mathbf{w}^n_j) = \lambda^n_{x,j}\cdot(u^n_j - u^n_{j-1}) + \lambda^n_{n,j}\cdot g(x^n + u^n_j, y^n + v^n_j) + \lambda^n_{\beta,j}\cdot\beta^n_j \qquad (4.17)$$

where x^n, y^n is the position of node n and $u_j^n = u_j(x^n, y^n), v_j^n = v_j(x^n, y^n)$ and $\beta_j^n = \beta_j(x^n, y^n)$. Furthermore, we employ the conditions $g(x^n + u_j^n, y^n + v_j^n) \leq 0$ and $\lambda_{n,j} \leq 0$ in order to identify the set of nodes with active contact constraints.

Since the contact energy contribution I_c^n is already defined in terms of discrete nodal variables, the nodal contact force vector

$$\mathbf{f}_{\text{con}}^n(\mathbf{w}_j^n) = \begin{pmatrix} \lambda_x^n + \lambda_n^n \cdot g_{,x} \\ \lambda_n^n \cdot g_{,y} \\ \lambda_\beta^n \\ u_j^n - u_{j-1}^n \\ g \\ \beta^n \end{pmatrix}$$

and the nodal tangent stiffness matrix

$$\mathbf{K}_{\text{con}}^n(\mathbf{w}_j^n) = \begin{pmatrix} g_{,xx} \cdot \lambda_n^n & g_{,xy} \cdot \lambda_n^n & 0 & 1 & g_{,x} & 0 \\ g_{,yx} \cdot \lambda_n^n & g_{,yy} \cdot \lambda_n^n & 0 & 0 & g_{,y} & 0 \\ 0 & 0 & 0 & 0 & 0 & 1 \\ 1 & 0 & 0 & 0 & 0 & 0 \\ g_{,x} & g_{,y} & 0 & 0 & 0 & 0 \\ 0 & 0 & 1 & 0 & 0 & 0 \end{pmatrix}$$

are easily obtained as the gradient and the Jacobian of (4.17). Note that g in these formulas refers to $g(x^n + u_j^n, y^n + v_j^n)$.

4.1.3 Newton-Raphson solution procedure

Using an assembly operator $\mathcal{A}$, we obtain the global force vector

$$\mathbf{f}(\hat{\mathbf{u}}) = \mathop{\mathcal{A}}_{e=1}^{n_e} (\mathbf{f}_{\text{int}}^e(\hat{\mathbf{u}}^e)) + \mathop{\mathcal{A}}_{n=1}^{n_c} (\mathbf{f}_{\text{con}}^n(\hat{\mathbf{u}}^n))$$

from the element internal force vectors and the nodal contact forces. Since no external forces are acting on the specimen, the discrete stationarity condition is

$$\mathbf{f}(\hat{\mathbf{u}}) = \mathbf{0},$$

where the global vector of internal and contact forces $\mathbf{f}$ is a nonlinear function $\mathbb{R}^{n_u} \to \mathbb{R}^{n_u}$ of the n_u unknown nodal values. Similarly, the global stiffness matrix

$$\mathbf{K}(\hat{\mathbf{u}}) = \mathop{\mathcal{A}}_{e=1}^{n_e} (\mathbf{K}_{\text{int}}^e(\hat{\mathbf{u}}^e)) + \mathop{\mathcal{A}}_{n=1}^{n_c} (\mathbf{K}_{\text{con}}^n(\hat{\mathbf{u}}^n))$$

consists of the element and contact contributions.

Convergence rate and stability of the Newton-Raphson solution procedure depend on the properties of the function $\mathbf{f}$. In our case, we have to consider strong nonlinearities and the possibility of arithmetic exceptions. For these reasons, we employ a Newton-Raphson iteration scheme with linesearch. The update of the current solution vector $\hat{\mathbf{u}}_n$ is

$$\hat{\mathbf{u}}_{n+1} = \hat{\mathbf{u}}_n + \alpha \mathbf{d}_n$$

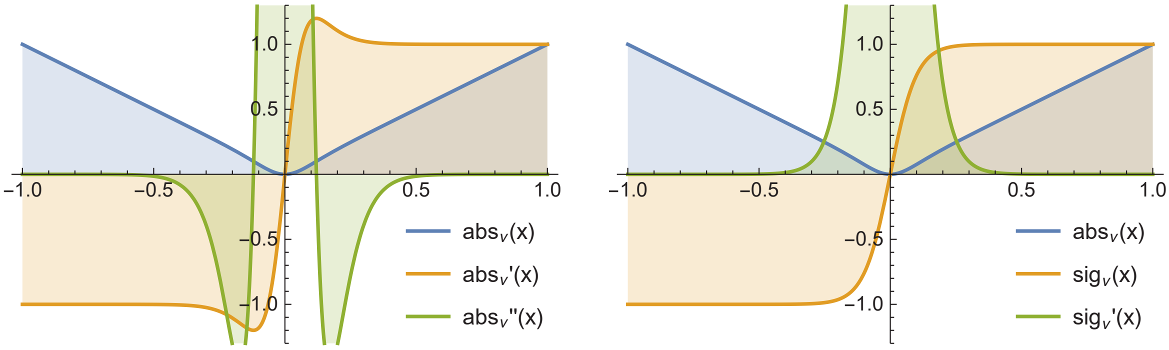

Figure 4.6: Smooth approximations of $|x|$ and its derivatives for $\nu = 20$. It can be seen that the consistent derivative in (4.19) on the left hand side has a bump close to $x = 0$ while the relaxed approximation of the derivative in (4.20) on the right hand side does not expose this behaviour. Furthermore, the second derivative of the relaxed formulation is strictly positive.

where the search direction in step n is

$$\mathbf{d}_n = -\mathbf{K}^{-1}(\hat{\mathbf{u}}_n)\mathbf{f}(\hat{\mathbf{u}}_n),$$

and the step-width α is obtained by minimizing the norm of the internal force vector such that

$$\alpha = \underset{\alpha > 0}{\operatorname{argmin}} \, |\mathbf{f}(\hat{\mathbf{u}}_n + \alpha \mathbf{d}_n)|. \tag{4.18}$$

Other linesearch criteria (e.g. the system energy, see De Borst et al. (2012)) for this one-dimensional minimization problem are discussed in the literature, but for the problem at hand, the norm of the residual turns out to be favorable. Problem (4.18) is solved using Brent's algorithm (Brent, 2013).

Modification of energy of dislocation network In order to mitigate numerical problems associated with the non-smooth abs function in the formulation of the dislocation density (4.2), we approximate the sign function by the smooth sigmoid function sig_ν (see (Kochmann, 2009))

$$\mathrm{sign}(x) \cong \mathrm{sig}_\nu(x) = \frac{2}{1 + e^{-\nu x}} - 1,$$

with the approximation parameter $\nu \in \mathbb{R}^+$ which has to be chosen sufficiently large. Using sig_ν, we obtain

$$|x| \cong \mathrm{abs}_\nu(x) = x \cdot \mathrm{sig}_\nu(x) \quad \text{and} \quad \frac{\mathrm{d}}{\mathrm{d}x}|x| \cong \mathrm{abs}'_\nu(x) = \mathrm{sig}_\nu(x) + x \cdot \mathrm{sig}'_\nu(x) \tag{4.19}$$

as consistent smooth approximation to the absolute value of x and the corresponding derivative. As an alternative to (4.19), it is possible to insert

$$|x| \cong \mathrm{abs}_\nu(x) = x \cdot \mathrm{sig}_\nu(x) \quad \text{and} \quad \frac{\mathrm{d}}{\mathrm{d}x}|x| = \mathrm{sgn}(x) \cong \mathrm{sig}_\nu(x), \tag{4.20}$$

where the exact derivative of the absolute value is approximated by a smooth function (instead of computing the derivative of the approximated absolute value). Although the relaxed

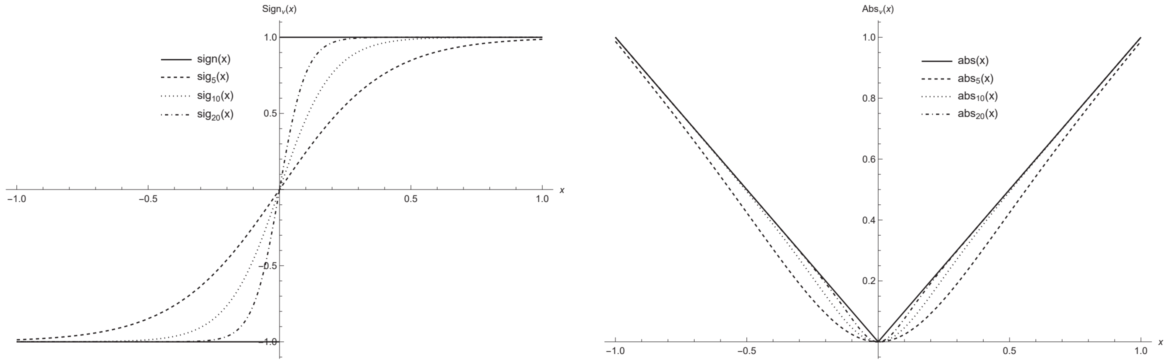

(a) Sign function.

(b) Absolute function.

Figure 4.7: Quality of the approximate function for sign and absolute value functions with different ν.

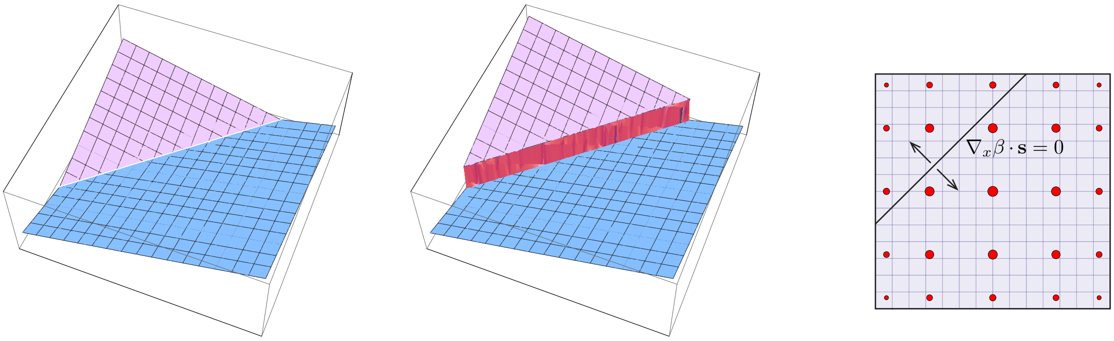

(a) Dislocation energy.

(b) Internal force vector.

(c) Quadrature points.

Figure 4.8: Integrands for energy and the element internal force vector.

formulation (4.20) is not consistent with the derivatives of the energy density of dislocation network, it turned out to be numerically more stable. The comparison in Figure 4.6 shows the functions for both approaches while Fig. 4.7 presents how precise the relaxed formulation may obtain by increasing ν. Numerical results presented in Subsection 4.1.4 are obtained with $\nu = 10^3$ and the relaxed approximation.

The energy of dislocation network $\psi_m = k\mu \ln \frac{1}{1-\rho/\rho_s}$ used in the linear CDT is well suited for analytical considerations but, since it is undefined for $\rho > \rho_s$, potentially dangerous in a numerical setting. Therefore, we choose the alternative energy density (Kochmann, 2009)

$$\tilde{\Psi}_m(\rho) = k\mu \left[\sum_{i=1}^{n} \frac{1}{i} \left(\frac{\rho}{\rho_s} \right)^i + e^{c(\rho/\chi\rho_s - 1)} - e^{-c} \right]$$

which is very close to the original density for small values of ρ while being well-defined for any $\rho \in \mathbb{R}$. The constants n, c, χ are selected according to the desired precision, we commonly use $n = 3, c = 90$ and $\chi = 0.95$.

Numerical integration It is well-known that Gauss-Legendre quadrature works with satisfactory accuracy only for sufficiently smooth functions such as the integrands related to the elastic energy. However, the absolute value introduced by the energy density of the dislocation network, causes the exact integrand of the internal force vector components related to the density of excess dislocations (4.2) to show a jump across the line $\nabla\beta \cdot \mathrm{s} = 0$ such that

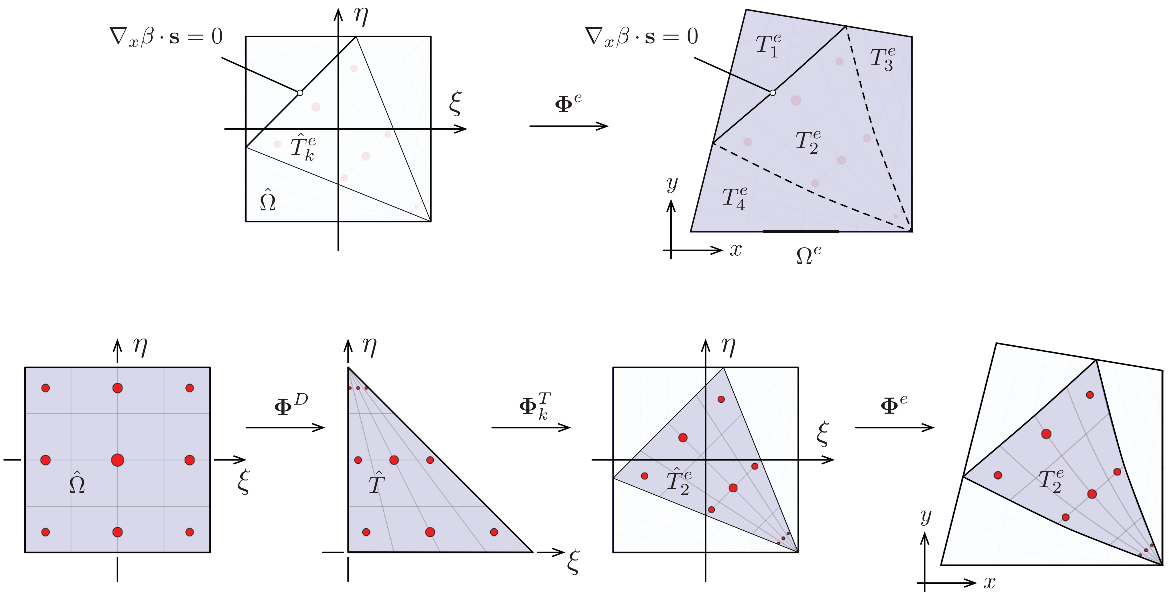
$\nabla_x\beta \cdot \mathbf{s} = 0$
η
ξ
$\hat{T}_k^e$
$\hat{\Omega}$
$\mathbf{\Phi}^e$
$\nabla_x\beta \cdot \mathbf{s} = 0$
T_1^e
T_3^e
T_2^e
T_4^e
y
x
Ω^e
η
$\hat{\Omega}$
ξ
$\mathbf{\Phi}^D$
η
$\hat{T}$
ξ
$\mathbf{\Phi}_k^T$
η
$\hat{T}_2^e$
ξ
$\mathbf{\Phi}^e$
T_2^e
y
x

Figure 4.9: Quadrature on triangles, $\hat{T} = \{(x, y)^T \in \mathbb{R}^2 \mid x, y > 0, x + y < 1\}$.

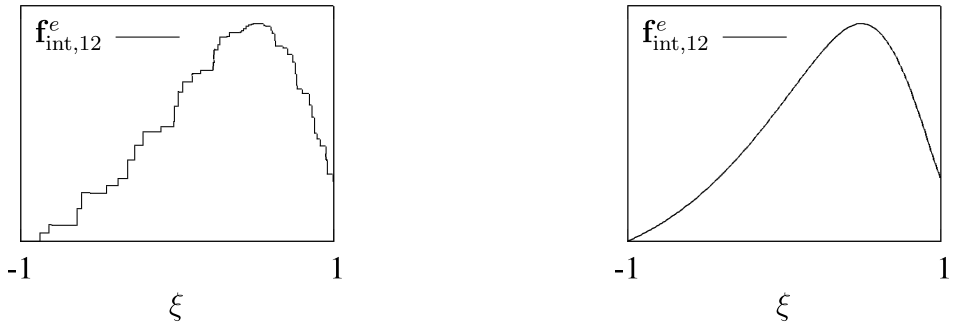

(a) 8 × 8 standard Gauss-Legendre quadrature.

(b) 4 × 4 quadrature on triangles.

Figure 4.10: Plot of internal force vector component for $\mathbf{f}^e_{\text{int}}(((1 - \xi)\hat{\mathbf{u}}^e_1 + (1 + \xi)\hat{\mathbf{u}}^e_2)/2)$.

a standard Gauss-Legendre quadrature scheme cannot be applied efficiently, see Fig. 4.8. Furthermore, whenever the line $\nabla\beta \cdot \mathbf{s} = 0$ crosses an integration point on a change of the β function during the solution procedure, the corresponding entries of $\mathbf{f}^e_{\text{int}}$ expose a jump.

In order to carry out the numerical integration of the terms related to the energy of dislocation network with good accuracy, we divide the element Ω^e in triangles T_k^e such that $\beta_{,x} \cos\varphi + \beta_{,y} \sin\varphi$ is strictly positive or strictly negative on $T_k^e, k = 1, \dots, n_t$. On those triangles, we are again integrating smooth functions. The subdivision of the reference domain is based on the intersections of the line $\nabla\beta\cdot\mathbf{s} = 0$ with the boundary of $\hat{\Omega}$. By using the two intersection points, the actual triangles are constructed using a Delaunay triangulation algorithm.

In order to obtain an integration rule of arbitrary order, we start from the Gauss-Legendre points on the quadratic reference domain $\hat{\Omega}$ which is mapped to the actual triangle by the application of a sequence of geometry maps as shown on Figure 4.9. First, $\hat{\Omega}$ is mapped on the standard triangle $\hat{T}$ using the Duffy transformation $\mathbf{\Phi}^D$ (see (Duffy, 1982)). Then, $\hat{T}$ is projected on the actual triangle T_k^e which results from the Delaunay triangulation using $\mathbf{\Phi}_k^T$. Finally, the original geometry map $\mathbf{\Phi}^e$ is applied such that the integration points for triangle k of the element e are obtained as

$$\boldsymbol{\xi}_i^{ek} = (\mathbf{\Phi}^e \circ \mathbf{\Phi}_k^T \circ \mathbf{\Phi}^D)(\boldsymbol{\xi}_i)$$

with the standard Gauss-Legendre points $\boldsymbol{\xi}_i$. The corresponding integration weights stem from the multiplication of the determinants of the involved Jacobi matrices.

The outlined integration procedure can easily be extended to more general cases with a curved boundary between the smooth subregions. Figure 4.10 shows a comparison of a standard quadrature procedure to our quadrature on triangles. It is clearly visible that the standard procedure fails to give a smooth function for the internal force vector components related to the dislocation energy. This situation is not substantially improved if a higher-order integration rule is employed. In the contrary, the quadrature on triangles, even with less number of integration points, gives a much better result for the internal force vector.

4.1.4 Numerical simulations and results

Geometry and material parameters setup

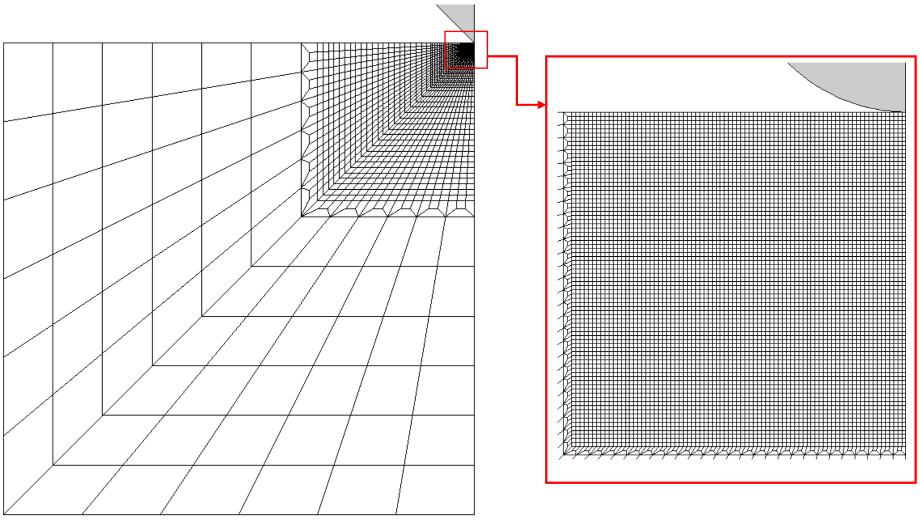

Figure 4.11: Mesh distribution and the zooming near the indenter tip.

In this Section, finite element simulations of a pure single-crystalline fcc Nickel indented by a rigid wedge indenter is reported. The aim is to compute the load acting on the indenter per unit length as well as the dislocation distribution, the lattice rotation, and the corresponding plastic slip as functions of the indentation depth for different loading and unloading paths and compare them with the experimental results obtained in (Kysar et al., 2010). These numerical simulations have been performed using an in-house FE code where we implemented the methods presented in Subsections 4.1.2 and 4.1.3.

We choose the cartesian coordinate system such that the x, y, and z-axis coincides with the crystallographic direction $[\bar{1}10]$, $[001]$, and $[110]$ of the fcc single crystal, respectively. A symmetric rigid wedge indenter (in Kysar's experiment the material of the wedge indenter is tungsten carbide) having an angle $\alpha = 90°$ and axis parallel to the z-axis is indented into the (x, z)-plane of the crystal in the y-direction. The sharp profile (consisting of two straight lines) near the tip of the indenter is replaced by a circular arc having the radius $r_d = 100\mu$m (Dahlberg et al., 2014). The plane-strain geometry of the indenter and crystal was shown schematically in Fig. 4.1, where it is sufficient to analyze only the left-half of the specimen owing to the mirror symmetry of the problem with respect to the y-axis. The sizes of the cross-section domain are chosen as $L = H = 6600\mu$m. Fig. 4.11 shows the mesh for the domain to be simulated under the indenter (represented as a gray area). This Figure also shows the zooming of the mesh and its distribution near the indenter tip. This mesh with approximately 500000 elements is designed so that it has fine elements near the indenter tip and progressively coarser elements far away from the indenter. The chosen mesh should adapt to the stress and dislocation density which are concentrated near the indenter tip while keeping the computational time for the complete loading and unloading process accessible.

We let the nodal displacement satisfy the boundary conditions (4.7), (4.8), and (4.9). The displacement in the horizontal direction and the plastic slip are zero on the very left edge and the anti-symmetric boundary of the domain, while the vertical displacement and the plastic slip are zero at the bottom of the domain.

The material parameters used in the numerical simulations are presented in Table 4.1. The Lamé constants, as well as the Poisson's ratio, are taken from (Hirth & Lothe, 1992), while for the magnitude of Burgers vector we refer to (Callister, 2007). Since the critical resolved shear stress for Nickel is quite small as compared to μ: $K = 5.7$ MPa (see, e.g., (Dieter & Bacon, 1986)), the account of dissipation with such small K does not change the load-displacement curve significantly as compared to the case $K = 0$. Therefore we shall take $K = 0$ and neglect completely the dissipation. The only one active slip system in the left-half of the specimen is chosen to be oriented at an in-plane angle of $-54.7°$ relative to the x-axis (this corresponds to the slip system (iii) in Kysar's nomenclature, see (Dahlberg et al., 2014; Kysar et al., 2010)). On the right half of the specimen the active slip system would then be the system (i) oriented under the angle $54.7°$ relative to the x-axis. Actually, there are three possible slip systems in this plane strain problem as shown in (Kysar et al., 2010), but only one slip system in each half of the specimen will be dominant due to its large Schmid factor there.

Name	**Symbol**	**Value**	**Unit**
First Lamé constant	λ	116.63	GPa
Elastic Shear Modulus	μ	94.66	GPa
Poisson ratio	ν	0.276	
Magnitude of Burgers vector	b	2.5	Å
Material constant	k	$4 \cdot 10^{-5}$	
Saturated dislocation density	ρ_s	10^{15}	m^{-2}

Table 4.1: Material parameters of single-crystalline Nickel used for simulations.

The specimen is loaded and unloaded quasi-statically by controlling the indenter displacement with the maximum depth of indentation during the simulation to be 200 μm. Thus, we see that the maximum indentation depth is quite small as compared to the sizes of the cross-section of the specimen, so the influence of the outer boundary conditions can be neglected.

Results

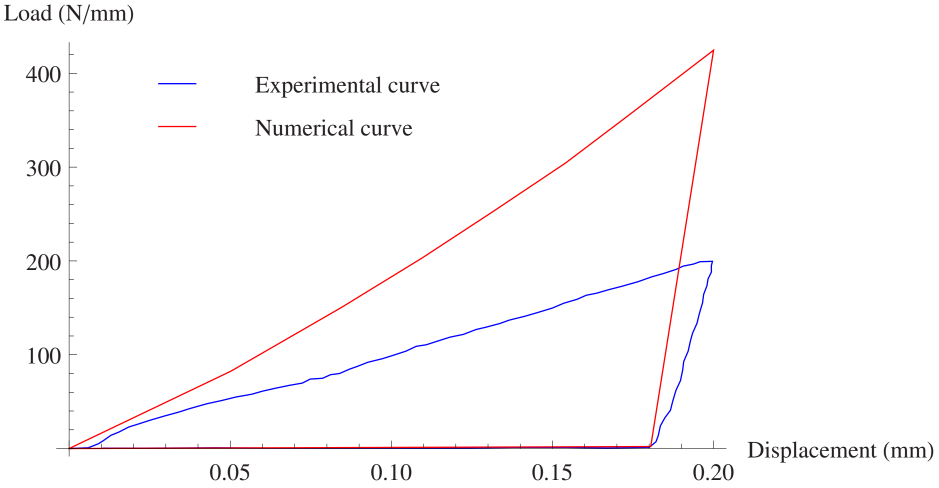

Figure 4.12: Load-displacement curve.

Load-displacement curve After finding the solution, we compute the applied load acting on the indenter per unit length by integrating the traction acting at the bottom of the domain multiplied by factor two. This is advantageous because we need neither to know the length of the contact zone nor to deal with the traction acting on the contact area between the indenter and the specimen which is less accurate. A comparison of the load-displacement curve corresponding to the loading and unloading stages of the Nickel single crystal under indentation is shown in Fig. 4.12. Although the load turns out to be higher in both stages of loading and unloading, a qualitative agreement between the experimental data from (Kysar et al., 2010) and the numerical computation data can be observed. During the loading stage when the indentation depth increases, dislocations are nucleated and pile up against the rigid indenter causing the increase of the load. We stop this loading process when the indentation depth reached its maximum value, 200 μm. Then the unloading process follows in which we decrease the indentation depth gradually until the load becomes zero. Since the difference between the resolved shear stress and the back stress becomes smaller than the critical threshold, the dislocations and the plastic slip will be frozen during this unloading process (elastic unloading). Therefore the slope of the load-displacement curve at this elastic unloading is much higher than that at the loading stage. The missing qualitative agreement could be due to the fact that two other slip systems, as well as the interaction between different groups of dislocations, are completely neglected in this simple model. As the other slip systems also produce dislocations and by this reduce the energy and consequently the stresses in the crystal. It is reasonable for us to guess that the CDT could predict a better load-displacement curve if all three slip systems together with their interaction will simultaneously be taken into account (see the load-displacement curve obtained in (Reuber et al., 2014) where all active slip systems are taken into account).

Dislocation density The dislocation distribution of the slip system (iii) in the left half of the specimen underneath the indenter tip at the maximum value of the indentation depth $h = 200\mu\text{m}$, computed from the experimentally measured lattice rotation (see the next paragraph), is shown in Fig. 4.13a and Fig. 4.13b (these Figures are obtained as the left half of Fig. 9 from (Kysar et al., 2010)). It is seen that a high density of dislocations is concentrated underneath the indenter tip, at the contact surface as well as on the anti-symmetric

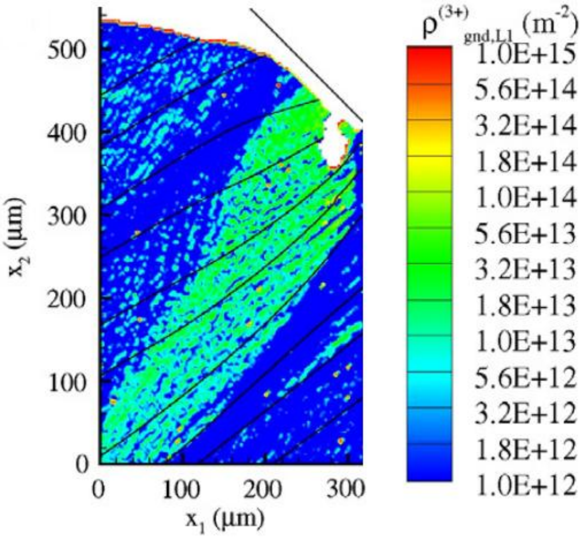

(a) ρ^+, with crystallographic traces normal to the slip direction, $h = 200\mu$m.

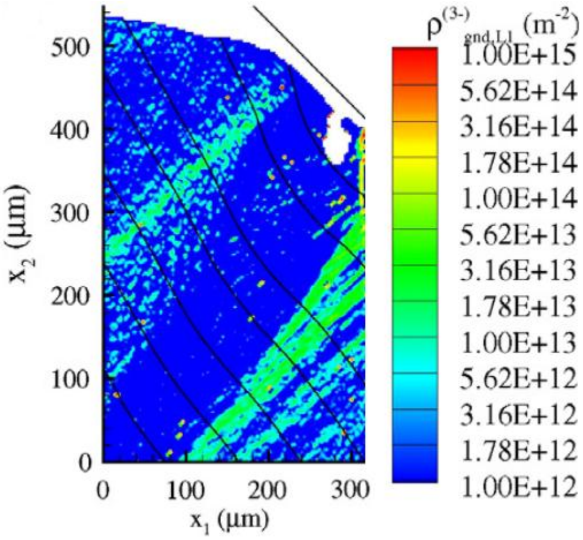

(b) ρ^-, with crystallographic traces tangential to the slip direction, $h = 200\mu$m..

Figure 4.13: Experimental GND density of the slip system (iii) from Kysar et al. (2010). Reprinted by permission.

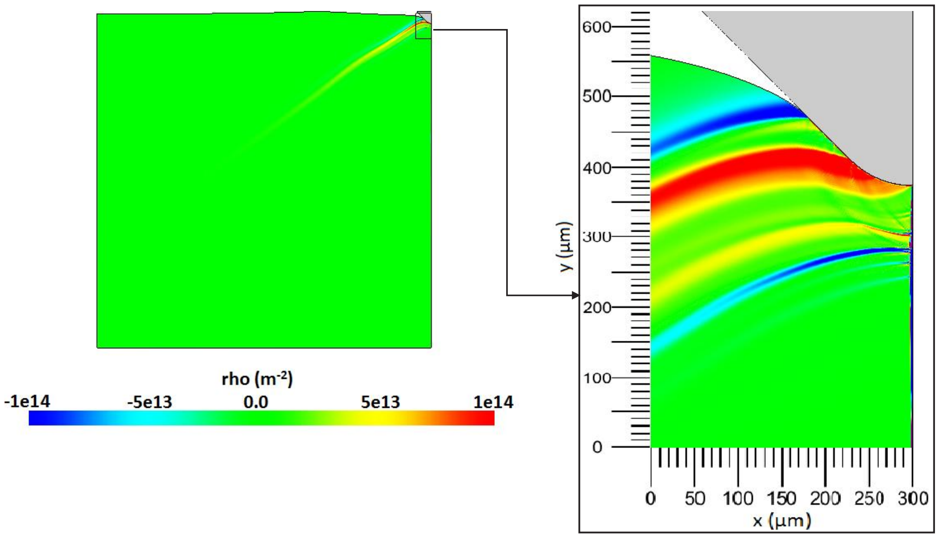

Figure 4.14: Simulated GND density $\frac{1}{b}(\beta_{,x}\cos\varphi + \beta_{,y}\sin\varphi)$, $h = 200\mu$m.

boundary line. The zones of high densities of positive and negative dislocations are closely oriented to the direction of normal to the slip planes of the slip system (iii). Besides, the negative dislocations are located close to the anti-symmetry line and concentrated in several strips emanating from the contact point and the symmetry line. On the contrary, the positive dislocations are concentrated mainly in a zone emanating from the contact surface and partly from the zone of negative dislocation on the symmetry line. The distribution of $\frac{1}{b}(\beta_{,x}\cos\varphi+\beta_{,y}\sin\varphi)$ computed in our numerical simulations at the same indentation depth giving both the positive and negative dislocation density is shown in Fig. 4.14. One can see on the left that, except the small region underneath the indenter, the dislocation density is zero everywhere. On the right of this Figure, the zooming of the region underneath the indenter together with the dislocation density distribution is shown. Although there are still some quantitative difference in the dislocation density distribution, the numerical computation outputs give the qualitatively similar features of the dislocation distribution compared to those obtained from experiments: i) high density of dislocations are concentrated at the indenter tip, at the contact surface as well as on the anti-symmetric boundary line, ii) the negative dislocations are located close to the anti-symmetry boundary and at several strips emanating from the contact point and from the symmetry line, iii) the positive dislocations are concentrated mainly in a strip from the contact area. Far away from the indenter tip, the strips are closely oriented to the direction of normal to the slip planes of the slip system (iii). Surprisingly, as compared to the similar results obtained in a much more complicated continuum dislocation dynamics model in (Reuber et al., 2014) the results obtained in our study capture even better the details of the distribution of dislocations in the experiment.

Lattice rotation The experimentally measured lattice rotation in the left half of the specimen underneath the indenter tip at the maximum value of the indentation depth $h = 200\mu$m is shown in Fig. 4.15 (cf. the left half of Fig. 3a in (Kysar et al., 2010)). Due to the mirror symmetry, the lattice rotation on the antisymmetry axis must ideally be zero. It is remarkable that the lattice rotation jumps from about $+20°$ to about $-20°$ when crossing the upper part of the line of antisymmetry. There are two zones of positive (anti-clockwise) and negative (clockwise) lattice rotation: the zone of positive lattice rotation emanates from the indenter tip and the anti-symmetric line, while that of negative lattice rotation from the contact sur-

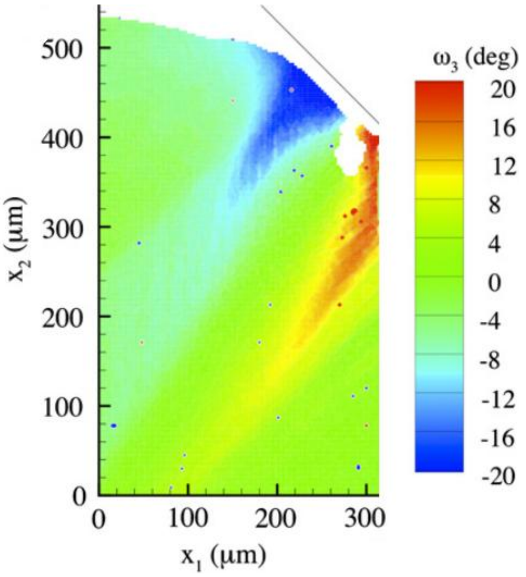

Figure 4.15: Experimental lattice rotation w_z^e from Kysar et al. (2010). Reprinted by permission.

face. These zones are closely aligned with the direction of the normal to the slip system (iii) in the left half of the specimen. To be able to compare with the experimental lattice rotation given in degree, we plot in Fig. 4.16 the following distribution

$$[\frac{1}{2}(v_{,x} - u_{,y}) + \frac{1}{2}\beta] \times 180^\circ/\pi$$

obtained from numerical solution at the same indentation depth, which is the lattice rotation according to CDT (in degree). On the right of this Figure, the zooming of the region together with the lattice rotation distribution is shown. Except for some quantitative differences, one can recognize there quite similar features as those obtained in experiments. The simulated lattice rotation also exhibits the jump from about $+20^\circ$ to about -20° when crossing the upper part of the line of antisymmetry. There are also two zones of positive and negative lattice rotation: the zone of positive lattice rotation emanates from the anti-symmetric line, while that of negative lattice rotation from the contact surface. On the left of Fig. 4.16 the distribution of lattice rotation is shown in the whole domain, where it is seen that the zones of non-zero lattice rotation are closely aligned with the direction of the normal to the slip system (iii).

Plastic slip The plastic slip obtained by the numerical simulations is shown in Fig. 4.17. Near the indenter (shown on the right of this Figure) we observe two zones of positive and negative plastic slip: the zone of positive plastic slip emanates from the contact area and partly from the anti-symmetry line. There exists a zone of high plastic slip of the slip system (iii) extending down toward the antisymmetry boundary along the local s^1 direction. The zone of negative plastic slip is detached from the contact surface. Far away from the indenter (see the left of this Figure) we observe the slip bands of positive and negative plastic slip which are aligned with the normal direction to the slip plane. It is interesting to compare our results with the similar numerical simulations within the single crystal plasticity theory provided by Saito, Oztop, and Kysar (2012) (see also (Saito & Kysar, 2011)). It was shown in (Saito et al., 2012) that the dominant slip system having the largest plastic slip rate in the right half of the specimen is the system (i) oriented under the angle 54.7° relative to

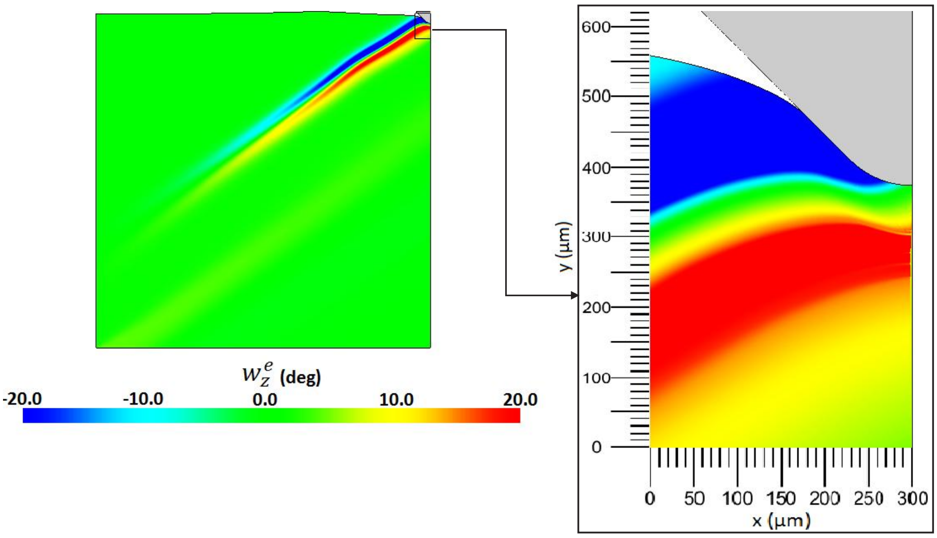

Figure 4.16: Simulated lattice rotation $[\frac{1}{2}(v_{,x} - u_{,y}) + \frac{1}{2}\beta] \times 180°/\pi$, $h = 200\mu$m.

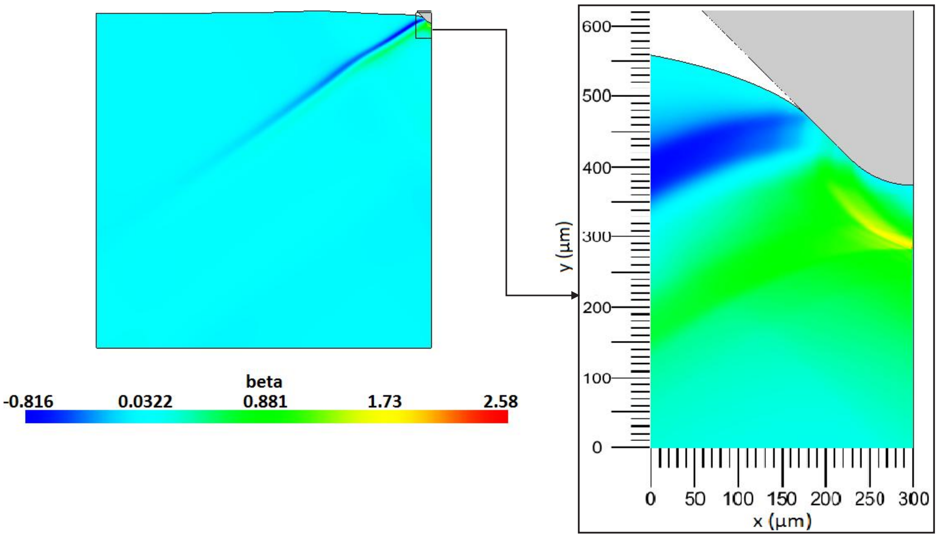

Figure 4.17: Simulated plastic slip, $h = 200\mu$m.

the x-axis. This means that the dominant slip system in the left-half of the specimen must be the system (iii) oriented under the angle -54.7° relative to the x-axis that agrees with our choice of the active slip system. Saito et al. (2012) obtained also in the right-half of the specimen a concentrated glide shear on slip system (i) that emanates from the contact point singularity and extends down toward the antisymmetry boundary along the local $\mathbf{s}^1$ direction from which concentrated kink-shear is activated and extends down and away from the antisymmetry line in the direction of the local $\mathbf{m}^1$. This is similar to the above features of the plastic slip distribution obtained in our simulations.

4.2 Anti-plane constrained shear

4.2.1 Energy density of excess dislocations and its extrapolation

The thermodynamic dislocation theory (TDT), proposed initially by Langer, Bouchbinder, and Lookmann (Langer et al., 2010) and developed further in Langer (2015, 2016, 2017a, 2017c); Le et al. (2017, 2018), deals with the uniform plastic deformations of crystals driven by a constant strain rate. During these uniform plastic deformations, the crystal may have only redundant dislocations whose resultant Burgers vector vanishes. As shown in Le (2018); Le and Piao (2018), the extension of TDT to non-uniform plastic deformations including excess dislocations due to the incompatibility of the plastic distortion Nye (1953) is based on the phenomenological free energy density proposed by Berdichevsky (2006b). Berdichevsky (2017) has shown later that the asymptotically exact free energy density of excess dislocations in a twisted bar can be found, and Le and Piao (2018) has extent Berdichevsky's idea to the anti-plane shear deformation. The formula is the following:

$$\psi_m(\rho^g) = \mu b^2 \rho^g \left[\psi^\star + \frac{1}{4\pi} \ln \frac{1}{b^2 \rho^g} \right]. \tag{4.21}$$

Where excess dislocation density ρ^g is a function of the gradient of plastic distortion β. μ and b is shear modulus and magnitude of Burger's vector respectively, and $\psi^\star$ is a parameter depending on the periodic dislocation structure. For the hexagonal periodic dislocation structure $\psi^\star = -0.105$.

The Eq. (4.21) can be written into the dimensionless energy density of excess dislocations as

$$f(y) = \psi_m/\mu = y \left(\psi^\star - \frac{1}{4\pi} \ln y \right), \tag{4.22}$$

where $y = b^2 \rho^g$ is the dimensionless dislocation density. This function is plotted for $y \in (0, 1)$ as in Fig. 4.18. There are three remarkable properties of this Eq. (4.22): First, $f(y)$ is concave; Second, $f(y)$ tends to $-\infty$ when $y \to \infty$; Third $f'(y) = \infty$. With these features, it is problematic to apply Eq.(4.22) in order to determine the average plastic slip via energy minimization within the continuum approach. For the well-posed boundary value problems within the continuum approach, the energy density and its derivative with respect to ρ^g respectively require to be convex and regular (the latter is needed for the regularity of the back-stress). Looking more closely at the assumptions made in deriving Eq. (4.21) where the dislocation density is assumed to be locally double-periodic distribution (see Berdichevsky

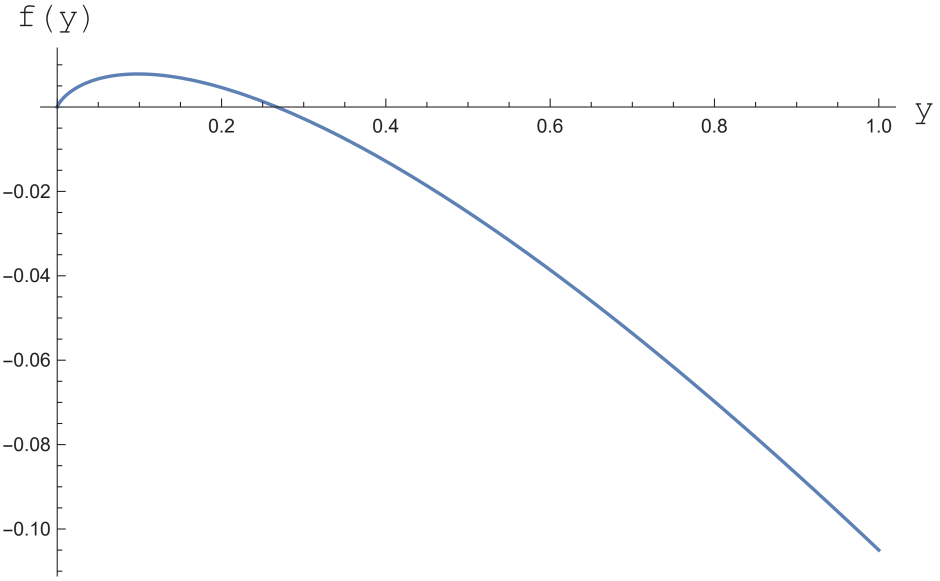

Figure 4.18: Dimensionless energy density $f(y) = \psi_m/\mu$.

(2017); Le and Piao (2018)), these assumptions can be violated for the extremely small or large dislocation densities. Such extreme values of dislocation densities may occur near the head or the tail of the dislocation pile-up. In these cases, the dislocations are either at the wall or adjacent to the dislocation free-zone, so the local periodicity is no longer valid there. It is, therefore, the energy density Eq. (4.21) must be extrapolated to the extremely small or large dislocation densities. Le et al. (2018) proposed the following extrapolation for the free energy density

$$\psi_m(\rho^g) = \mu b^2 \rho^g \left(\psi^\star + \frac{1}{4\pi} \ln \frac{1}{k_0 + b^2 \rho^g} \right) + \frac{1}{8\pi} \mu k_1 (b^2 \rho^g)^2. \tag{4.23}$$

with k_0 and k_1 being two new material parameters. The small constant k_0 corrects the behavior of the derivative of energy at $\rho^g = 0$, while the last term containing k_1 corrects the behavior of the energy at large density of the excess dislocations. The two parameters k_0 and k_1 are chosen so that, the energy density is not only close to the asymptotic exact energy density for moderate dislocation densities but also is the convex function for all positive dislocation densities. The latter requirement guarantees the existence of the energy minimizer. Le and Piao (2018) also proposed a sufficient constraint for these two coefficient $k_0 k_1 > 2$ in order to ensure the convexity of function ψ_m. Fig. 4.19 shows the comparison between two dimensionless energy density ψ_m/μ defined according to Eq. (4.21) and Eq. (4.23) within the range $\rho^g \in (0, 10^{14}/\mathrm{m}^2)$ and the range $\rho^g \in (0, 10^{16}/\mathrm{m}^2)$, here, $b = 10^{-10}$ m, $k_0 = 10^{-6}$, $k_1 = 2.1 \times 10^6$. one can see that the two energy densities are approximately the same in the range $\rho^g \in (0, 10^{14}/\mathrm{m}^2)$, but differ substantially for ρ^g larger than $10^{14}/\mathrm{m}^2$.

4.2.2 Equations of Motion

Suppose, for simplicity, that the single crystal beam has a rectangular cross-section, of width c and height h, that lies in the (x, y)-plane. This crystal beam is placed in a "hard device" such that at its side boundary the displacement in the z-direction is prescribed: $w = \gamma(t) y$, with $\gamma(t)$ being the shear strain regarded as a control parameter (see Fig. 4.20). Under this condition, dislocations cannot reach the boundary, as otherwise, the steps formed by

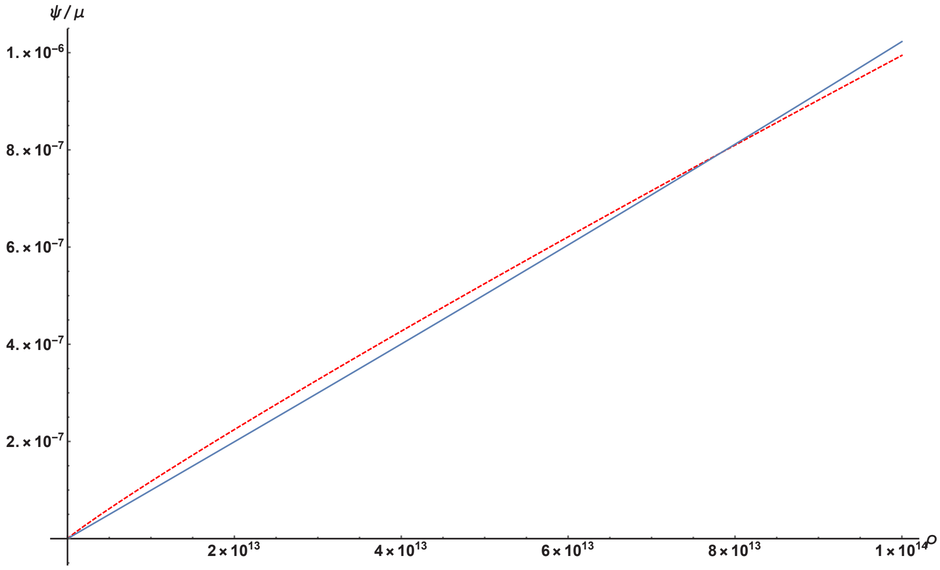

(a) $\rho^g \in (0, 10^{14}/\mathrm{m}^2)$.

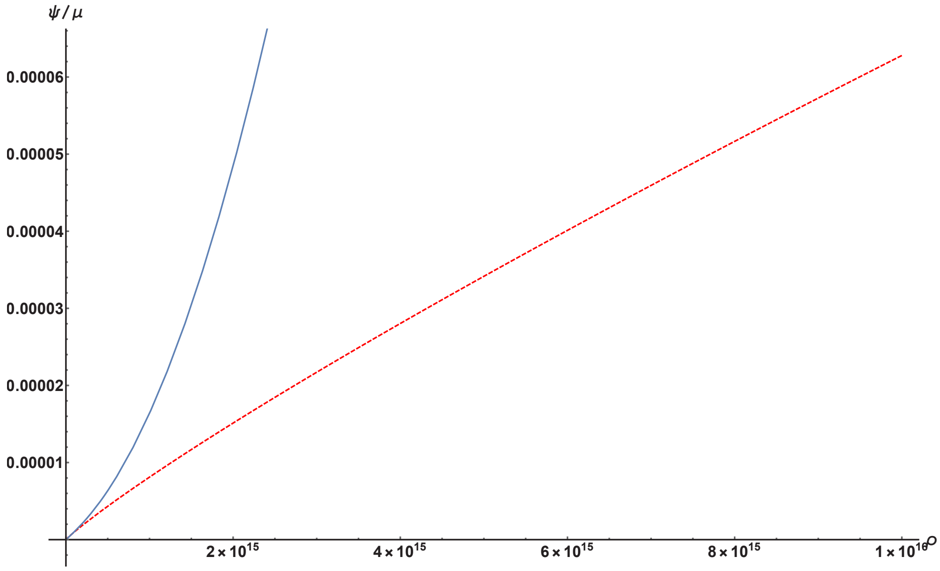

(b) $\rho^g \in (0, 10^{16}/\mathrm{m}^2)$.

Figure 4.19: The dimensionless energy density ψ_m/μ within two different range of ρ^g. The dashed line refers to Eq. (4.21), and the bold line refers to Eq. (4.23).

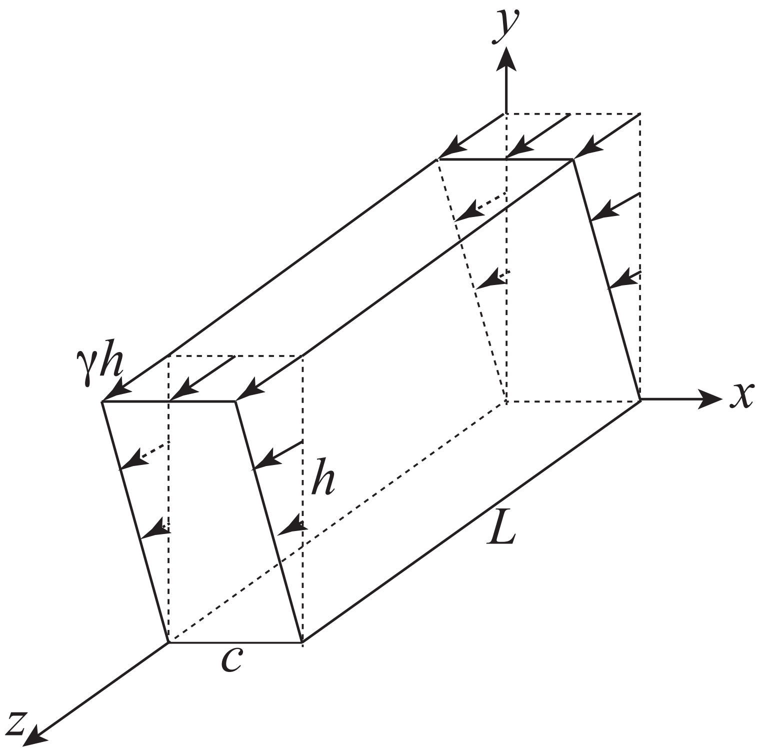

Figure 4.20: Anti-plane constrained shear.

them (equal to the length of the Burgers vector) would contradict the smoothness of the displacement specified there. In this sense, the ”hard” boundary conditions model the grain boundaries that serve as obstacles and prevent dislocations from leaving the grain. If $h \gg c$, the end-effect near $y = 0$ and $y = h$ may be neglected and assume that all state variables depend only on the spatial coordinate x.

Now, let this system be driven at a constant shear rate $\dot{\gamma} \equiv Q/t_0$, where t_0 is a characteristic microscopic time scale. Because the system is undergoing steady-state anti-plane shear, the time t can be replaced by the total strain γ so that $t_0\, \partial/\partial t \to Q\, \partial/\partial\gamma$. The equations of motion are taken from Eqs. (2.73a),(2.73b), and (2.73c) with minor modification:

$$\frac{\partial \tau_Y}{\partial \gamma} = \mu \left[1 - \frac{q(\gamma)}{Q}\right], \tag{4.24}$$

$$\frac{\partial \rho}{\partial \gamma} = \kappa_1 \frac{\tau_Y\, q}{a^2 \nu(\theta,\rho,Q)^2\, \mu\, Q} \left[1 - \frac{\rho}{\rho_{ss}(\chi)}\right], \tag{4.25}$$

$$\frac{\partial \chi}{\partial \gamma} = \kappa_2 \frac{\tau_Y e_D\, q}{\mu\, Q} \left(1 - \frac{\chi}{\chi_0}\right), \tag{4.26}$$

with μ being the shear modulus. Note that, for the uniform plastic deformation involving only redundant dislocations $q(\gamma)/t_0$ equals the plastic shear rate $\dot{\beta}$, with β being the uniform plastic distortion, but in general when β is non-uniform it is not necessarily so. The state variables that describe this system are the elastic strain $\gamma - \beta$, the areal densities of redundant dislocations ρ_r and excess dislocations $\rho_g \equiv |\beta_{,x}|/b$ (where b is the length of the Burgers vector), and the effective disorder temperature χ (cf. Kröner (1992); Langer (2016)). All four quantities, $\gamma - \beta$, ρ_r, ρ_g, and χ, are functions of γ.

The equation for the plastic distortion β reads

$$\tau - \tau_B - \tau_Y = 0. \tag{4.27}$$

This equation is the balance of microforces acting on excess dislocations. Here, the first term $\tau = \mu(\gamma - \beta)$ is the applied shear stress, the second term the back-stress due to the interaction of excess dislocations, and the last one the flow stress. This balance of microforces can be derived from the variational equation for irreversible processes Le (2018); Le and Piao (2018) yielding

$$\tau_B = -\frac{1}{b}(\frac{\partial \phi_m}{\partial \rho_g})_{,x} \text{sign} \beta_{,x} = -\frac{1}{b^2}\frac{\partial^2 \phi_m}{\partial (\rho_g)^2}\beta_{,xx}, \tag{4.28}$$

with ϕ_m being the free energy density of excess dislocations. Berdichevsky (2017) has found ϕ_m for the locally periodic arrangement of excess screw dislocations. However, as shown by us in Le and Piao (2018), his expression must be extrapolated to the extremely small or large dislocation densities to guarantee the existence of solution within TDT. Using the extrapolated energy proposed in Le and Piao (2018), the back-stress is obtained

$$\tau_B = -\mu b^2 \frac{k_1 \xi^2 + (2k_0 k_1 - 1)\xi + k_1 k_0^2 - 2k_0}{4\pi (k_0 + \xi)^2}\beta_{,xx}, \tag{4.29}$$

where $\xi = b|\beta_{,x}|$. Equation (4.27) is subjected to the Dirichlet boundary condition $\beta(0) = \beta(c) = 0$.

4.2.3 Discretization and method of solution

For the purpose of numerical integration of the system of equations (4.24)-(4.29) it is convenient to introduce the dimensionless variables and quantities

$$\tilde{x} = x/b,\ \tilde{\rho} = a^2 \rho,\ \tilde{\tau} = \tau/\mu,\ \tilde{\tau}_Y = \tau_Y/\mu,\ \tilde{\tau}_B = \tau_B/\mu. \tag{4.30}$$

The variable $\tilde{x}$ changes from 0 to $\tilde{c} = c/b$. The dimensionless plastic strain rate q is rewritten in the form

$$q(\tau_Y, \rho) = \frac{b}{a}\tilde{q}(\tilde{\tau}_Y, \tilde{\rho}), \tag{4.31}$$

where

$$\tilde{q}(\tilde{\tau}_Y, \tilde{\rho}) = \sqrt{\tilde{\rho}}[\tilde{f}_P(\tilde{\tau}_Y, \tilde{\rho}) - \tilde{f}_P(-\tilde{\tau}_Y, \tilde{\rho})]. \tag{4.32}$$

We set $\tilde{\mu}_T = (b/a)\mu_T = \mu s$ and assume that s is independent of temperature and strain rate. Then

$$\tilde{f}_P(\tilde{\tau}_Y, \tilde{\rho}) = \exp\Big[-\frac{1}{\theta}\, e^{-\tilde{\tau}_Y/(r\sqrt{\tilde{\rho}})}\Big]. \tag{4.33}$$

We define $\tilde{Q} = (a/b)Q$ so that $q/Q = \tilde{q}/\tilde{Q}$. Then,

$$\tilde{\nu}(\theta, \tilde{\rho}, \tilde{Q}) \equiv \ln\Big(\frac{1}{\theta}\Big) - \ln\Big[\ln\Big(\frac{\sqrt{\tilde{\rho}}}{\tilde{Q}}\Big)\Big]. \tag{4.34}$$

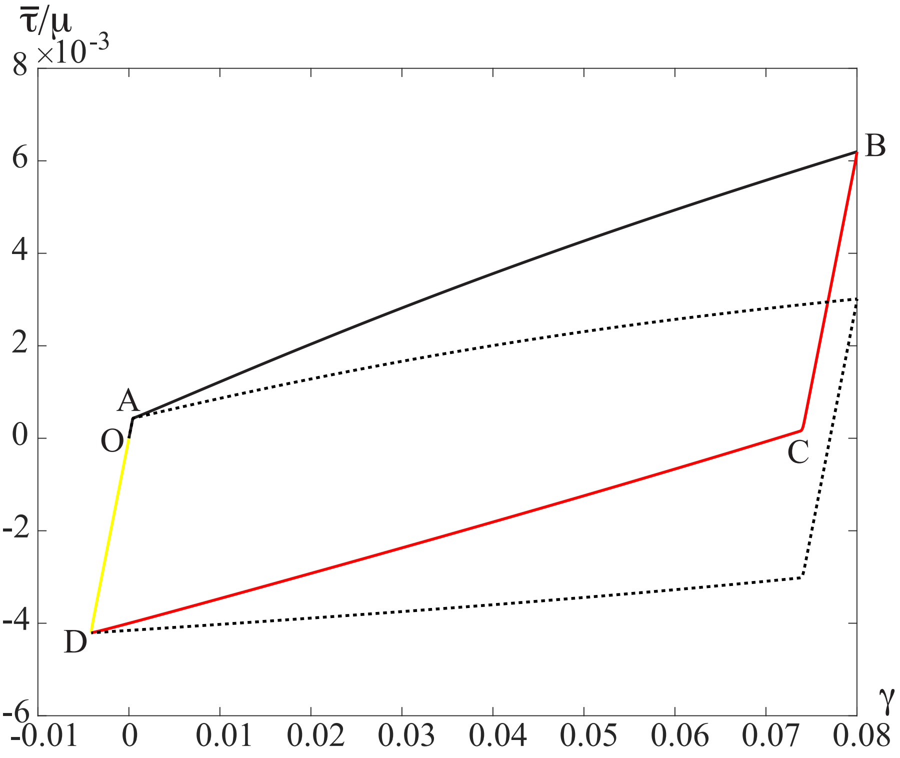

Figure 4.21: Stress-strain curves at the strain rate $\tilde{Q} = 10^{-13}$, for room temperature, and for $\gamma^* = 0.08$: (i) loading path OAB (black), (ii) load reversal BCD (red/dark gray), (iii) second load reversal DO (yellow/light gray), (iv) flow stress versus strain (dashed black curve).

The dimensionless steady-state quantities are

$$\tilde{\rho}_{ss}(\tilde{\chi}) = e^{-1/\tilde{\chi}}, \quad \tilde{\chi}_0 = \chi_0/e_D. \tag{4.35}$$

Using $\tilde{q}$ instead of q as the dimensionless measure of plastic strain rate means that t_0 is effectively rescaled by a factor b/a. For purposes of this analysis, it is assumed that $(a/b)t_0 = 10^{-12}$s.

In terms of the introduced dimensionless quantities the governing equations read

$$\frac{\partial \tilde{\tau}_Y}{\partial \gamma} = \left[1 - \frac{\tilde{q}(\tilde{\tau}_Y, \tilde{\rho})}{\tilde{Q}}\right], \tag{4.36}$$

$$\frac{\partial \tilde{\rho}}{\partial \gamma} = \kappa_1 \frac{\tilde{\tau}_Y \, \tilde{q}}{\tilde{\nu}(\theta, \tilde{\rho}, \tilde{Q})^2 \, \tilde{Q}} \left[1 - \frac{\tilde{\rho}}{\tilde{\rho}_{ss}(\tilde{\chi})}\right], \tag{4.37}$$

$$\frac{\partial \tilde{\chi}}{\partial \gamma} = \kappa_2 \frac{\tilde{\tau}_Y \, \tilde{q}}{\tilde{Q}} \left(1 - \frac{\tilde{\chi}}{\tilde{\chi}_0}\right), \tag{4.38}$$

$$\gamma - \beta - \tilde{\tau}_B - \tilde{\tau}_Y = 0, \tag{4.39}$$

where

$$\tilde{\tau}_B = -\frac{k_1 \xi^2 + (2k_0 k_1 - 1)\xi + k_1 k_0^2 - 2k_0}{4\pi (k_0 + \xi)^2} \beta_{,\tilde{x}\tilde{x}}, \tag{4.40}$$

and $\xi = |\beta_{,\tilde{x}}|$. To solve this system of partial differential equations subject to initial and boundary conditions numerically, the equations are discretized in the interval $(0 < \tilde{x} < \tilde{c})$

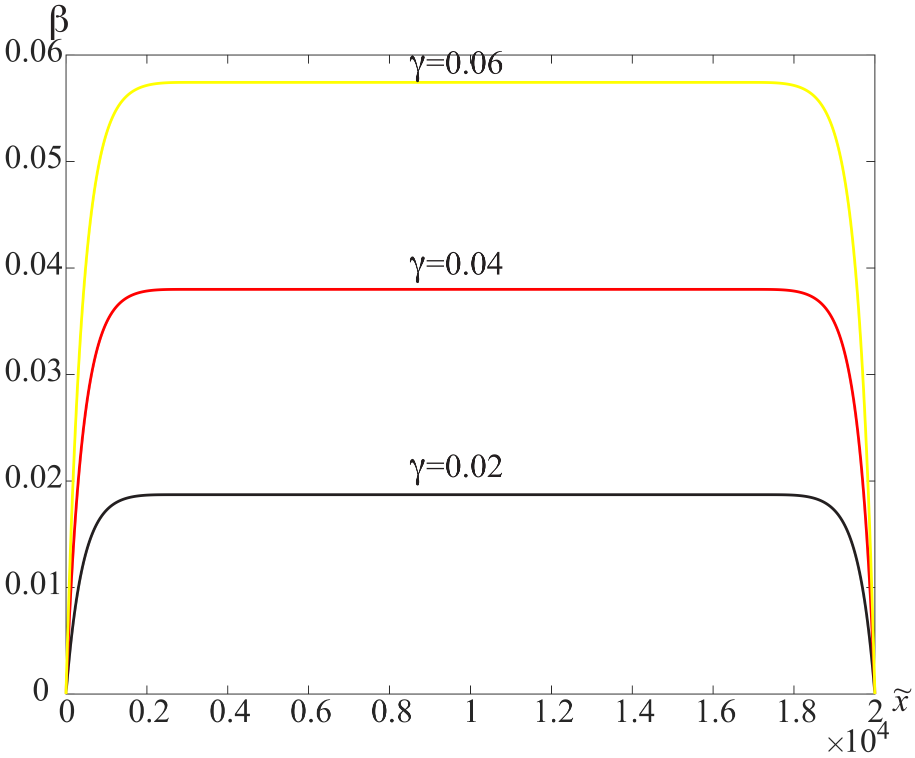

Figure 4.22: Evolution of $\beta(\tilde{x})$ at the strain rate $\tilde{Q} = 10^{-13}$ and for room temperature during the loading along AB: (i) $\gamma = 0.02$ (black), (ii) $\gamma = 0.04$ (red/dark gray), (iii) $\gamma = 0.06$ (yellow/light gray).

by dividing it into n sub-intervals of equal length $\Delta\tilde{x} = \tilde{c}/n$. Then the first and second spatial derivative of β in equation (4.39) are approximated by

$$\frac{\partial\beta}{\partial\tilde{x}}(\tilde{x}_i) = \frac{\beta_{i+1} - \beta_i}{\Delta\tilde{x}}, \tag{4.41}$$

$$\frac{\partial^2\beta}{\partial\tilde{x}^2}(\tilde{x}_i) = \frac{\beta_{i+1} - 2\beta_i + \beta_{i-1}}{(\Delta\tilde{x})^2}, \tag{4.42}$$

where $\beta_i = \beta(\tilde{x}_i)$. In this way, the four partial differential equations are reduced to a system of $4n$ ordinary differential-algebraic equations. These have been solved numerically using the Matlab-ode15s solver with $n = 1000$ and the γ step equal to 10^{-6}.

After shearing the specimen up to the shear strain γ^*, the crystal is unloaded and loaded further in the opposite direction by reversing the direction of change of γ. The latter will now be reduced with the same rate from γ^* to some negative value γ_*, to be specified later. The author postulate that the system of governing equations (4.36)-(4.39) remains valid during this load reversal. Besides, as initial conditions, all quantities $\tilde{\tau}_Y$, $\tilde{\rho}$, $\tilde{\chi}$, and β assume those values $\tilde{\tau}_Y(\gamma^*)$, $\tilde{\rho}(\gamma^*)$, $\tilde{\chi}(\gamma^*)$, and $\beta(\gamma^*)$ achieved at the end of the loading, thus satisfying the continuity requirement. Since the equations remain valid during the load reversal with the same magnitude of the strain rate, $\tilde{Q}$ is unchanged, reverse the expression for $\tilde{q}$ to

$$\bar{q}(\tilde{\tau}_Y, \tilde{\rho}) = \sqrt{\tilde{\rho}}[\tilde{f}_P(-\tilde{\tau}_Y, \tilde{\rho}) - \tilde{f}_P(\tilde{\tau}_Y, \tilde{\rho})], \tag{4.43}$$

and integrate the system (4.36)-(4.39), with $\tilde{q}$ being replaced by $\bar{q}$, backwards in γ. If the next load reversal with the same shear rate should be made after reaching γ_*, $\tilde{q}$ is switched again and the system (4.36)-(4.39) is integrated, with the initial conditions satisfying the

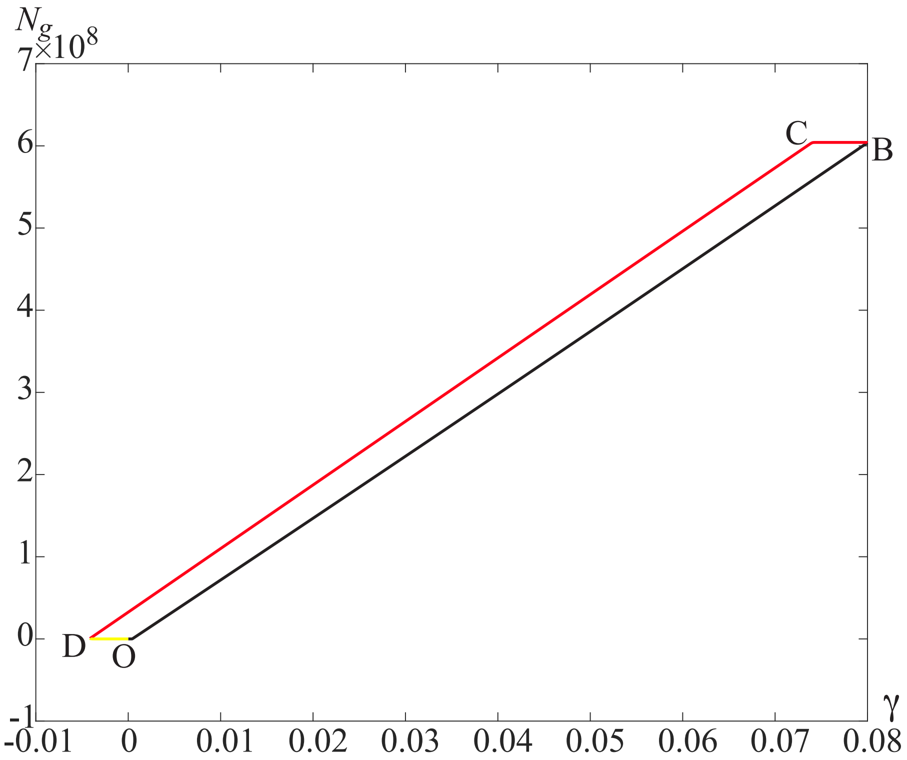

Figure 4.23: N_g versus γ at the strain rate $\tilde{Q} = 10^{-13}$, for room temperature, and for $\gamma^* = 0.08$: (i) loading path (black), (ii) load reversal (red/dark gray), (iii) second load reversal (yellow/light gray).

continuity requirement, forwards in γ. The magnitude of the strain rate $\tilde{Q}$ can also be changed if necessary. Thus, the numerical simulation with several load reversals and different strain rates can be realized in this way.

After finding the solution, the average rescaled stress can be computed according to

$$\bar{\tau}/\mu = \frac{1}{\tilde{c}} \int_0^{\tilde{c}} \tilde{\tau} d\tilde{x}. \tag{4.44}$$

The average flow stress is computed similarly. The total number of dislocations per unit height is

$$N = \int_0^c \rho \, dx = \frac{b}{a^2} \int_0^{\tilde{c}} \tilde{\rho} \, d\tilde{x}. \tag{4.45}$$

The number of excess dislocations per unit height equals

$$N_g = 2 \int_0^{c/2} \rho_g \, dx = \frac{2}{b} \int_0^{c/2} \beta_{,x} \, dx = \frac{2}{b} \beta_m, \tag{4.46}$$

where $\beta_m = \beta(\tilde{c}/2)$. Then, obviously, $N_r = N - N_g$.

4.2.4 Numerical simulations

Let the anti-plane shear test be done at room temperature $T = 298$K and at the strain rate $\tilde{Q} = 10^{-13}$. The parameters for copper at this room temperature are chosen as follows

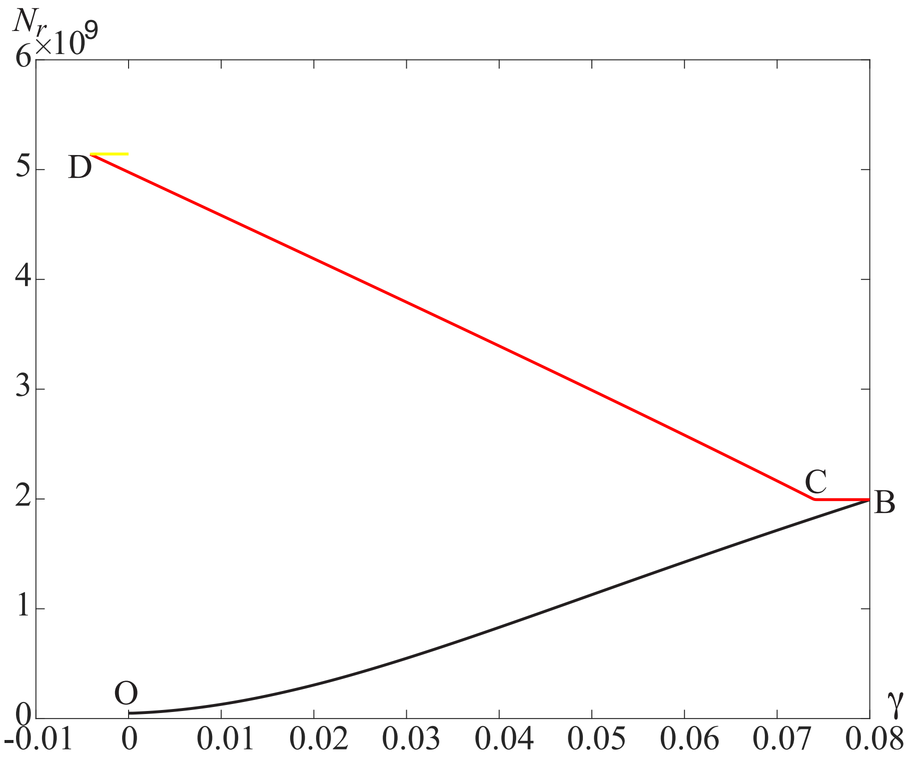

Figure 4.24: N_r versus γ at the strain rate $\tilde{Q} = 10^{-13}$, for room temperature, and for $\gamma^* = 0.08$: (i) loading path (black), (ii) load reversal (red/dark gray), (iii) second load reversal (yellow/light gray).

Langer et al. (2010)

$$s = 0.0323,\ \theta = 0.0073,\ \kappa_1 = 96.1\ \kappa_2 = 350,\ \tilde{\chi}_0 = 0.25.$$

We take $c = 5.1$ micron, $b = 2.55$Å and $a = 10b$. In addition, the parameters k_0 and k_1 required to compute the back stress Le and Piao (2018) are: $k_0 = 10^{-6}$, $k_1 = 2.1 \times 10^6$. We choose also the initial conditions

$$\tilde{\tau}_Y(0) = 0,\ \tilde{\rho}(0) = 6.25 \times 10^{-5},\ \tilde{\chi}(0) = 0.18,\ \beta(0) = 0.$$

This initial dislocation density in real dimension equals 10^{13}/m^2.

The results of numerical simulations are presented in Figs. 4.21-4.29. In Fig. 4.21 the average normalized shear stress versus shear strain curve (called for short stress-strain curve) with the strains at the beginning of load reversals $\gamma^* = 0.08$ and $\gamma_* = -0.00414$ is shown. We plot there also the average rescaled flow stress $\bar{\tau}_Y/\mu$ versus γ (dashed black curve) for comparison. The loading path OAB (black curve) consists of the elastic line OA and the hardening curve AB. The yielding transition occurs at A. Fig. 4.22 shows the plastic distortion β at three different γ along the hardening curve AB that agrees well with the approximate analytical solution found in Le and Piao (2018). The excess dislocations pile up against the left and right boundaries, leaving the center of the specimen free of excess dislocations. As γ increases the number of excess and redundant dislocations as well as the effective temperature also increase as shown in Fig. 4.23-4.25.

During the load reversal BCD (red/dark gray), it is first observed the elastic unloading BC where the redundant and excess dislocations as well as the effective temperature (in the

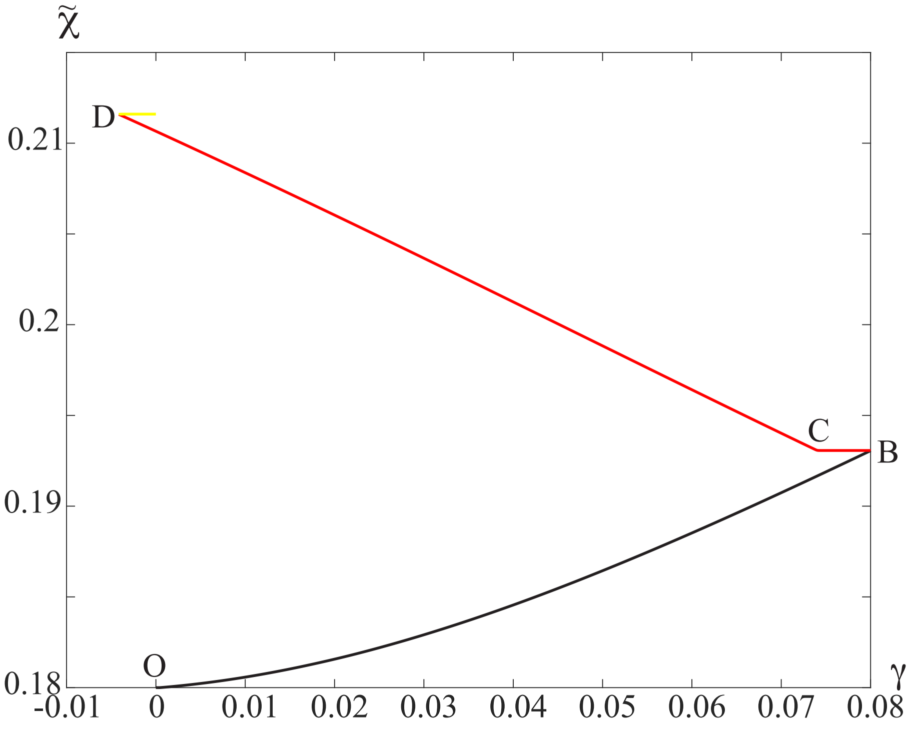

Figure 4.25: $\tilde{\chi}(\tilde{c}/2)$ versus γ at the strain rate $\tilde{Q} = 10^{-13}$, for room temperature, and for $\gamma^* = 0.08$: (i) loading path (black), (ii) load reversal (red/dark gray), (iii) second load reversal (yellow/light gray).

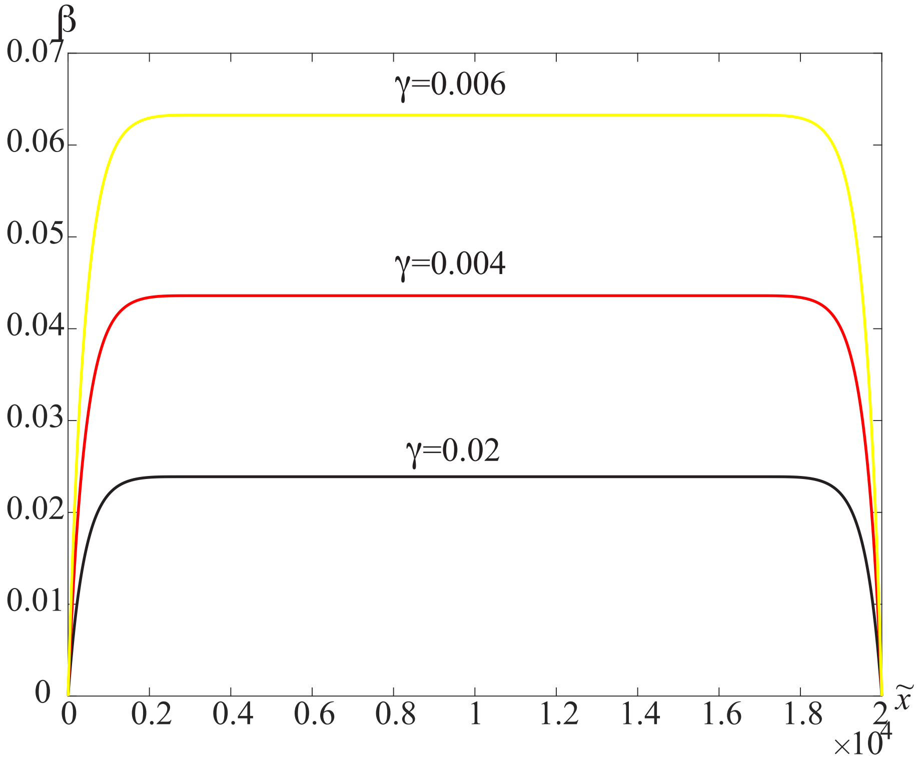

Figure 4.26: Evolution of $\beta(\tilde{x})$ at the strain rate $\tilde{Q} = 10^{-13}$ and for room temperature during the load reversal along CD: (i) $\gamma = 0.02$ (black), (ii) $\gamma = 0.04$ (red/dark gray), (iii) $\gamma = 0.06$ (yellow/light gray).

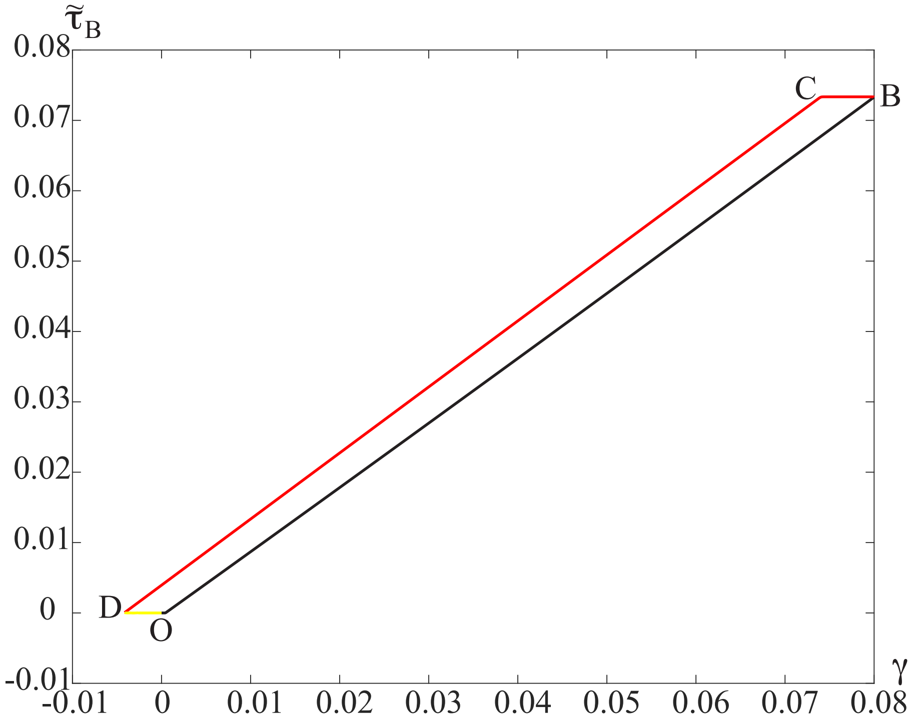

Figure 4.27: The normalized back stress $\tilde{\tau}_B$ near the boundary versus γ at the strain rate $\tilde{Q} = 10^{-13}$, for room temperature, and for $\gamma^* = 0.08$: (i) loading path (black), (ii) load reversal (red/dark gray), (iii) second load reversal (yellow/light gray).

middle of the specimen) are frozen as seen in Figs. 4.23-4.25. The yielding transition occurs at C, where the magnitude of the stress is much lower than that at the end of the loading path exhibiting the Bauschinger effect. To explain this effect the author plots in Fig. 4.27 the evolution of the normalized back stress $\tilde{\tau}_B$ (near the boundary) as γ changes. This back stress increases during the loading due to the increasing number of excess dislocations, and then remain unchanged during the unloading when the dislocations are frozen along the line BC. The presence of this positive back stress reduces the magnitude of shear stress required for pulling the excess dislocations back to the center of the specimen. There, the excess dislocations of opposite signs meet and annihilate each other, so the number of excess dislocations reduces gradually to zero along the curve CD as shown in Fig. 4.23. Fig. 4.26 shows the evolution of the plastic distortion at three different γ that confirms this tendency. It is interesting that the number of redundant dislocations do not decrease at all, except that they are also frozen along the elastic line BC as shown in Fig. 4.24.

If the loading direction is reserved again by increasing γ from γ_* to zero, $(\gamma, \tilde{\tau})$ moves along the elastic line DO (yellow/light gray) where the dislocations and the effective temperature are frozen (see Fig. 1). Note that the effective temperature always increases during the loading along AB and loading in the opposite direction along CD as seen in Fig. 4.25, in agreement with the second law of thermodynamics.

It is remarkable that the loading path in the opposite direction CD differs essentially from the loading path AB due to the increase of the total number of dislocations along CD. Thus, along CD the material is closer to the steady state than along AB, and consequently, the slope of CD must be less than that of AB. This asymmetry between loadings in opposite directions becomes more pronounced as γ^* increases.

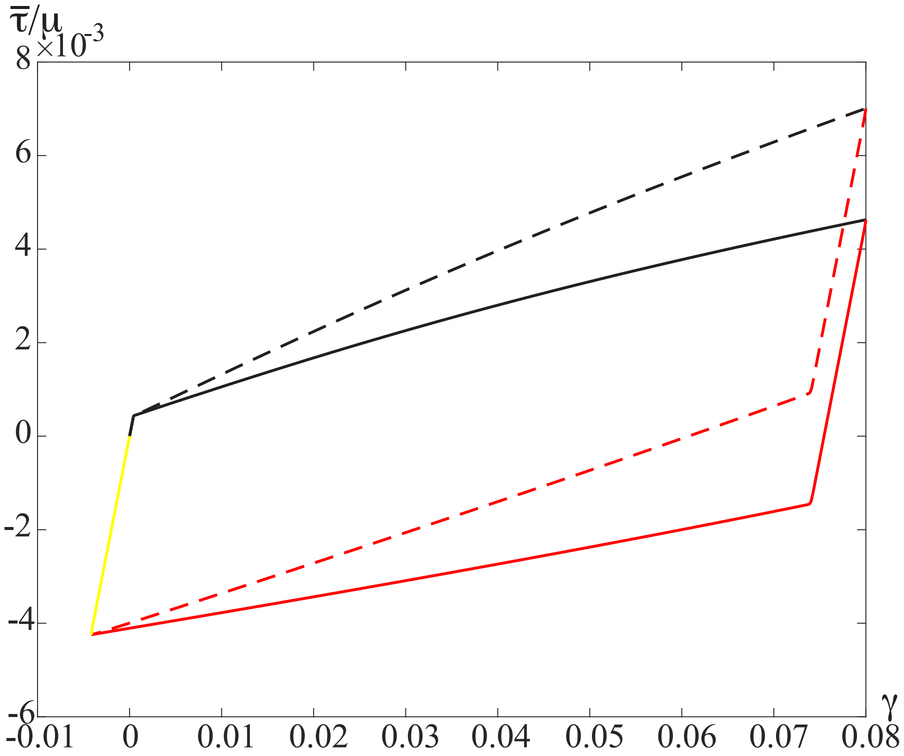

Figure 4.28: The stress-strain curves for specimens with different sizes at the strain rate $\tilde{Q} = 10^{-13}$, for room temperature, and for $\gamma^* = 0.08$: (i) $c = 5.1$ micron (dashed), (ii) $c = 51$ micro (bold).

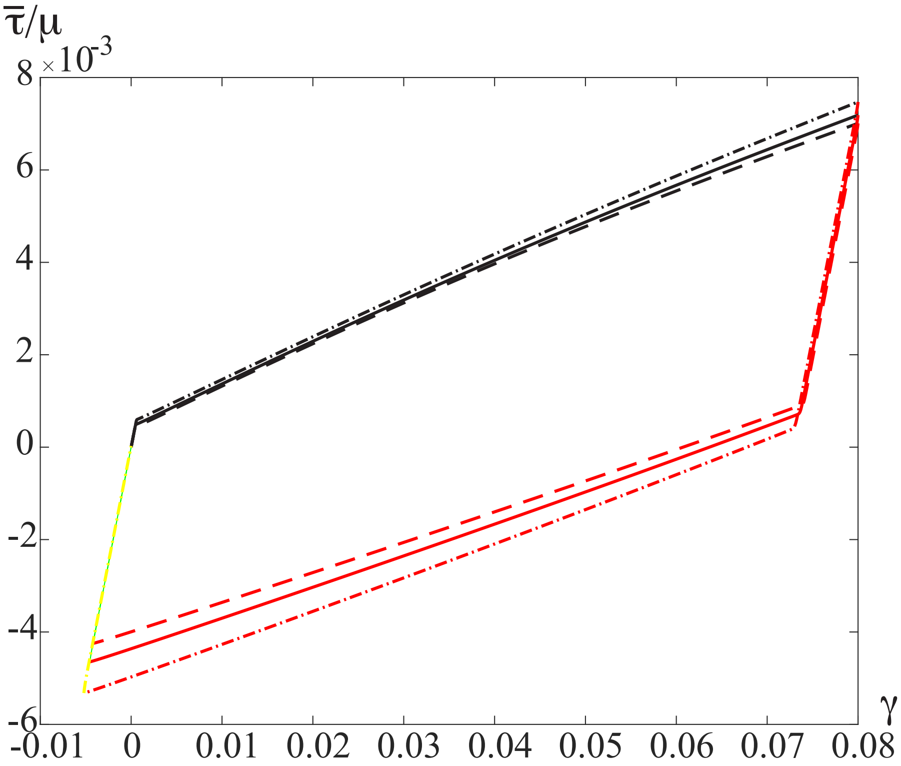

Figure 4.29: The stress-strain curves for the specimen loaded at different strain rates, for room temperature, and for $\gamma^* = 0.08$: (i) $\tilde{Q} = 10^{-13}$ (dashed), (ii) $\tilde{Q} = 10^{-11}$ (bold), (iii) $\tilde{Q} = 10^{-8}$ (dashed and dotted).

It is interesting to examine the influence of the size of the sample on the Bauschinger effect. Fig. 4.28 shows two stress-strain curves for two samples with different widths $c = 5.1$ micron (dashed line) and $c = 51$ micron (bold line) and with all other parameters being left unchanged. We see that the size strongly influences the slope of the hardening curve because the dislocation pile-up for the smaller sample leads to stronger kinematic hardening than for the larger sample (smaller is stronger). This affects the stress level at which the yielding transition occurs during load reversal. For the smaller sample, this stress is even positive.

Another important question is how much the strain rate affects the Bauschinger effect. Fig. 4.29 shows three stress-strain curves for three samples loaded at three different strain rates $\tilde{Q} = 10^{-13}$ (dashed line), $\tilde{Q} = 10^{-11}$ (bold line), and $\tilde{Q} = 10^{-8}$ (dashed and dotted line). The width of samples is $c = 5.1$ micron, while all other parameters remain unchanged. We see that the strain rate mainly affects the isotropic hardening, but much less the Bauschinger effect. Even for $\tilde{Q} = 10^{-8}$ (corresponding to the fast strain rate $Q = 10^4/\mathrm{s}$ which is typical of Hopkinson bar testing) the Bauschinger effect remains nearly the same as for the much slower loading. The reason is that the kinematic hardening due to the excess dislocations is much less sensitive to the change in strain rate. Also note that it is practically difficult to stop the load and instantly realize the load reversal at the same rate of strain, especially for the fast loading. Therefore, the real stress-strain curve usually deviates from the theoretical one in a small transient period. Perhaps this is one of the reasons for the differences between unloading and immediate reloading.

4.2.5 Discussions

The physical explanation of the Bauschinger effect on the basis of the back stress and the excess dislocations seems to be quite reasonable. In constructing the STZ-theory for glasses (Langer, 2008), Langer has argued that ”The Bauschinger effect is one example where the system remembers the direction in which it has been deformed, and responds differently – more compliantly or less so – to further loading in different directions. The natural way to include such effects in the theory is to let the STZ's possess internal degrees of freedom that carry information from one event to the next.” This argument holds true for dislocation mediated plasticity as well. Here, the incompatible plastic distortion is the natural variable that keeps the memory of excess dislocations. It cannot enter the free energy, but the curl of this quantity should enter the free energy causing the back stress. In this way the theory differs substantially from the phenomenological plasticity that introduces the back stress along with an assumed constitutive equation to fit the stress strain curves exhibiting the kinematic hardening. In contrary, this thermodynamic dislocation theory allows to find the back stress from the first principle calculation of the free energy of dislocated crystals and thus to predict the stress-strain curves and the Bauschinger effect.

As the comparison with the experiments is concerned, the experimental data in anti-plane shear-controlled deformations are not known yet, in contrast to the tension-compression tests provided in Abel and Muir (1972); Bate and Wilson (1986) or plane strain shear tests in Lewandowska (2003); Vincze et al. (2005), so the justification of the theory by the experiments is not possible at present time. However, the proposed theory may serve as a useful guide for the future experimental investigation on the Bauschinger effect in several directions: (i) the asymmetry between loadings in opposite directions at different level of γ^*, (ii) the influence of the size effect, (iii) the sensitivity of the back stress on the strain rate and temperature, et cetera. Last, but not least, the thermodynamic dislocation theory for uniform plastic deformations Langer et al. (2010) yields in the proportional compression tests for copper an excellent agreement with the experiments conducted in Follansbee and Kocks (1988) over a wide range of temperatures and strain rates. This gives a hope that the same will happen for the theory proposed in this section.

5 Conclusion

In this thesis the Thermodynamic Dislocation Theory (TDT) was successfully developed and used to determine the plastic behavior of crystals subject to different types of deformation, such as planar strain shear deformation, planar strain pressure, planar strain indentation, anti-planar shear deformation or torsion of bars.

In the first approach, where excess dislocations and kinematic strain hardening can be ignored, the theoretical curves take into account exactly the different stress-strain curves observed at very different strain rates and temperatures. Each curve begins with a yielding transition from elastic to plastic deformation at infinitesimally small strains. Each then passes through the hardening and softening regimes and ends (for high strain rates) with a robust shear band instability. One of the main reasons for the success of this theory is the extreme sensitivity of the plastic strain rate to small temperature or stress changes. On the other hand, the author tries to find ways to use these new findings to predict the performance of materials in engineering applications. Since this theoretical starting point is unconventional, the author has made extraordinary efforts to construct and test it as rigorously as possible. High demands are placed on the equations of motion and the selection of their parameters. The equations themselves are statements of known physical principles - conservation of energy and flow of entropy in accordance with the second law of thermodynamics - and they are expressed in terms of sufficiently defined internal state variables - dislocation density and the two thermodynamically defined temperatures. No phenomenological fitting functions are postulated. Each of the parameters occurring in the equations can basically be determined either by independent measurement or by calculation according to the first principles. We do not know this in conventional literature.

In the second approach, where the excess dislocations are taken into account, the author has built a meaningful framework of thermodynamic dislocation theory for nonuniform plastic deformation that helps to explain Bauschinger's physical mechanism and size effect. Here, incompatible plastic deformation is the natural variable that preserves the memory of excess dislocations. It cannot enter the free energy, but the curl of this quantity should enter the free energy that causes the back stress. In this way, the theory differs substantially from the phenomenological plasticity that introduces back stress together with an assumed constitutive equation to mimic the stress-strain curves with kinematic hardening. In contrary, this thermodynamic dislocation theory allows us to find the back stress from the first principle calculation of the free energy of dislocated crystals and thus to predict the stress-strain curves and the Bauschinger effect.

Besides, it is worth mentioning in this conclusion the finite element solution within the continuum dislocation theory, which is a simplified version of thermodynamic dislocation theory that takes into account only excess dislocations. This finite element implementation can be extended to TDT. This will open a promising and exciting research direction and enable one to solve more complex problems such as 3-D indentation test for single crystals with more than one slip system or 3-D plastic deformations.

Matlab supplement

The complete system of four integro-differential equations (3.11)-(3.17) are reduced to a system of $6n+1$ ordinary differential equations and implemented by using equations (3.21)-(3.22).

```matlab
function dude = PDE(u,dy,ny,tp,r,chi0,kappaChi,kappaRho,c0,c1,c2,k1,k2,theta0,q0)
sigma=u(1);
rho=u(2:ny+1);
chi=u(ny+2:2*ny+1);
theta=u(2*ny+2:3*ny+1);

integro=0;
for i=1:ny
        mui=mu(theta(i),tp);
        qi=q(sigma,rho(i),theta(i),tp,r);
        if(i==1||i==ny) integro=integro+mui*qi*dy/(4*q0);
        else integro=integro+mui*qi*dy/(2*q0);
        end
end
dsigmade=mu(theta(1),tp)-integro;

for i=1:ny
        mui=mu(theta(i),tp);
        qi=q(sigma,rho(i),theta(i),tp,r);
        nu0i=nu0(rho(i),theta(i),qi);
        ki=k(theta(i),c0,c1,c2,tp);

        drhode(i)=(kappaRho/(nu0i)^2)*(sigma*qi/(mui*r*q0))*(1-rho(i)/exp(-1/chi(i)));
        dchide(i)=kappaChi*sigma*(qi/(mui*r*q0))*(1-chi(i)/chi0);

        if(i==1 || i==ny) dthetade(i)=0;
        else dthetade(i)=ki*sigma*qi/q0+(k1/q0)*(theta(i+1)-2*theta(i)+theta(i-1))/(dy^2)-k2*(theta(i)-theta0)/q0;
        end
end

dude=[dsigmade; drhode; dchide; dthetade];
end
```

A piece of Matlab code which supports to run the least-square analysis for the sum square function (3.8):

```
function output=optimizationSS(pars0,lb,ub)
func = @(z)sumsquares(z);
problem = createOptimProblem('fmincon','objective', func,'x0',pars0,'lb',lb,'ub',ub);
gs = GlobalSearch;

output = run(gs,problem);
end
```

```
function ss = sumsquares(z)

load data_298_1000.txt;
%% T=298 K,q0=1000/s==================================
sigmaData=data_298_1000(:,2);
epsilonData=data_298_1000(:,1);
temperature=298;
q0=1000*10^(-12);

[epsilonNum,sigmaNum]=langerSolver(z,temperature,q0);
sigmaNumInteP = interp1(epsilonNum,sigmaNum,epsilonData,'spline');

for k=1:length(data_298_1000)
ss=ss+(sigmaNumInteP(k)-sigmaData(k))^2;
end
end
```

References

Abbod, M. F., Sellars, C. M., Cizek, P., Linkens, D. A., & Mahfouf, M. (2007). Modeling the flow behavior, recrystallization, and crystallographic texture in hot-deformed fe-30 wt pct ni austenite. *Metallurgical and Materials Transactions A*, *38*(10), 2400–2409.

Abel, A., & Muir, H. (1972). The bauschinger effect and discontinuous yielding. *Philosophical Magazine*, *26*(2), 489–504.

Ashby, M. F. (1970). The deformation of plastically non-homogeneous materials. *Philosophical Magazine*, *21*(170), 399–424.

Baitsch, M., Le, K. C., & Tran, T. M. (2015, sep). Dislocation structure during microindentation. *International Journal of Engineering Science*, *94*, 195–211.

Basinski, S. J., & Basinski, Z. S. (1966). The nature of the cold worked state. In *Recrystalization, grain growth, and textures, papers presented at a seminar of the american society for metals, metals park, ohio, usa.*

Bate, P. S., & Wilson, D. V. (1986). Analysis of the bauschinger effect. *Acta Metallurgica*, *34*(6), 1097–1105.

Berdichevsky, V. L. (2005). Homogenization in micro-plasticity. *Journal of the Mechanics and Physics of Solids*, *53*(11), 2457–2469.

Berdichevsky, V. L. (2006a). Continuum theory of dislocations revisited. *Continuum Mechanics and Thermodynamics*, *18*(3-4), 195.

Berdichevsky, V. L. (2006b). On thermodynamics of crystal plasticity. *Scripta materialia*, *54*(5), 711–716.

Berdichevsky, V. L. (2017). A continuum theory of screw dislocation equilibrium. *International Journal of Engineering Science*, *116*, 74–87.

Berdichevsky, V. L., & Sedov, L. I. (1967). Dynamic theory of continuously distributed dislocations. its relation to plasticity theory. *Journal of Applied Mathematics and Mechanics*, *31*(6), 989–1006.

Bilby, B. A. (1955). Types of dislocation source. In *Report of bristol conference on defects in crystalline solids* (pp. 124–133).

Brent, R. P. (2013). *Algorithms for minimization without derivatives*. Massachusetts, U.S.A.: Courier Corporation.

Burger, J. M. (1939). Some considerations on the fields of stress connected with dislocations in a regular crystal lattice. *Proc. Kon. Ned. Akad. Wetenschap*, *42*, 293.

Callister, W. D. (2007). *Materials science and engineering: an introduction*. New York, U.S.A: John Wiley & Sons. Inc.

Chen, S. R., Stout, M. G., Kocks, U. F., MacEwen, S. R., & Beaudoin, A. J. (1998). *Constitutive modeling of a 5182 aluminum as a function of strain rate and temperature* (Tech. Rep.). Los Alamos National Lab., NM (United States).

Cottrell, A. H. (1964). The mechanical properties of materials. *J. Wiley*, 277.

Dahlberg, C. F. O., Saito, Y., Öztop, M. S., & Kysar, J. W. (2014). Geometrically necessary dislocation density measurements associated with different angles of indentations. *International Journal of Plasticity*, *54*, 81–95.

De Borst, R., Crisfield, M. A., Remmers, J. J. C., & Verhoosel, C. V. (2012). *Nonlinear finite element analysis of solids and structures*. West Sussex, England: John Wiley &

Sons, Ltd.

Dieter, G. E., & Bacon, D. J. (1986). *Mechanical metallurgy.* New York, U.S.A: McGraw-hill.

Duffy, M. G. (1982). Quadrature over a pyramid or cube of integrands with a singularity at a vertex. *SIAM journal on Numerical Analysis*, *19*(6), 1260–1262.

Elam, C. F. (1935). *Distortion of metal crystals.* Oxford University Press, London.

Ewing, J. A., & Rosenhain, W. (1900). Bakerian lecture–the crystalline structure of metals. *Proceedings of the Royal Society of London*, *65*(413-422), 172–177.

Follansbee, P. S., & Kocks, U. F. (1988). A constitutive description of the deformation of copper based on the use of the mechanical threshold stress as an internal state variable. *Acta Metallurgica*, *36*(1), 81–93.

Frank, F. C., & Read, W. T. (1950). Multiplication processes for slow moving dislocations. *Physical Review*, *79*(4), 722.

Frenkel, J. (1926). Zur theorie der elastizitätsgrenze und der festigkeit kristallinischer körper. *Zeitschrift für Physik*, *37*(7-8), 572–609.

Galindo-Nava, E. I., & Rivera-Díaz-del Castillo, P. E. J. (2013). Thermostatistical modelling of hot deformation in fcc metals. *International Journal of Plasticity*, *47*, 202–221.

Goto, D. M., Garrett, R. K., Bingert, J. F., Chen, S. R., & Gray, G. T. (2000). The mechanical threshold stress constitutive-strength model description of hy-100 steel. *Metallurgical and Materials Transactions A*, *31*(8), 1985–1996.

Gurtin, M. E. (2002). A gradient theory of single-crystal viscoplasticity that accounts for geometrically necessary dislocations. *Journal of the Mechanics and Physics of Solids*, *50*(1), 5–32.

Hirth, J. P., & Lothe, J. (1992). *Theory of dislocations.* Malabar, Florida: Krieger.

Holmquist, T. J. (1987). *Strength and fracture characteristics of hy-80, hy-100, and hy-130 steels subjected to various strains, strain rates, temperatures, and pressures* (Tech. Rep.). HONEYWELL INC BROOKLYN PARK MN ARMAMENT SYSTEMS DIV.

Holzapfel, G. A. (2000). *Nonlinear solid mechanics: a continuum approach for engineering.* West Sussex, England: John Wiley & Sons, Ltd.

Horstemeyer, M. F., Lim, J., Lu, W. Y., Mosher, D. A., Baskes, M. I., Prantil, V. C., & Plimpton, S. J. (2002). Torsion/simple shear of single crystal copper. *Journal of Engineering materials and technology*, *124*(3), 322–328.

Kaluza, M., & Le, K. C. (2011). On torsion of a single crystal rod. *International Journal of Plasticity*, *27*(3), 460–469.

Kochmann, D. M. (2009). *Mechanical modeling of microstructures in elasto-plastically deformed crystalline solids* (Unpublished doctoral dissertation). Ruhr Universität Bochum, Germany.

Kochmann, D. M., & Le, K. C. (2008). Dislocation pile-ups in bicrystals within continuum dislocation theory. *International Journal of Plasticity*, *24*(11), 2125–2147.

Kochmann, D. M., & Le, K. C. (2009a). A continuum model for initiation and evolution of deformation twinning. *Journal of the Mechanics and Physics of Solids*, *57*(6), 987–1002.

Kochmann, D. M., & Le, K. C. (2009b). Plastic deformation of bicrystals within continuum dislocation theory. *Mathematics and Mechanics of Solids*, *14*(6), 540–563.

Kocks, U. F., & Mecking, H. (2003). Physics and phenomenology of strain hardening: the fcc case. *Progress in materials science*, *48*(3), 171–273.

Koehler, J. S. (1941). On the dislocation theory of plastic deformation. *Physical Review*, *60*(5), 397.

Kondo, K. (1952). On the geometrical and physical foundations of the theory of yielding. In *Proc. 2nd japan nat. congr. applied mechanics* (Vol. 2, pp. 41–47).

Koster, M., Le, K. C., & Nguyen, B. D. (2015). Formation of grain boundaries in ductile single crystals at finite plastic deformations. *International Journal of Plasticity*, *69*, 134–151.

Kröner, E. (1955). Der fundamentale zusammenhang zwischen versetzungsdichte und spannungsfunktionen. *Zeitschrift für Physik*, *142*(4), 463–475.

Kröner, E. (1958). *Kontinuumstheorie der versetzungen und eigenspannungen* (Vol. 5). Springer.

Kröner, E. (1992). Mikrostrukturmechanik. *GAMM-Mitteilungen*, *15*, 104–119.

Kysar, J. W., Saito, Y., Oztop, M. S., Lee, D., & Huh, W. T. (2010). Experimental lower bounds on geometrically necessary dislocation density. *International Journal of Plasticity*, *26*(8), 1097–1123.

Langer, J. S. (2008). Shear-transformation-zone theory of plastic deformation near the glass transition. *Physical Review E*, *77*, 021502.

Langer, J. S. (2015). Statistical thermodynamics of strain hardening in polycrystalline solids. *Phys. Rev. E*, *92*, 032125.

Langer, J. S. (2016). Thermal effects in dislocation theory. *Phys. Rev. E*, *94*, 063004.

Langer, J. S. (2017a). Thermal effects in dislocation theory. II. Shear banding. *Phys. Rev. E*, *95*, 013004.

Langer, J. S. (2017b). Thermodynamic theory of dislocation-enabled plasticity. *Phys. Rev. E*, *96*, 053005.

Langer, J. S. (2017c). Yielding transitions and grain-size effects in dislocation theory. *Phys. Rev. E*, *95*, 033004.

Langer, J. S., Bouchbinder, E., & Lookman, T. (2010). Thermodynamic theory of dislocation-mediated plasticity. *Acta Materialia*, *58*(10), 3718–3732.

Le, K. C. (2010). *Introduction to micromechanics*. Nova Science Inc.

Le, K. C. (2018). Thermodynamic dislocation theory for non-uniform plastic deformations. *Journal of the Mechanics and Physics of Solids*, *111*, 157–169.

Le, K. C., & Berdichevsky, V. L. (2001). Energy distribution in a neutral gas of point vortices. *Journal of Statistical Physics*, *104*(3), 881–892.

Le, K. C., & Günther, C. (2014). Nonlinear continuum dislocation theory revisited. *International Journal of Plasticity*, *53*, 164–178.

Le, K. C., & Nguyen, B. D. (2012). Polygonization: Theory and comparison with experiments. *International Journal of Engineering Science*, *59*, 211–218.

Le, K. C., & Nguyen, B. D. (2013). On bending of single crystal beam with continuously distributed dislocations. *International Journal of Plasticity*, *48*, 152–167.

Le, K. C., & Nguyen, Q. S. (2010). Polygonization as low energy dislocation structure. *Continuum Mechanics and Thermodynamics*, *22*(4), 291–298.

Le, K. C., & Piao, Y. (2018). Non-uniform plastic deformations of crystals undergoing anti-plane constrained shear. *Archive of Applied Mechanics*.

Le, K. C., Piao, Y., & Tran, T. M. (2018). Thermodynamic dislocation theory: torsion of bars. *Physical Review E*, *98*, 063006.

Le, K. C., & Sembiring, P. (2008a). Analytical solution of plane constrained shear problem for single crystals within continuum dislocation theory. *Archive of Applied Mechanics*, *78*(8), 587–597.

Le, K. C., & Sembiring, P. (2008b). Plane constrained shear of single crystal strip with two active slip systems. *Journal of the Mechanics and Physics of Solids*, *56*(8), 2541–2554.

Le, K. C., & Sembiring, P. (2009). Plane constrained uniaxial extension of a single crystal strip. *International Journal of Plasticity*, *25*(10), 1950–1969.

Le, K. C., & Stumpf, H. (1994). *Finite elastoplasticity with microstructure.* Inst. für Mechanik.

Le, K. C., & Stumpf, H. (1996). A model of elastoplastic bodies with continuously distributed dislocations. *International journal of plasticity*, *12*(5), 611–627.

Le, K. C., & Tran, T. M. (2017). Dislocation mediated plastic flow in aluminum: Comparison between theory and experiment. *International Journal of Engineering Science*, *119*, 50–54.

Le, K. C., & Tran, T. M. (2018). Thermodynamic dislocation theory: Bauschinger effect. *Phys. Rev. E*, *97*(4), 43002.

Le, K. C., Tran, T. M., & Langer, J. S. (2017). Thermodynamic dislocation theory of high-temperature deformation in aluminum and steel. *Physical Review E*, *96*(1), 013004.

Le, K. C., Tran, T. M., & Langer, J. S. (2018). Thermodynamic dislocation theory of adiabatic shear banding in steel. *Scripta Materialia*, *149*, 62–65.

Lewandowska, M. (2003). Dependence of the deformation microstructure of aluminium alloys on the strain path. *Materials chemistry and physics*, *81*(2-3), 555–557.

Limkumnerd, S., & Van der Giessen, E. (2008). Statistical approach to dislocation dynamics: From dislocation correlations to a multiple-slip continuum theory of plasticity. *Phys. Rev. B*, *77*(18), 184111.

Liu, D., Zhang, X., Li, Y., & Dunstan, D. J. (2018). Critical thickness phenomenon in single-crystalline wires under torsion. *Acta Materialia*, *150*, 213–223.

Marchand, A., & Duffy, J. (1988). An experimental study of the formation process of adiabatic shear bands in a structural steel. *Journal of the Mechanics and Physics of Solids*, *36*(3), 251–283.

Meyers, M. A., Andrade, U. R., & Chokshi, A. H. (1995). The effect of grain size on the high-strain, high-strain-rate behavior of copper. *Metallurgical and materials transactions A*, *26*(11), 2881–2893.

Nye, J. F. (1953). Some geometrical relations in dislocated crystals. *Acta metallurgica*, *1*(2), 153–162.

Orowan, E. (1934). The crystal plasticity. iii: about the mechanism of the sliding. *Z Physik*, *89*, 634–659.

Poh, L. H., Peerlings, R. H. J., Geers, M. G. D., & Swaddiwudhipong, S. (2013). Homogenization towards a grain-size dependent plasticity theory for single slip. *Journal of the Mechanics and Physics of Solids*, *61*(4), 913–927.

Polanyi, M. (1934). Über eine art gitterstörung, die einen kristall plastisch machen könnte. *Zeitschrift für Physik*, *89*(9-10), 660–664.

Reuber, C., Eisenlohr, P., Roters, F., & Raabe, D. (2014). Dislocation density distribution around an indent in single-crystalline nickel: Comparing nonlocal crystal plasticity finite-element predictions with experiments. *Acta Materialia*, *71*, 333–348.

Saito, Y., & Kysar, J. W. (2011). Wedge indentation into elastic–plastic single crystals, 1: Asymptotic fields for nearly-flat wedge. *International Journal of Plasticity*, *27*(10), 1640–1657.

Saito, Y., Oztop, M. S., & Kysar, J. W. (2012). Wedge indentation into elastic–plastic single crystals. 2: simulations for face-centered cubic crystals. *International Journal of Plasticity*, *28*(1), 70–87.

Schmid, E. (1924). Yield point of crystals, critical shear stress law. In *Proceedings of the first international congress for applied mechanics, delft* (pp. 342–353).

Sedov, L. I. (1968). Variational methods of constructing models of continuous media. In *Irreversible aspects of continuum mechanics and transfer of physical characteristics in moving fluids* (pp. 346–358). Springer.

Shi, H., McLaren, A. J., Sellars, C. M., Shahani, R., & Bolingbroke, R. (1997a). Constitutive equations for high temperature flow stress of aluminium alloys. *Materials Science and Technology*, *13*(3), 210–216.

Shi, H., McLaren, A. J., Sellars, C. M., Shahani, R., & Bolingbroke, R. (1997b). Hot plane strain compression testing of aluminum alloys. *Journal of testing and evaluation*, *25*(1), 61–73.

Taylor, G. I. (1934). The mechanism of plastic deformation of crystals. part i. theoretical. *Proceedings of the Royal Society of London. Series A*, *145*(855), 362–387.

Varshni, Y. P. (1970). Temperature dependence of the elastic constants. *Physical Review B*, *2*(10), 3952.

Vincze, G., Rauch, E. F., Gracio, J. J., Barlat, F., & Lopes, A. B. (2005). A comparison of the mechanical behaviour of an aa1050 and a low carbon steel deformed upon strain reversal. *Acta Materialia*, *53*(4), 1005–1013.

Volterra, V. (1907). On the equilibrium of multiply-connected elastic bodies. *Ann. Ec. Norm*, *24*(3), 401–517.

Weertman, J., & Weertman, J. R. (1964). *Elementary dislocation theory*. Macmillan.

Wriggers, P., & Zavarise, G. (2004). Computational contact mechanics. *Encyclopedia of computational mechanics*.

Zaiser, M. (2015). Local density approximation for the energy functional of three-dimensional dislocation systems. *Phys. Rev. B*, *92*(17), 174120.

Curriculum Vitae

Personal Data

Name	Tran Tuan Minh
Date of Birth	November 11, 1986
Place of Birth	Can Tho, Vietnam
Nationality	Vietnamese

Education

2004–2008	Bachelor of Engineering – Mechatronics Engineering, Can Tho University, Vietnam
2009-2011	Master of Engineering – Computational Engineering, Vietnamese-German University, Vietnam in cooperation with Ruhr-University Bochum, Germany
2015-present	Ph.D. Candidate – Chair of Mechanics-Material Theory, Ruhr-University Bochum, Germany

Professional Occupation

11/2008–10/2009	Teaching assistant, Can Tho University, Vietnam
05/2011-11/2011	Internship, Robert BOSCH group, Vietnam
02/2012-12/2014	Research and teaching assistant, Vietnamese-German University, Vietnam
01/2015-present	Research associate, Chair of Mechanics-Material Theory, Ruhr-University Bochum, Germany

Bochum, April 29, 2019

Mitteilungen aus dem Institut für Mechanik
RUHR-UNIVERSITÄT BOCHUM
Nr. 180

ISBN 978-3-935892-58-2